Aalto University
School of Engineering

European Mining Course

Dzugala Magdalena

Pull experiment to validate the photogrammetrically predicted friction angle of rock discontinuities

Master's Thesis

Espoo, 26.08.2016

Supervisor: Prof. Mikael Rinne

Instructor: M.Sc. Lauri Uotinen

Aalto University
School of Engineering

Aalto University, P.O. 11000, 00076 AALTO
www.aalto.fi

Abstract of Master's thesis

Author Magdalena Dzugala

Title of thesis Pull experiment to validate the photogrammetrically predicted friction angle of rock discontinuities

Degree programme European Mining, Minerals and Environmental Program

Major/minor European Mining Course **Code**R3008

Thesis supervisor Prof. Mikael Rinne

Thesis advisor(s) M.Sc. Lauri Uotinen, M.Sc. Joni Sirkiä

Date 26.08.2016 **Number of pages** 116 + 6 **Language** English

Abstract

The accurate estimation of the mechanical properties of a rock joints is crucial in terms of safety when it comes to design of slopes in open pit mines or caverns used for the storage of hazardous materials, for instance – nuclear waste. Photogrammetry provides a simple and objective method of joints roughness assessment, without the need for expensive and time consuming laboratory tests or imprecise empirical methods.

In this thesis photogrammetric method developed in KARMO II project was used to estimate the roughness, shear strength and friction angle of a discontinuity of big scale sample. That estimation was done by analyzing the profiles of digital models of joint surface. Surface length and slope measurement methods were used to calculate the values of joint roughness coefficient of analyzed surfaces. Alternatively, JRC was also estimated empirically, with hand profiling method, and the same calculations were done for JRC values obtained this way. Next, Barton – Bandis criterion was used to calculate the shear strength and friction angle of the joint. Additionally, the shear strength and friction angle of the rock discontinuity were obtained experimentally with multistage pull testing. The results obtained with all methods were analyzed and compared.

JRC values from photogrammetrically created digital models of the joint surface were overestimated due to the models not being dense enough which resulted in high noise to signal ratio. High JRC values combined with low normal load used during the pull test constrained the applicability of Barton – Bandis criterion and the linear interpolation was used to determine the shear strength and friction angle of tested rock surfaces. Values of shear strength obtained with photogrammetrically created models were overestimates in relation to the results of the pull test by approximately 45%.

The errors made during this research are analyzed in the thesis and recommendations on how to improve reliability of the results are made. Main error in photogrammetric prediction was too low density of the point clouds and in laboratory test too low stiffness of the test arrangement. The alternative methodology for photogrammetric studies used in previous stage of the KARMO I project was tested in this thesis and was proven to give significantly higher accuracy of generated digital models. The stiffness of the testing machine and proper positioning of the sample halves on top of each other were identified as the most sensitive aspects of methodology of big scale pull test when it comes to reliability of the results.

KeywordsPhotogrammetry, pull test, friction angle, rock joints, shear strength, JRC prediction

Foreword

I would like to thank everyone who contributed to the completion of this thesis.

Prof. Mikael Rinne
Lauri Uotinen
Joni Sirkiä
Pertti Alho
Piironen Jukka
Veli – Antti Hakala
Otto Hedström
Matti Ristimäki
Lauri Sipilä
Harm Oosterbaan

Thank you!

I would also like to acknowledge the Ministry of the Economical Affairs and Employment who funded this research.

Table of contents

List of figures

1 Introduction

The determination of shear strength of rock discontinuities is an object of research since the middle of the last century, yet the developed models and failure criterions are based on simplifications which are the topic of ongoing discussion in the field of rock mechanics (Barton, 2013). The reason for that is the multiplicity and complexity of the parameters affecting the value of the shear strength of a joint or its friction angle. Amongst said parameters there is joint surface condition (dry, wet, submerged, weathered, unweathered), roughness of the joint surface, matedness (matching) of the opposites of a joint, compressive strength of a joint, normal load which the joint is subjected to and the mineral composition of the jointed rock, which determines its basic friction angle (Giani, 1992).

The parameter which is the most challenging to quantify is the roughness of a joint surface. That is mainly due to the anisotropic character of natural joints. Directional variation in the joint roughness results in the different shear strength of the same joint depending on the direction of shearing (Grasselli, 2001). Therefore, most commonly used method of determining the roughness – Joint Roughness Coefficient profiling (Barton and Choubey, 1977), ISRM suggested method (ISRM, 2007) is considered subjective by significant amount of investigators, since it only quantifies the roughness in one direction and involves a human decision on where to measure the shape of the profile, and then to match the obtained profile with a reference (Kulatilake *et al*., 1995; Hsiung *et al*.1993; Grasselli, 2001).

Besides that, many publications state that the shear strength of a rock joint is a scale dependent variable (Bandis, 1980; Barton and Choubey, 1977; Castelli *et al*, 2001). However the exact relation between the scale and shear strength of a joint, the reason for a scale effect, and even the existence of this effect is a subject of a debate between the scientist. Several divergent articles have been published on that matter, reporting negative scale effect, positive scale effect and no scale effect at all (Bandis, Lumsden and Barton, 1981; Kutter and Otto, 1990; Johansson, 2015).

Significant contribution to the improvement of the peak shear strength criteria were made in recent decades, incorporating alternative methods of quantifying the roughness of a rock joint. Fractals are used very frequently as a measure of rock fracture roughness (Brown, 1987; Hsiung, *et al*., 1993; Lee *et al*., 1990; Malinverno, 1990; Pwer and Tullis, 1991; Wakabayashi and Fukushige, 1992; McWilliams, Kerkering and Miller, 1993). Conventional statistical parameters have been used by some researchers to quantify the joint roughness (Kulatilake *et al*., 1995). Although, those approaches only consider 2D profiles and therefore cannot represent the anisotropy which is present in natural rock joints. The limits of said methods were overcame by taking into account the three - dimensional surface geometry of a joint (Grasselli, 2001; Tatone and Grasselli, 2009). The main principle of the criterion proposed by Tatone and Grasselli is to create a high density point cloud model of the joint surface collected by optical instruments – for instance, close range photogrammetry or laser scanning (Tatone and Grasselli, 2009; Sirkia, 2015). However, there is a significant economic advantage of photogrammetry in relation to the laser scanning since it can produce good results using off – the – shelf equipment (Nilsson, Edelbro and Sharrock, 2012).

The digital modelling of a joint surface using photogrammetry is an easy alternative for the standard methods of the joint roughness assessment.

This method can be executed using standard off-the-shelf equipment – a camera with a fixed lens and a photogrammetry software (Nilsson, Edelbro and Sharrock, 2012). Photogrammetry has been successfully used for the surface roughness evaluation by many researchers (Kolecka, 2011; Unala, Yakarb and Yildizb, 2004; Nilsson and Edelbro, 2012; Kim, Gratchev and Poropat, 2013). Many publications report that results obtained by phiotogrammetry are more accurate compering to other methods such as dial gauges measurement, profilometry or drag measurement system (Unal, Yakar and Yildiz, 2004) In practice, the photogrammetry is commonly used to obtain the data for kinematic and numerical analyses in the slope stability assessment (Kim, Gratchev and Poropat, 2013).

However, besides its unquestionable advantages described in the paragraph above, photogrammetry is also not free of errors and certain limits. Recent research show some discrepancies between the JRC values obtained by photogrammetry and measurements with the Barton´s profilometer (Kim, Gratchev and Poropat, 2013; Nilsson, Edelbro and Sharrock, 2012; Sirkiä, 2015). Of course, the accuracy of this method is dependent on the quality and spatial density of the digital images. (Nilsson, Edelbro and Sharrock, 2012; Schenk, 2005). Therefore, too low resolution of obtained images can lead to underestimation of the surface roughness, while too high resolution of the images taken at close distances can have opposite effect – overestimation of this value (Kim, Gratchev and Poropat, 2013). The comprehensive evaluation of the errors and limitations of the method, as well as the recommendations on the procedure which gives the best performance was done by Sirkiä (2015).

The accurate estimation of the mechanical properties of a rock joints, including shear strength and angles of friction is crucial in terms of safety when it comes to design of slopes in open pit mines or caverns used for the storage of hazardous materials, for instance – nuclear waste. Shear failure can have serious healthy, economical, technological and environmental consequences, especially if it occurs in the vicinity of the storage of hazardous material. This Master´s Thesis was conducted as a part of the KARMO (Mechanical Properties of Rock Joints) research project which is a subproject of the KYT2018 Finnish Research Program on Nuclear Waste Management. KARMO project is conducted by the Geoengineering research group of Aalto University and it aims to develop an independent method which will allow to determine the mechanical properties of rock joint.

The first part of KARMO project – KARMO I started in 2014. In this part, the pilot experiment was done to develop a method for producing the rock joint surfaces replicas using photogrammetry and produced replicas were subjected to a shear test (Korpi, unpublished). In 2015, KARMO II was continuing the development of the method produced before. This development was mainly concentrated on defining the quantity and quality requirements of initial data and determining a procedure to minimize the error and information loss in the process.

The focus of presented thesis is to validate the mechanical properties of a rock joint predicted using the photogrammetry procedure developed in 2014 - 2015. This is done by comparing the values of friction angles obtained experimentally with results obtained using digital modelling of photogrammetrically created images.
Therefore, the main objectives of this thesis can be formulated as a steps in the process of validation:

1. To determine the peak friction angle value of the granite sample by using photogrammetry.
2. To determine the peak friction angle value of the granite sample by conducting laboratory tests.
3. To compare the result gained using both methods.
4. To identify the sources of potential discrepancies between them.
5. To propose changes in the experiment set up or data interpretation to minimize/eliminate those discrepancies.

Besides the major objectives thesis also aims to empirically determine the residual and peak shear strength of a rock joint as well as record the dilation of the sample during the test. To conclude, thesis attempts to answer the following questions:

- Is photogrammetry a valid method to predict the friction angle of a rock joint and if not, why?
- Is the experiment methodology appropriate for determining the shear strength of rock joint, and if not why?
- How the measurement procedure (both experimental and photogrammetric) can be improved to give more reliable results?

2 Preceding studies

2.1 Development of a method to replicate the rock joint surfaces.

In this first stages of KARMO, three bachelor projects of Raphael Yorke, Paulina Kallio and Laura Tolvanen were done. The objectives of this studies were:

- To test the usability of photogrammetry as a method to create the molds for concrete casting of rock joints replicas.
- To experimentally develop a recipe for self-compacting mortar for casting of the rock joint replicas.
- To create the high quality digital models of produced replicas for further studies of the difference in roughness between the original surface and its replicas.

The replicas process of creating the replicas is described (Korpi, 2015; Uotinen et al, 2015). The objective of the study was to determine the loss of information about the joint surface roughness and geometry involved in photogrammetry, downscaling, 3D printing and casting. During the research a method was developed to model the surface of a fresh, unweather rock joint. The workflow was consist of the following steps:

- Creation of the digital point cloud model of a rock surface using close range hand held photogrammetry. The point cloud resolution was 16.2 points/mm^2
- Downscaling of the point cloud model from scale 1:1 to scale 1:10 and triangulation of downscaled models (5 different), original size of the sample was 175 cm x 60 cm
- Creation of the molds by 3D printing the downscaled and triangulated models (pilot, molding)
- Casting the concrete replicas in the molds created previously
- Shear box testing of the replicas

Before the final casting of the replicas three types of molding and casting techniques were tested to find out the optimal method.
The loss of information about the rock surface geometry was quantified by comparing the joint roughness coefficients (JRC) of the original samples and the replicas. The results showed the decrease of the JRC value for replicas in scale 1:1 in comparison to the original rock measured in direction perpendicular to the shearing. The values measured parallel to the shearing direction do not show that kind of correlation. For some sample sizes JRC value are smaller for replicas in relation to the original rock surface, for some the opposite.
Additionally as a part of results interpretation, the shear strength of the different scale replicas were confronted to investigate the effect of scale on the joint shear resistance. This comparison was done for both peak and residual shear strength and does not reveal any clear correlation. In fact the values are scattered, making it impossible to draw any conclusion about the trend.

During his study Korpi assumed that the scale effect is not present since the replicas were made to be perfectly matched, so the contact area for different sample sizes was assumed to be approximately the same. Therefore the changes in the shear strength with scale were presumed to be an effect of loss of geometrical features of joint surfaces caused by downscaling and replicating.

Yet, during the shear box test, the negative vertical displacement was noted at the beginning of the experiment indicating that the joint was "closing" and consequently was in reality mismatched. This behavior of the joint´s shear strength together with the natural difference in the roughness of different sample surfaces was given by Korpi as an explanation for the lack of apparent correlation pattern between the shear strength and the sample scale. However, considering the linear regression of the presented values the declining trend can be noticed between the shear strength of a joint and the sample scale. There is an evident drop in the shear strength of sample scale 1:1 and 1:10 for both peak and residual shear strength values. Besides, the roughness component of the peak shear strength estimated during the shear box test of the sample scale 1:10 was only equal to 59% of the same parameter for sample scale 1:1. That could be presumed to be an effect of smoothening the joint surface while the downscaling factor is increasing. Though, the linear representation of the data cannot be considered as accurate since the R^2 coefficient values are relatively low.

The results of this studies were compiled and published as a conference paper in the 13th International ISRM congress 2015 (Uotinen et al., 2015)

2.2 Development of a method of photogrammetric recording of rock joint surfaces.

During this stage of KARMO project Joni Sirkiä was working on establishing the requirements for initial data in photogrammetric recording of rock joint surfaces. (Sirkiä, 2015).

This research was done as a part of KARMO II project and its aim was defined by three steps:

- Identification of the errors involved in the photogrammetric replication process,
- Development of a method for measuring the accuracy of photogrammetric replication process,
- Formulation of recommendations for the imaging arrangement and photogrammetric processing by evaluating the impact of images quality and quantity on produced errors.

During this study the surface roughness evaluation was conducted using four methods: JRC measurements using hand held profilometer, JRC measurements derived from the digital models with surface length (Maerz et al., 1990) and slope length measurement (Tse and Cruden, 1979) methods, 3D roughness evaluation with surface area method derived from 2D surface length method, and finally, Directional 3D roughness evaluation introduced by Tatone and Grasselli (2009). The study was executed on different type of specimens, including original rock slab, casting mold and replica sample produced during the KARMO I as well as the digital models of rock slab, casting mold and replica sample produced with photogrammetric modelling.

The outcome of the research is that roughness evaluation executed during the thesis is suitable in representing the changes of the joint surface roughness resulting from the photogrammetric replication process. The best results were achieved using the directional, 3D surface roughness characterization, since it takes into account the whole surface area of the joint. Concluding his thesis, Sirkiä recommended for upcoming studies in KARMO research projects to construct the imaging procedure in a way that the sample is photographed from every direction possible and from multiple heights.

The lightning should be constant and "sufficient" to allow the fast shutter speed (for hand held photogrammetry) and low ISO sensitivity. Quantitative study conducted by Sirkiä showed that the point cloud model reaches its saturation level for about 300 hundred pictures, therefore this number was recommended to be sufficient in further photogrammetry projects (Figure 1). Yet, Sirkiä pointed out that the results might not be accurate since the said studies were conducted using ISO sensitivity value 2000. For the used camera base ISO value is 100 and it is known that high ISO sensitivity introduces noise to the picture which can be observed as a "grainy" texture. The effect of this noise can be observed on a graph presented below, where the density of a point cloud is showed as a function of the number of images. The unexpected peak occurring for around 40 images can be presumed to result from the noise contamination of the analyzed pictures.

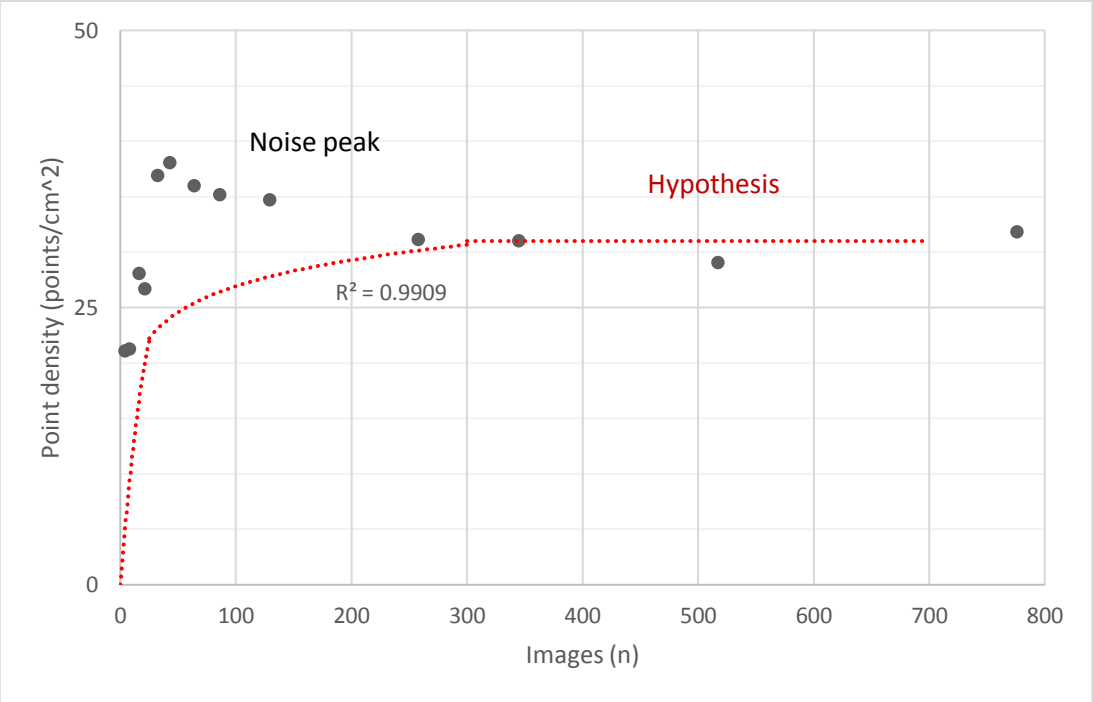

Figure 1 The density of a point cloud as a function number of images taken per one surface (Sirkia, 2015)

The outcome of this research (among others) was summarized and published as a conference paper in the Ground Support 2016 conference (Sirkiä *et al.*, 2016).

3 Theoretical background

3.1 Definitions

The parameters which are the topic of this thesis are defined in literature very frequently, however some of the definitions can be confusing. While in case of peak friction angle authors are consistent, the difference between the residual and basic friction angle presents some discrepancies. Some authors define the value of residual friction angle as lower than basic, others equal (Hoek, 2007; Giani, 1992). Graphical representation of presented definitions is shown in Figure 2.

Table 1. Comparison of the definitions of different kinds of friction angle

Parameter	Definition	Source
Peak friction angle ϕ_p	The peak friction angle is evaluated on natural discontinuities, in correspondence to the maximum shear strength determined by roughness failure or overstep	(Giani, 1994)
	Arctangent of the ratio of the peak shear strength to the corresponding apparent normal stress which is equivalent to the arctangent of the ration of peak shear load to the corresponding normal load	(ISRM 2014)
Basic friction angle ϕ_b	Basic friction angle is evaluated on an artificially planar slickenside surface and is characteristic of the rock mineralogy	(Giani, 1994)
	This is approximately equal to the residual friction angle ϕ_r, but is generally measured by testing sawn or ground rock surfaces.	(Hoek, 2007)
	The frictional resistance (ϕ_b) developed between two flat rock surfaces is affected by the mineralogical composition of the material and moisture conditions.	(Bandis, 1980)
	The angle of frictional sliding resistance between particles.	(Barton, 1971)
Residual friction angle ϕ_r	Residual friction angle is evaluated when the shear strength is stabilized on a minimum value. It is obtained on altered and smooth surfaces, by representing the shear strength of the thin alteration discontinuity surface level. This is the lowest value.	(Giani, 1994)
	The residual friction of angle of a non-planar fresh joint may for practical purposes be considered equal to the basic friction angle, thus assuming that roughness is not influential anymore and hence dilation at the residual stage must be zero	(Bandis, 1980)
	The angle of residual sliding resistance of materials which initially were partly or completely intact. It is obtained from asymptotic minimum values of shear strength following large displacements.	(Patton, 1966)
Ultimate friction angle ϕ_u	Arctangent of the ratio of the ultimate shear strength to the corresponding apparent normal stress which is equivalent to the arctangent of the ratio of ultimate shear load to the corresponding normal load.	(Ulusay ISRM/, 2014)
	The ultimate frictional resistance depends on the initial roughness of the joint by contrast to the "theoretical" minimum of ϕ_r. Ultimate friction angle is probably the lowest value which may be obtained by shear testing a rough joint unless asperity strength is low and normal stresses high.	(Bandis, 1980)

	The angle of frictional sliding resistance. For most practical problems involving rocks, the appropriate value of ϕ_u can apparently be obtained after large displacement have occurred along macroscopically smooth and flat but microscopically irregular wet surfaces.	(Patton, 1966)
Dilation friction angle	The slope of the curve of the normal to plastic shear displacement of a fracture exposed to a direct shear test.	(Melin, 2012)

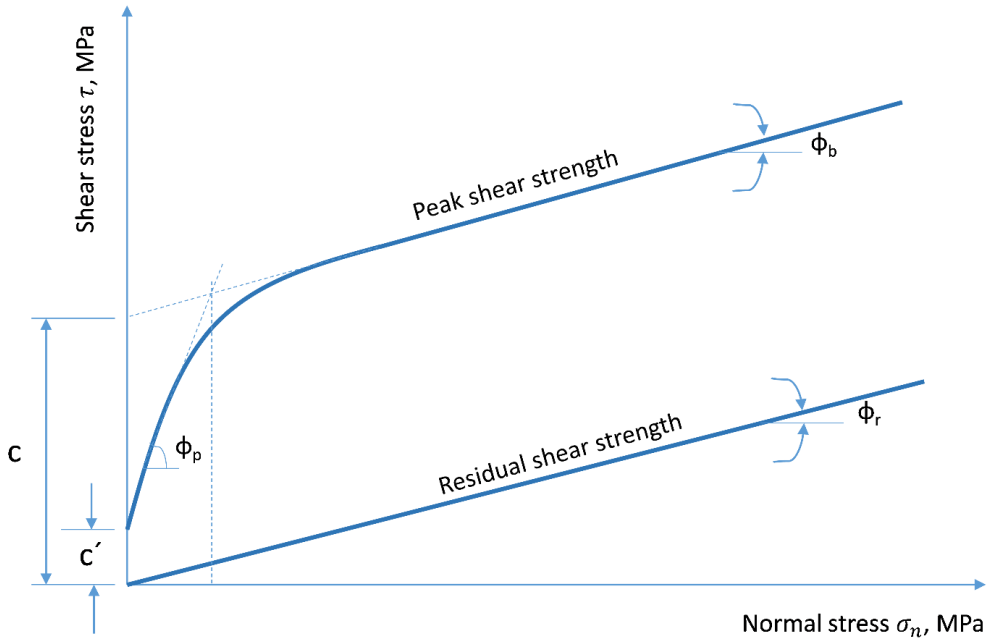

Figure 2 Shear strength as a function of normal stress (modified after (Ulusay and Hudson, 2007)

where:

τ – shear stress
σ_n – normal load
ϕ_p – peak friction angle
ϕ_b – basic friction angle
ϕ_r – residual friction angle
c - apparent cohesion at stress level corresponding to ϕ_b
c´ - cohesion intercept of peak shear strength curve; it may be zero

Depending on a purposes of the design different friction angle values can be used. It is advisable to use residual friction angle when the high safety factor is required, for instance due to the long life span of construction. The application of a residual friction angle is also reasonable when the structure is designed to be made in a rock mass where shear displacements have occurred in the past or are anticipated to occur during the construction phase or if the joints in a rock mass are infilled with a clay material (Bandis, 1980). The usage of peak friction angle in the design calculations can be justified in cases of structures projected for a short term stability or supported long term stability (anchored or bolted slopes). Besides that, peak friction angle can be used for a construction in "clean" unfilled and unweathered joints (Barton, 1973).

According to Hoek and Londe (1974) the temporary structures can be designed for the peak friction angle on condition that all the parameters used in design were verified by the back analysis of the failures that have occurred in a similar material in the past.

3.2 Physics of a shear failure (of discontinuities)

In the process of sliding of one surface over another the friction between the two surfaces plays the crucial role. Friction is a material property usually expressed by a coefficient of friction μ. The coefficient of friction is a parameter which determines the force needed to initiate the sliding on a flat surface. From equations 1 -6 and Figure 3 it can be seen that the friction coefficient is a tangent of the angle of sliding.

The coefficient of friction can be defined by considering a block on an inclined plane. The forces acting on a block are the components of a gravitational force. The component parallel to the incline is the force advancing the sliding of the block. The force preventing the sliding, according to Coulomb (equation above), is the perpendicular component of a gravitational force (normal force – σ_n) multiplied by the coefficient of friction μ. Obviously the block will remain at rest if this forces are in equilibrium, meaning the acceleration of the block is equal to zero. Equations 1-6 present the derivation of the value of friction coefficient.

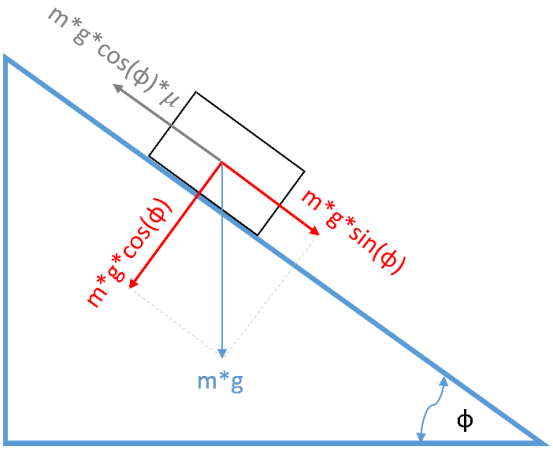

$$\tau = \mu * \sigma_n ; \quad (1)$$

$$m * a = m * g * \sin(\varphi) - m * g * \cos(\varphi) * \mu \quad (2)$$

$$m * g * \sin(\varphi) = m * g * \cos(\varphi) * \mu ; \quad (3)$$

$$\sin(\varphi) = \cos(\varphi) * \mu ; \quad (4)$$

$$\mu = \tan(\varphi); \quad (5)$$

$$\tau = \sigma_n * \tan(\varphi_b); \quad (6)$$

where: m –mass, g – gravitational acceleration

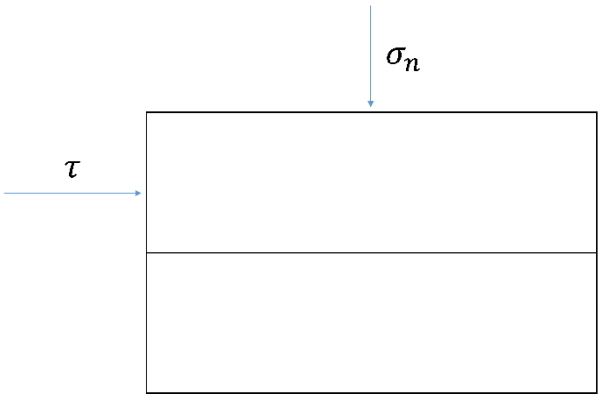

From the Figure 3 and equations 1-6 it can be concluded that the occurrence of a sliding is strongly dependent on a coefficient of friction μ, which is a function of the angle of plane inclination. The inclination for which the sliding starts can be interpreted as a basic friction angle value (Table 1) (Grasselli, 2001).

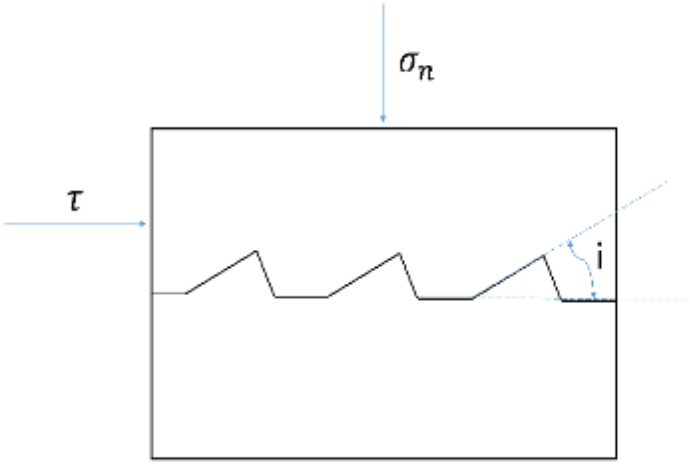

The mechanism of sliding along the planar surfaces is the simplest case. Although the main principle remains the same, increasing roughness of surfaces increases the complexity of a process. In case of non-planar surfaces the friction cannot be described by a coefficient of friction being just a function of basic friction angle, the roughness and geometry of asperities also play a role (Patton, 1966) see equation 7 and Figure 5.

$$\tau = \sigma_n * \tan(\varphi_b + i)\,; (7)$$

Depending on the normal force which has to be overcame to allow the oversliding of asperities and the shear resistance of asperities two failing modes may occur: shearing and sliding. In low normal stress conditions overcoming the friction results in overriding the asperities (sliding over) and therefore in dilation – changes in the normal displacement. On the other hand, if the normal stress is high enough, the work required to break some asperities would be less than the work required to dilate against the normal load, in that case the shearing of asperities will occur.

For that case the Patton´s equation is applicable (Patton, 1966):

$$\tau = c_j + \sigma_n * \varphi_r; \quad (8)$$

c_j – apparent joint cohesion
φ_r – residual friction angle

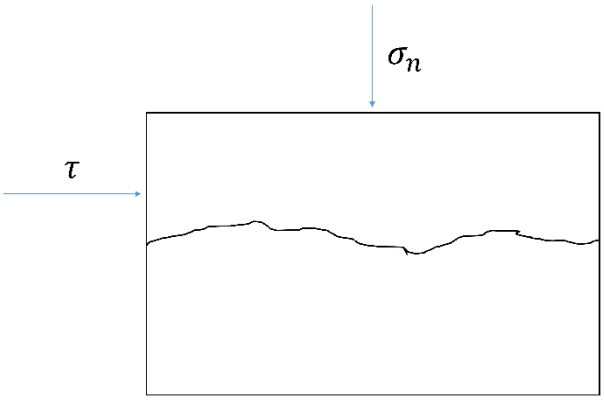

However “saw tooth” model (Figure 5) of a joint brings us closer to reality it is still a simplification. For most natural rough joints failure envelope is not bilinear but continuous (Grasselli, 2001).

This case can be described by Barton´s equation for shear resistance of rock joints (Barton and Choubey, 1977):

$$\tau = \sigma_n \tan(\varphi_r + JRC log_{10}\left(\frac{JCS}{\sigma_n}\right)); \quad (9)$$

JRC – joint roughness coefficient
JCS – joint compressive strength

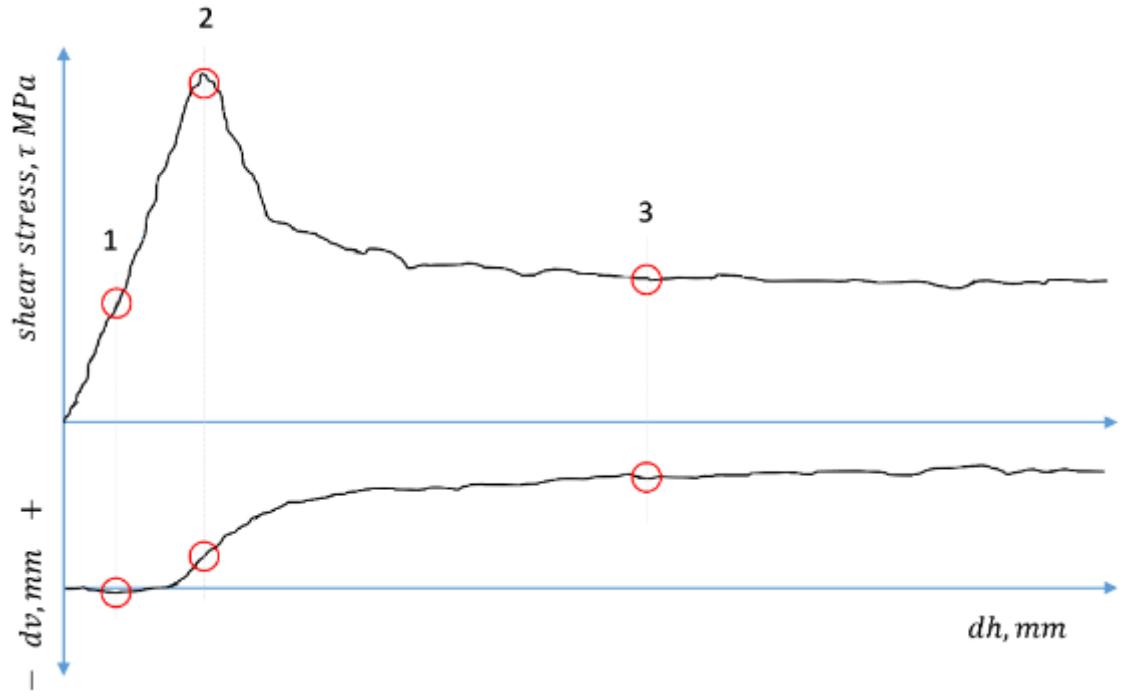

In practice, for the joints in a rock mass, the sliding over asperities is possible only in very low normal stress conditions, such as in the slopes of open pit mines.

In the majority of cases, the energy input required for dilation is higher than the energy input required for a shear failure to occur (Bandis, 1980). Even at low normal stresses some failure may occur at the tips of asperities in contact (Barton, 1971).

The measure of dilation is termed as dilation angle i and is defined as an inclination of the shearing path relative to the mean plane (arcus tangent of the ratio of vertical displacement to horizontal displacement ($i=\arctan(d_v/d_h)$) (Table 1). Peak dilation angle refers to the inclination of the shearing path at the peak shear strength in relation to the mean plane and it expresses the minimum energy path between a sliding over and shearing through mode of failure at a given normal stress (Barton, 1971).

It is typical for the rough natural joints that the maximum dilation occurs near the peak shear strength (Figure 7). Figure 7 shows the shear behavior of a joint, its shear strength and respective vertical and horizontal displacement. At the point one, the stress strain curve corresponds to the closure and elastic behavior of a joint, which might be an explanation for the negative vertical displacement. At the point two joint reaches its peak strength mobilization. On this level of shear stress the failure or overriding of the asperities occur, it can be observed that in the vicinity of a peak shear strength the inclination d_v/d_h is the highest on the whole curve – the dilation angle reaches its maximum value. Section 2-3 in Figure 7 corresponds to the post peak behavior, the joint continues to dilate but at significantly reduced rate. From the point three further, nearly horizontal part of the curve represents the residual behavior, the shear strength reaches its residual value and the dilation angle approaches zero.

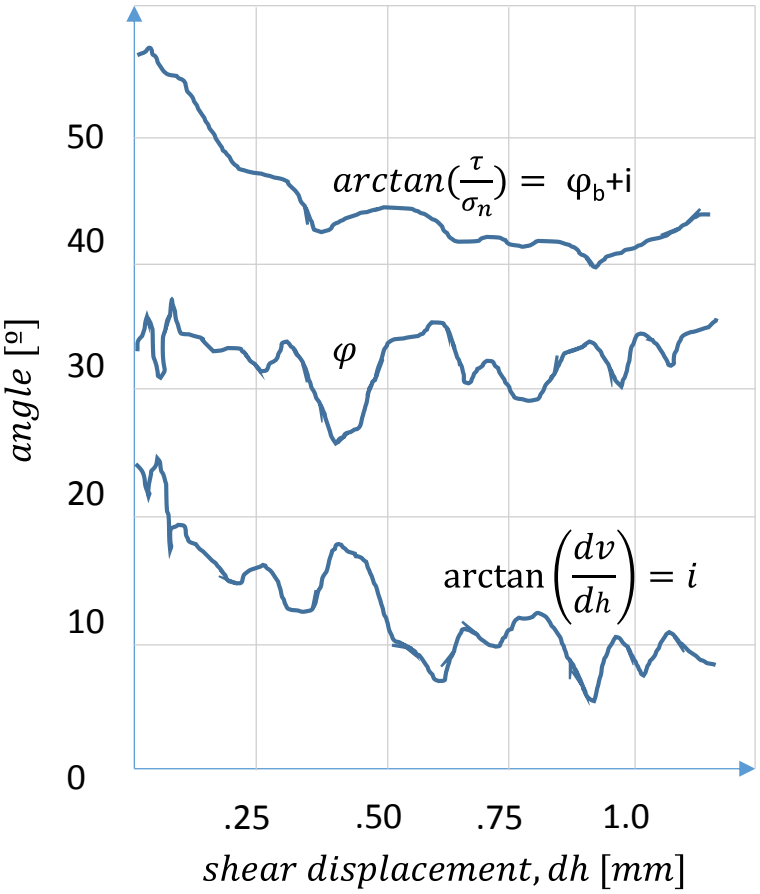

Figure 8 Relation between dilation angle and friction angle (modified after Barton, 1973)

Figure 8 Represents the relation between the total frictional resistance of a joint of a joint ($\arctan(\tau/\sigma)=\varphi_b+i$) and the dilation angle ($\arctan(d_v/d_h)=i$) in the constant normal load conditions and the difference between those two angles $-\varphi_b$. That relation illustrates the fact that increasing roughness of a joint leads to the decreasing dilation rate

The term normal stiffness (K_n) was introduced in 1968 by Godman et al. to describe the stress-strain character of joints under normal loading conditions. The term is defined as the normal stress per unit closure. K_n is equal to the increase in the normal load on a shearing plane caused by the tendency of a rough joint to dilate (Meemun and Fuenkajorn, 2015).

In the instances when the normal displacement of a joint is restricted (constant normal stiffness conditions – CNS, $K_n <> 0$) the tendency of a joint to dilate increases the normal stress acting on a joint and shear displacement can only occur in meaning of the failure of asperities. In cases when the dilation is allowed due to the open external boundaries or /and low normal stress (constant normal load conditions – CNL, $K_n = 0$) the joint is forced to slight up at an angle to the mean shearing direction, shear, therefore shear displacement can only occur as an effect of sliding over the asperities (Iakovlev *et al.*, 2015; Bandis, 1980; Meemun and Fuenkajorn, 2015; Poturovic, Schubert and Blumel, 2015). Constant normal load and constant normal stiffness conditions are illustrated in figure 9 below.

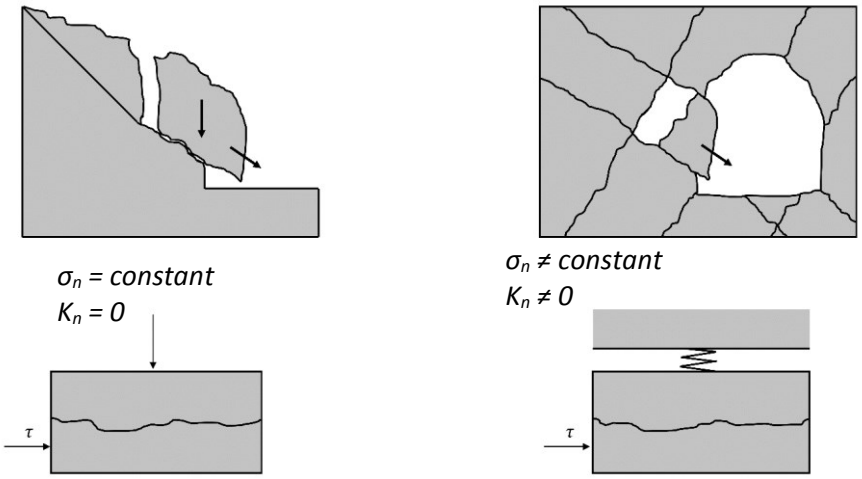

Figure 9 CNL (left) and CNS (right) conditions (modified after Van Nguyen and Konietzky, 2014)

The one dimensional dilation will be suppressed in case when the effective normal stress acting on a joint surface reaches the value of confined compressive strength/critical effective confining pressure ($\sigma_n = \sigma_1 - \sigma_3$) (Barton, 1976). – critical state concept – Barton 1976, Barton and Choubey, 1977

It is possible for two modes of failure, "sliding – up" and "shearing through", to occur one after another in the following cases: after reaching the peak shear strength, when the angle relative to the mean shearing plane changes or the value of normal stress changes. A joint might cease to delate after overcoming its peak shear strength, when the asperities are sheared off, the mode of failure changes from shearing to sliding. In low normal stresses joint might continue to dilate after reaching its peak shear strength if the angle is reduced (Barton, 1973).

3.3 Review on roughness assessment methods

Input data for methods presented in 3.3.1 and 3.3.2 is the cross sectional profile of analyzed surface. Input data for method presented in 3.3.3 is the triangulated digital model of a surface. In this thesis both cross sectional profiles and digital models of joint surface were created using close range photogrammetry. Both surface length and slope measurement methods presented in 3.3.1 and 3.3.2 use the value of Joint Roughness Coefficient (JRC), which is a curve fitting parameter, well known and commonly used in the world of rock mechanics. This method is based on visual comparison of real joint profile and standard profiles developed by Barton and Choubey (1977). JRC values determined with this method range from 0 for smooth profile to 20 for the roughest profile.

3.3.1 Surface length method (2D)

The surface length method is based on a statistacal approach and was introduced by Maerz and coworkers (1990). The slope length measurement describes correlation between the JRC and Roughness Coefficient (R_p). The roughness coefficient $R_p$was defined as a ratio of real profile length $L_t$to nominal profile length L_n (Sirkiä, 2015).

$$R_p = \frac{L_t}{L_n} = \frac{\sum_{i=1}^{N-1} \sqrt{(x_{i+1} - x_i)^2 + (y_{i+1} - y_i)^2}}{Ln} \; ; \tag{10}$$

Where (x_i, y_i, x_{i+1}, y_{i+1}) represent the coordinates of a respective point of cross sectional 2D profile of joint surface. N stands for the total number of points in line profile. The relation between the R_p and JRC is described by Maerz as follows:

$$JRC = c(R_p - 1); \tag{11}$$

Where c is a constant value ranging from 400 to 411.

3.3.2 Slope measurement method (2D)

The slope measurement is also a method based on a statistical approach which was proposed by Tse and Cruden (1979). The slope measurement describes a correlation between the JRC and the parameter Z_2. Z_2 is defined as a root mean square (RMS) which is estimated from the 2D profile of a joint surface by taking into account local slopes with intervals between the data points on a profile:

$$Z_2 = \sqrt{\frac{\sum_i^{N-1}(z_i - z_{i+1})^2}{(N-1)ds^2}}; \tag{2}$$

Where z is the height of a profile above the reference line, N is the quantity of measures and ds is the interval between measures. The correlation between the Z_2 and JRC was described by Tse and Cruden as follows:

$$JRC = 32.3 + 32.47 \log(Z_2) \; ; \tag{13}$$

3.3.3 Directional roughness assessment (3D)

A method for 3D directional roughness assessment was presented by Tatone and Grasselli (2009). The roughness parameter described by this method is dependent on a spatial distribution of asperity angles with respect to the direction of shearing. To conduct that analysis the digital model of joint surface is required. In the roughness analysis according to Tatone and Grasselli (2009) the best fit plane is created for a digital model of a joint surface. Next, the orientation of each triangle forming the surface model is analyzed by assigning the triangle dip (θ) and azimuth (α). The dip is the maximum angle between the best – fit plane and certain triangle, while azimuth is the angle between the projection of the true dip vector (d) and the shearing direction. The principle is illustrated in figure 10.

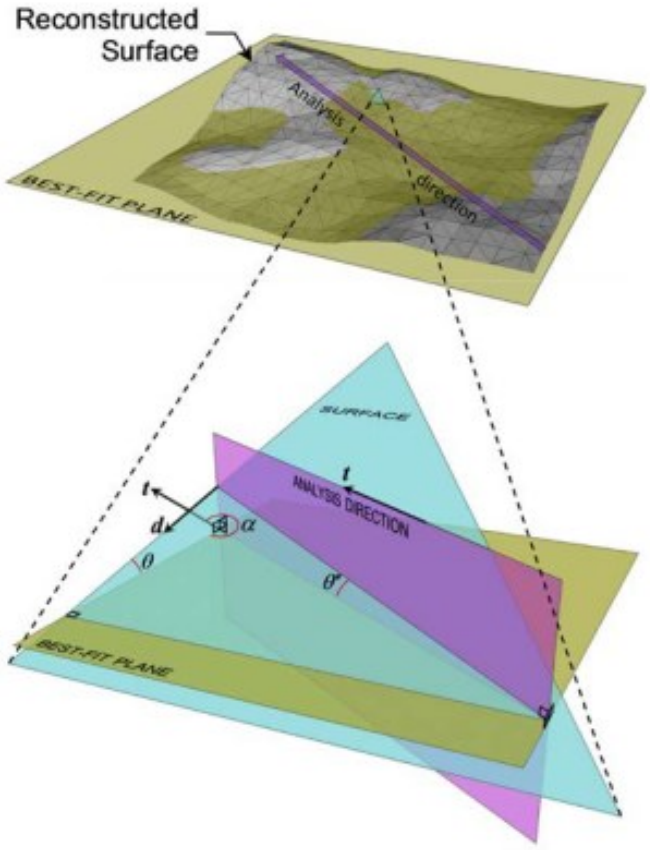

Figure 10 Principle of the directional 3D roughness assessment method (Tatone and Grasselli, 2009)

During the analysis the fraction of area which is more inclined than a certain threshold is defined. That fractional area is referred to as normalized area ($A_{\theta*}$) and the threshold is referred to as θ*. Also the fitting parameter C is defined during the analysis. Authors propose two parameters as a metrics of surface roughness:

$$\frac{\theta^*_{max}}{C+1}; \quad (14)$$

$$2A_0 * \frac{\theta^*_{max}}{C+1}; \quad (15)$$

Where, A_0 is the normalized surface area steeper than 0º, θ^*_{max} is the maximum apparent dip angle of surface in the shearing direction and C is a dimensionless fitting parameter. The directional roughness analysis allows also to estimate the residual friction angle of a joint without any schistosity in **CNS** conditions (Grasselli, 2005):

$$\varphi_r = \varphi_b + \left(C * A_0^{1.5} * \theta^*_{max} * \left(1 - A_0^{\frac{1}{C}} \right) \right); \quad (16)$$

The detailed description of the method with examples can be found in (Tatone and Grasselli, 2009)

3.4 Main principles of close range photogrammetry and image processing

The use of photogrammetry for a measurement of a rock join surface roughness was first proposed by Wickens and Barton (1971) and ISRM (1978). The method developed then is still of use and was published in 2014 as one of the ISRM suggested methods for determining the roughness of a joint surface. Among the systems providing 3D data for surface roughness evaluation photogrammetry is one of the cheapest (Unal, M., Yakar, M., Yildiz, F., 2004). Constant development in the digital cameras industry and state of the art of Free and Open Source Surface (FOSS) allows to achieve high accuracy of the results with minimal expenses.

3.4.1 How photogrammetry works

In principle, close range photogrammetry is a process of creation 3 dimensional digital models of any object. That process can be divided into three basic steps: project planning, image acquisition and image processing. In short, during that process 3-D world coordinates of an object are converted into 2-D flat coordinates by photography and then they are converted back into 3-D coordinated by image processing. Obviously, some information about the depth is lost during the photographic process, for that reason at least 2 pictures taken from different directions are required to reconstruct the 3 dimensional coordinates of an object. Process of reconstructing 3-D coordinates from a set of pictures taken with different camera positions is called bundle adjustment. Bundle adjustments starts with determining the position and aiming of the camera for each picture. Next, the lines (so called lines of sight connecting each camera position with each point on the object are developed. Finally, lines of sight are intersected by aerial triangulation is conducted to produce 3 dimensional coordinates of each point within the model. The principle of bundle adjustment is shown in figure 11.

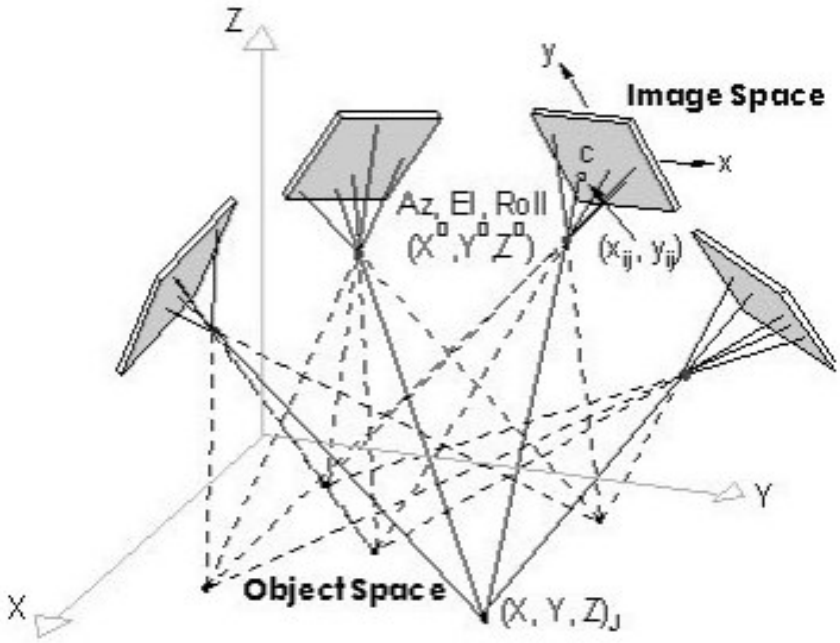

Figure 11 Bundle adjustment

3.4.2 Accuracy in photogrammetry

The accuracy of photogrammetry is mainly dependent on the quality of the photographs and the procedure of imaging itself. According to the author of the thesis, parameters controlling the precision of the model can be divided into three categories and include:

a) Equipment related:
- **resolution of the camera (sensor pixel size)**,
- type of the lens

b) Environment related:
- the size of the measured object
- lighting conditions

c) Procedure related
- **distance from camera to the object,**
- number of pictures
- camera intersection angle
- camera settings (ISO speed, aperture, is the tripod used?)

The accuracy of the result can be controlled by adjusting those parameters, yet since most of the parameters are mutually depended on each other changes must be done thoughtfully because change in one parameter implies the change in the others. Accuracy control in the close range photogrammetry project means finding the optimum for the set of parameters. Two parameters critical for accuracy of the final results are the camera resolution and the distance from camera to object. Case of the camera resolution is quite straightforward, one should always aim for the highest available resolution, considering the required accuracy and economical aspect of the project.

When it comes to distance between photographed object and camera, the first approach is to aim for the smallest distance to minimize the fraction of the picture containing the information irrelevant for the project (surroundings). Though, there are parameters on which the distance camera – object is dependent as well as there are parameters which depend on this distance (Figure 12). That makes finding the optimal camera – object distance a complex procedure.

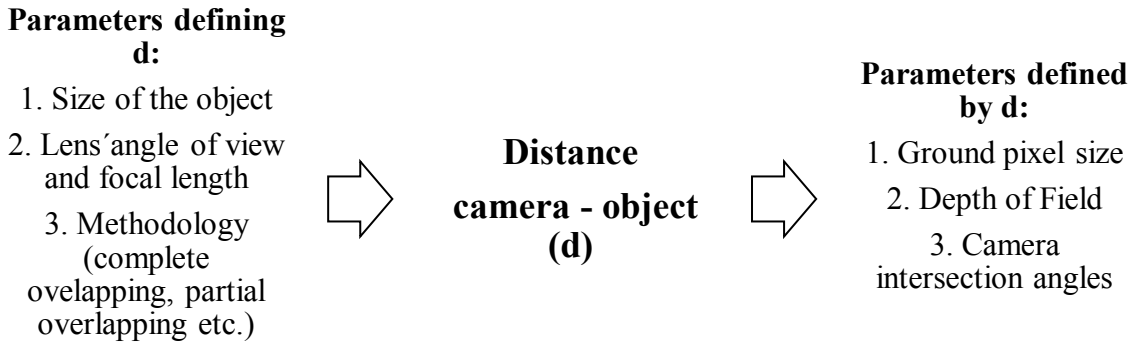

Figure 12 Relation between the camera object distance and other accuracy parameters

The relation between the size of the object and distance from object to camera is ruled by the lens type and the photogrammetric measurement method. In this thesis, the measurement method of photogrammetry is complete overlapping, since is a method recommended by Sirkiä (2015). In other words, the aim is for every picture taken to contain entire object to be measured. Consequently, the bigger object is the further camera should be positioned in order to capture entire object in the picture. Next influential factor is the type of the lens, more specifically its angle of view. In case of small object surfaces macro lenses with large angle of view and short focal length would allow to decrease the distance between object and camera and improve the accuracy. Lenses with very narrow angle of view are not recommended for close range photogrammetry projects. On the other hand, wide angled lenses tend to have bigger distortion which is a big disadvantage when it comes to accuracy.

Distance between the camera and the object to be measured has a direct influence on the critical accuracy parameters. Firstly, it defines the maximum resolution of the picture, this is the ground pixel size (GPS). Figure 12 shows the projection scheme of the digital camera, it can be concluded that the proportion of the camera´s focal length to the distance between the camera and photographed object is equal to the proportion of the sensor pixel size to the ground pixel size. This relation is expressed by equation 17. With known image pixel size and estimated pixel accuracy it is possible to estimate the accuracy of the image. Naturally the smaller ground pixel size the better. Theoretically, the smallest achievable ground pixel size is equal to the sensor pixel size, in cases when the distance between the object and camera is equal to the lens' focal length. This could be only possible in cases where the object´s surface is small and wide angled lens is used. Yet it is very challenging to capture the whole surface to be measured from such a small distance, on the top of that, the aim is not only to capture the whole object´s surface on the picture but also for the image to be sharp. This is where the Depth of Field comes into play.

$$pixelsize_{image} = \frac{d}{f} * pixelsize_{sensor}; \quad (17)$$

where:

$pixelsize_{image}$ – size of the pixel on the images

$pixelsize_{sensor}$ – size of the pixel on the image sensor

d – focus distance: object – camera

f – lens´ focal length

Depth of Field is a term which is used to describe the sharpness area of a picture. That is defined by the near and far distance of sharpness. Values of this distances are dependent on the distance from camera´s optical center to the object, aperture value and the circle of confusion. It is important to notice that the sharpness distances calculated for the set up where the camera is positioned at an angle to the horizontal plane, the sharpness area is inclined to the object surface as well. When determining optimal shooting distance it is important that as large as possible part of the object surface fits into the sharpness area. The aperture value should be adjusted according to the required DoF area. The method to calculate depth of field is shown by equations 18-20 below

Since the images will be used to convert 2D images into 3D model the accuracy in all directions should be as good as possible. In case of rough rock joint surface the elevation of the asperities is ccrucial in the roughness assesmen, therefore the accuracy in vertical direction. To ensure that, the camera intersection angle (Figure ddd) should not be too stee. It is advised that this angle is not less than 60°.

$$D_n = \frac{s(H-f)}{H+d-2f}; \quad (18)$$

$$D_f = \frac{s(H-f)}{H-d}; \quad (19)$$

$$H = \frac{f^2}{F*c} + f; \quad (20)$$

Where:

d – focus distance: camera – object

Dn – near distance of sharpness

Df – far distance of sharpness

DoF – whole depth of field area

α – camera´s line of sight inclination

H – hyperfocal distance

f – focal length of a lens

F – aperture, f-stop

c – circle of confusion

4 Description of the sample

4.1.1 Dimension, mass, density

Rock type: Grey Kuru granite

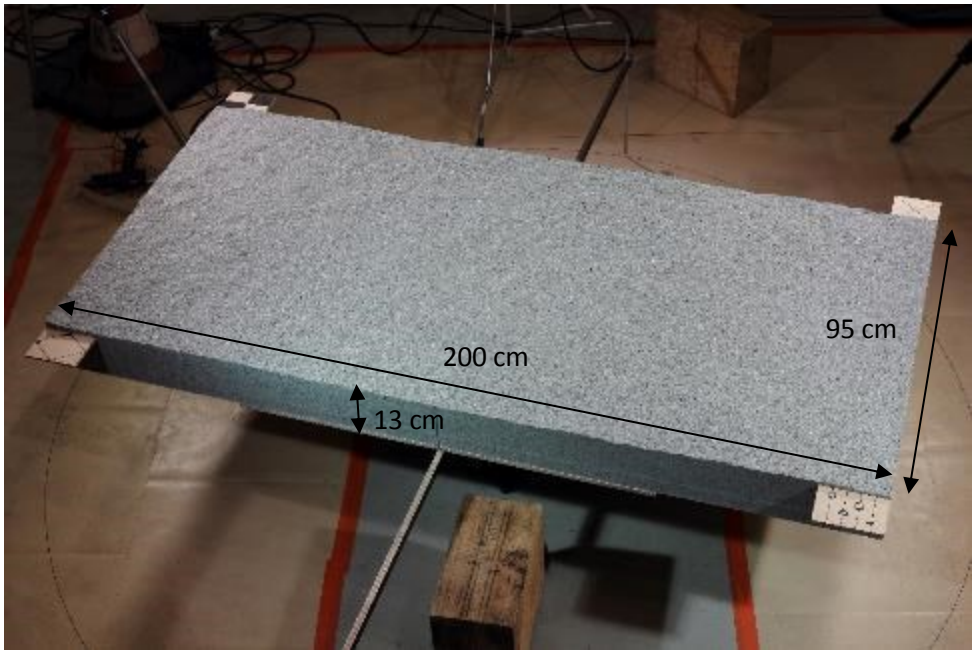

Figure 13 Dimensions of the sample (picture made during photogrammetry of the bottom part of the sample.

The density of rock: 2.67 kg/m^3

Mass of the bottom half of the sample: 660 kg.

4.1.2 Manufacturing and preparation

a) Step 1 – drilling.

Prior to the splitting, the holes were drilled in the boulder to enable hammering in the wedges. The drilling was done using a hand held drill bit. The drilling pattern was designed based on the crew´s experience, the distance between the holes was approximately 15 cm. The holes were drilled on the line representing the projected crack.

Step 2 – hammering in the wedges.

As the next step, the 10 cm long wedges were put in the holes and were gradually hammered in with a rubber hammer. At this stage it was possible to observe the creation of the initial crack (Figure 17. The direction of the propagation of the crack was indicating which wedges should be hammered in deeper.

Step 3 – Removing the wedges.

After the crack has propagated throughout the whole boulder the wedges were removed one by one. It was possible to remove them without any tools.

Step 4 – Splitting.

After the wedges were removed and the whole boulder was cracked the two parts were split manually using a wrench.

b) Step 5 – Sawing.

The split parts were transported separately with a fork lift to the sawing hall, where they were cut to the desired dimensions. The parts affected by drilling and wedging were cut out. Final measures of the sample are 2000 x 950 x 120 mm for each half.

4.1.3 Joint roughness and matedness assessment

As it has been pointed out by Tatone and Grasselli (2009) most studies on the shear strength of discontinuities are conducted on small joint surfaces (less than 1 m^2). Consequently, the contribution of large scale asperities is not taken into account. The differentiation of roughness components according to the scale was introduced by Patton (1966) who distinguished two types of asperities: first order asperities and second order asperities. First order asperities represent the large scale undulations, so called waviness, and second order asperities represent small scale roughness, so called unevenness (Giani, 1992). Figure 20 shows first and second order asperities introduced by Patton (1966) and Figures 21 and 23 shows the first and second order asperities on a tested joint.

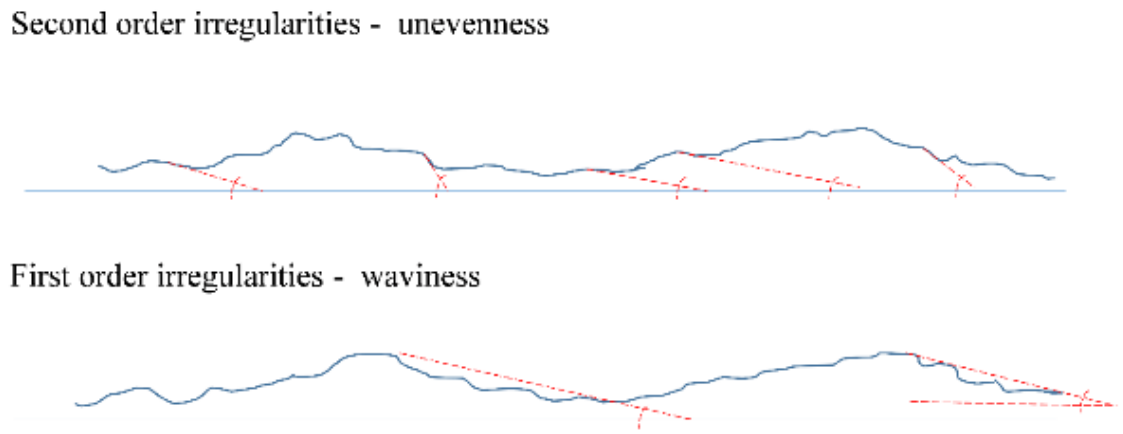

Figure 20 First and second order asperities (modified after Patton 1966)

Joint surface 1,9 m^2 allows both orders of asperities contribute to the shear strength of discontinuity.

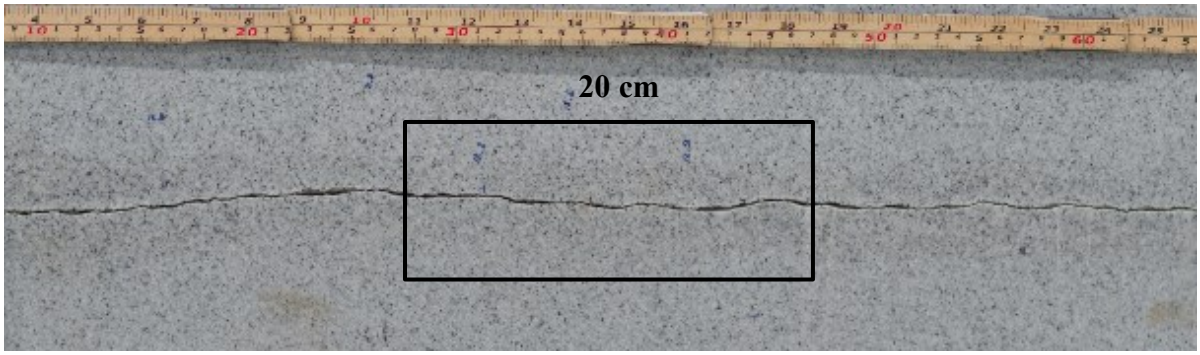

a) Firt order irregularity of base length about 60 cm. Apparent waviness can be observed in this fragment of a sample.

b) The picture shows the fragment of discontinuity highlighted with black frame in the picture above. Here the small, second order asperities can be observed representing the unevennes of the joint.

Figure 21 Waviness and unevennes of the joint surface, sample 2000 x 950 mm.

a) Side view of the sample. First order asperities can be observed throughout the whole length of the sample (2000 mm). Black frame represents the fragment of a joint which is showed on the Figure 21 a)

b) Opposite side view of the sample. It can be noticed that joint on this side is “smoother” and the waviness is less apparent than in the picture above.

Figure 22 Side views of the sample size 2000 x 950 mm

The fracturing process described in chapter 4.1.2 requires splitting two parts of the boulder and putting them back together after sawing. As a results the opposite sides of a joint do not match together perfectly and some damage zones can be observed within the length of a joint (Figure 23).

Figure 23 Mismatching part of a joint. Debris is infilling the space where discontinuity is not matching.

The gap distance between the opposite sides of joint the within the whole sample has been measured using digital caliper. The biggest gap distance is equal to 4,3 mm, the smallest – 0,3 mm (see sigure 24). Figure 25 shows the spatial distribution of the gap distance along the edges of the sample

Figure 24 Measuring the gap distance of a joint (in this case it is just the damaged edge).

The poor matedness of a joint has and influence on the scale effect study. As it has been mentioned in chapter 3.2 several theories exist according to which the scale effect is a result of difference in the contact area for different sample sizes (Pratt, 1974; Johannson and Stille, 2014).Obviously, for not matching joint the relative contact area decreases with increasing size, therefore the pressure on asperities in contact is higher and failure occurs easier than in case of smaller sample. The creation of fracture with perfect matedness is from author´s point of view the biggest challenge in experimental study of the scale effect.

<	0,5	
0,5	1,0	
1,0	1,5	
1,5	2,0	
2,0	2,5	
2,5	3,0	
3,0	3,5	
3,5	4,0	
>	4,0	

Key for the inner graph

<	1,0	
1,0	1,5	
1,5	2,0	
>	2,0	

[mm] Key for the outer graph [mm]

Figure 25 Spatial distribution of the gap distances throughout the entire sample. For 2000 mm long side 96 and for 950 mm long sides 44 measurements have been taken which results in the increment of approximately 20 mm.

It can be noticed the big values of gap are concentrated in the left upper corner of the figure. It might indicate that the splitting was done from this side.

Four hypothesis explaining the poor matedness of discontinuities:

- Loose pieces of rock filling the joint gap not allowing the joint surfaces to match closely,
- Damage zones are located mostly on the edges since this part is mostly prone of being chipped and damaged during transport or sawing.
- Sample halves not placed perfectly at the top of each other.
- Damage done to the sample during the transportation and handling process.

5 Methodology

5.1 General description

As the title of the thesis states, the aim of the experiments is to validate the value of friction angle determined using photogrammetry. The validation in this study means the comparison of the values of peak and residual friction angle achieved in two ways – by analyzing the digital models of the joint surface created with photogrammetry and by analyzing the results of multistage shear testing. The chronology of the steps is shown in figure 26.

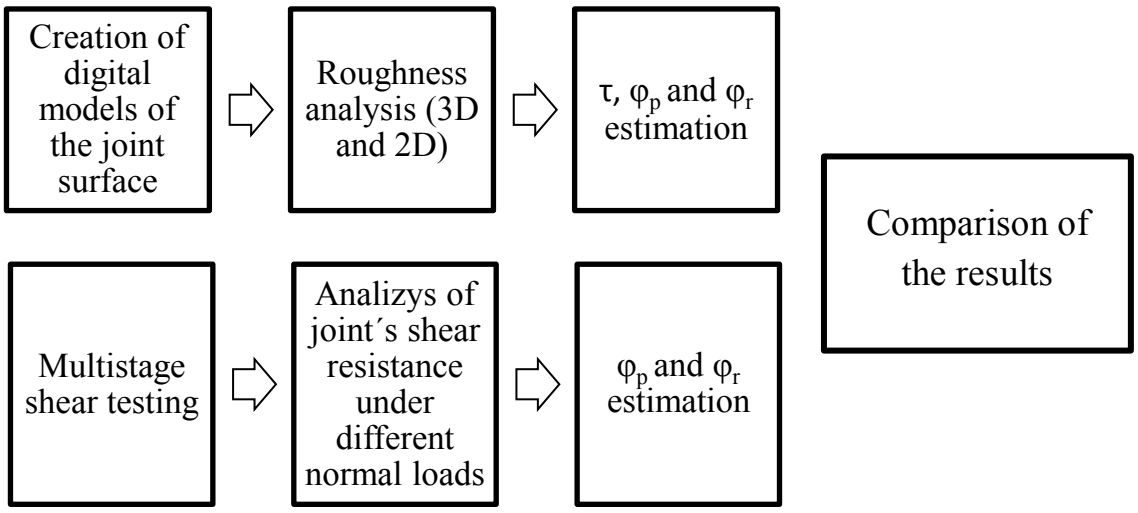

Figure 26 General description of the methodology

Tilt, push and pull tests were considered as an options for the testing method (Figure 27). Tilt test was eliminated as first due to technical problems concerning the set up and high risk of damage of equipment and the sample during the experiment. The typical value of peak friction angle for a fresh joint in granite is around 75° The granite plate of significant mass and dimensions inclined at this angle could pose a serious risk of the damage to equipment in case of its sudden displacement.

The push and pull experiment would employ similar equipment and methodology, but one drawback of the push set up was identified during the planning of experiment. Namely, since the push test would require direct contact of the slab and hydraulic cylinder, due to the high stiffness of the whole set up and uneven surface of the joint, accumulated energy could be released by lifting the sample up instead of displacing it horizontally. To mitigate this risk, it was necessary to increase the distance between the sample and hydraulic cylinder and decrease the stiffness of whole set up to ensure smoother release of accumulated energy. That led to decision that most suitable methodology for this sample size is pull test incorporating hydraulic cylinder and a steel chain.

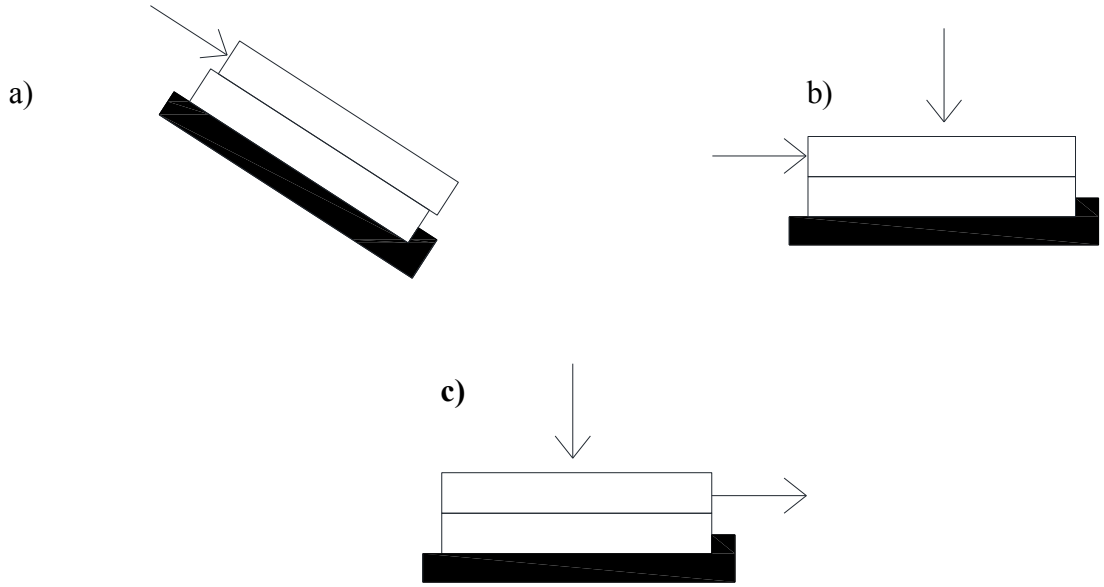

Main principle of the pull test on the rock joint is to apply the pull force at a certain rate on the upper part of the sample half while restraining the movement of the lower sample half The applied force is increased until the peak shear strength is reached and the shearing is continued until the shear strength reaches its residual level and the required shear displacement is reached.
The purpose of the pull experiment was to determine values of peak and residual friction angle. In order to do that, shear strength of a joint was measured for three different values of normal load (Figure 28). Test was designed to imitate the constant normal load (CNL) conditions, meaning the normal load was small enough to allow the vertical displacement of the sample. Lateral displacement of the sample was constrained.

The results of pull experiment include the value of residual and basic friction angle of a joint, its peak and residual shear strength, dilation during each stage of shearing and spatial analysis of damage after each shearing stage.
Additionally to the test, the joint surface geometry was analyzed using photogrammetry. That analysis included photographing both surfaces of a joint (top and bottom part of a sample) before and after the pull test was done. Next, acquired images were processed into the point clouds which were then triangulated into DTM surfaces. In sum, 4 digital models of join surface were made: top sample before test, bottom sample before test, top sample after test and bottom sample after test. In the last step, surfaces models were analyzed in terms of roughness. Based on the results of that analysis, the value of peak and residual friction angle were calculated. Finally, the results from both methods were compared.

The chronology of executed tasks looked as follow:

1. Image acquisition
2. Multistage shear testing
3. Analizys of joint´s shear resistance under different normal loads and φ_p and φ_r estimation (from shear experiment)
4. Creation of digital models of the joint surface
5. Roughness analysis (3D and 2D) and τ, φ_p and φ_r estimation
6. Comparison of the results.

The reason why photogrammetric prediction of joints roughness, shear strength and friction angle was not done before the shear test was due to the time constraints involved in the project.

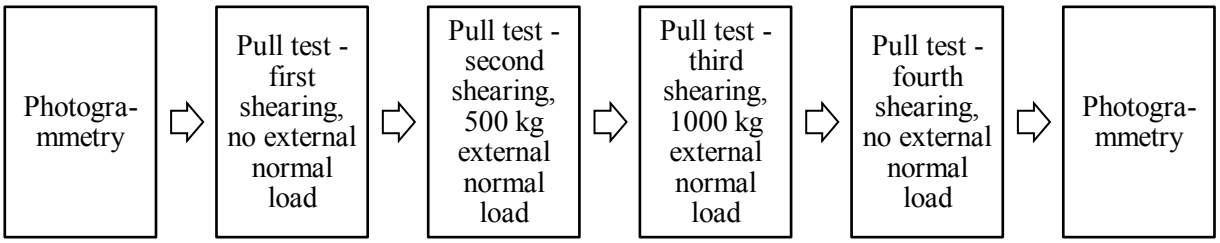

Figure 28 Workflow for the experimental study

DELIVERABLES FROM EXPERIMENTAL STUDY – <u>peak and residual friction angle of a joint</u>, peak and residual shear strength of a joint, dilation during each shearing stage, spatial damage analysis

A methodology of image acquisition I used in this study is a slightly modified version of methodology developed during the KARMO II project by Joni Sirkiä. Detailed description of it can be found in his Master´s Thesis (Sirkiä. 2015). Similarly, the technique of surface creation and the roughness analysis methods implemented in this thesis were developed during the previous stages of KARMO, the descriptions of those methods can be found in (Sirkiä, 2015; Uotinen et al 2015; Sirkia et al 2016) and are described in chapter 5.2.2 of this thesis.

The Figure 29 below presents the workflow of photogrammetric prediction of friction angle.

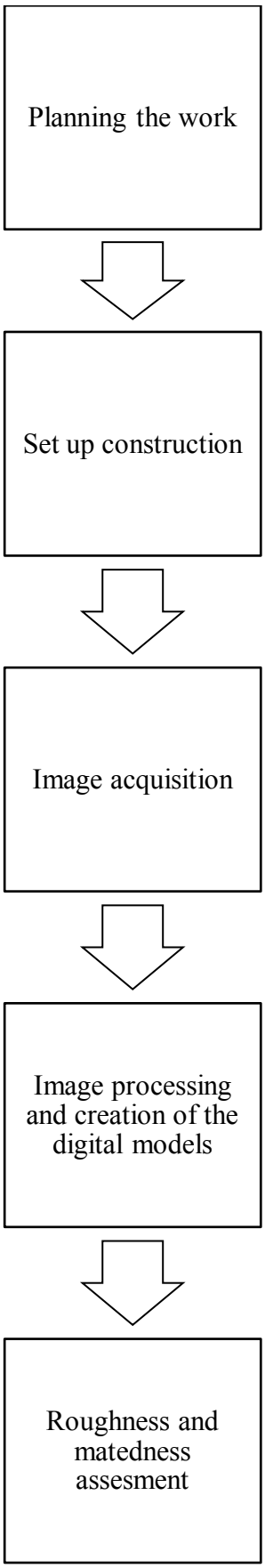

- Planning the work set up
- Planning the configurations of camera position

DELIVERABLES – Work plan

- Building rotational table
- Setting up the angle measurement system
- Fixing the sufficient lighting

DELIVERABLES – Work set up

- Adjusting the object camera distance accordingly to required Depth of Field and pixel size on the image
- Taking pictures using 5 different configurations of a camera

DELIVERABLES – Images of both (top and bottom) surfaces taken before and after the pull test, in total over 3 600 pictures in RAW format.

- Converting image files from RAW to JPEG
- Adjusting the brightness and sharpness of the pictures
- VisualSFM sparse and dense reconstruction
- CloudCompare point cloud cropping and DTM creation

DELIVERABLES – 4 point clouds (4 .PLY files) and 4 DTM models of joint surface (4 .STL files)

- Sectioning the models
- Slope measurement and surface length JRC estimation
- Directional roughness assessment
- Barton –Bandis friction angle calculations

DELIVERABLES –directional roughness of sample surface, JRC values for joint surface, colormaps of the joint surface

Figure 29 Workflow for the photogrammetric prediction.

5.2 Photogrammetric prediction of joint roughness and friction angle

5.2.1 Set-up and image acquisition

One of the results of previous studies done for KARMO II (chapter 2.2) is the methodology of taking pictures of a sample from multiple angles in a very efficient way. Sirkiä used rotational platform attached to the floor at its central point to take pictures of the rock sample using multiple camera positions. This method allows to acquire images without changing the actual position of the camera for every picture taken. Instead, the relative position of camera to the sample is changed by rotating the sample 360º and taking a picture at every certain interval. In this studies, I used analogical methodology, but due to the bigger mass of the sample we replaced the rotational platform with more sturdy construction – turning table (Figure 32). As a turning mechanism we used the wheel bearing, as a sample holder – 90 x 60 cm steel frame (profile type IPE 120). The frame size ensures that the deflection of the sample is negligible. On the top of the steel frame we placed a plywood plank. The purpose of the plank was to enable positioning the sample correctly, so the center of the sample would be placed exactly in the center of a frame. Additionally we used the wooden plank to mount the angle measuring bars. (Figure 31) In this studies I took 180 pictures per one full 360 º revolution, meaning that each pictures were taken after turning the sample by 2º clockwise. To measure the angle of rotation I drew half circle on the floor with a center exactly in a center of a turning table and made marks every 2º. Thanks to the bars attached to the table it was possible to rotate the sample precisely by 2º. To create a photogrammetric model of a surface it is not enough to take pictures "all around" the sample, it is also necessary to change the vertical position of a camera, it is its height and angle. I used five different configurations of vertical camera position combining 4 different angles and 2 different heights to photograph one rock surface. Table 2. For each one of this configurations 180 pictures (full sample revolution) were taken. That sums up to 900 pictures per one joint surface.

The camera with a tripod was placed on a stable scaffolding at the height of approximately 150 cm. (Figure 30) It was necessary in order for the sample to fit in the image frame. The range of changes in camera´s angle was limited by the sample size. The height of a camera was changed by regulating the height of a tripod. I was taking pictures from the floor level using a remote control so any possible movement of the camera.

Obviously, the distance between the sample and camera was changing together with changing vertical camera position. That is why for each configuration I calculated the distance from camera to the sample and selected the correct aperture which ensured that the sample fit in the near and far distance of DoF and the sample was in the sharpness zone. The camera was focused on 2/3 of the sample length therefore the minimal value for near DoF distance was 66.7 cm and for far DoF distance 133.3 cm

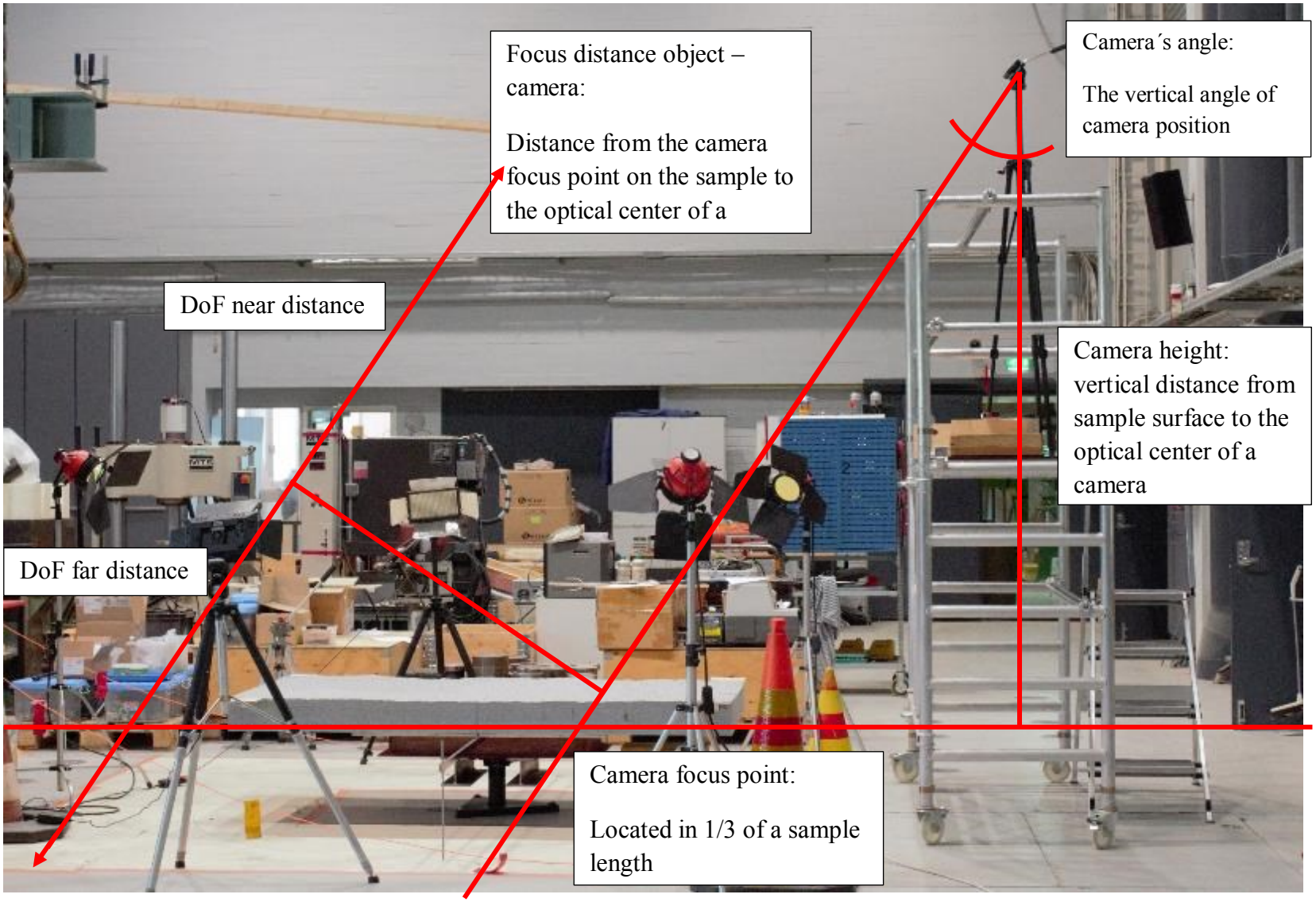

Figure 30 Photogrammetry setup, for values see table (for exact dimensions see table 2).

Figure 31 Sample on a turning table during photogrammetry (top part of a sample, after pull test)

Figure 32 Construction of a turning table

Table 2. Camera configurations during the picture acquisition process.

Configuration camera angle, camera height	Distance camera – object [cm]	f-stop	Depth of field [cm]	$pixelsize_{image}$ [mm]
35^0, 326 cm	334,5	f11	Dn – 70,6 Df – 264,3	0,41
40^0, 326 cm	357,7	f8	Dn – 65,0 Df – 184,2	0,44
40^0, 299 cm	322,4	f9	Dn – 81,1 Df – 147,5	0,40
45^0, 299 cm	349,3	f8	Dn – 74,3 Df – 185,0	0,43
50^0, 299 cm	384,3	f5,6	Dn – 73,8 Df – 147,2	0,47

I used Canon 600D camera and Canon EF 35 mm f/2.0 IS USM lens. The sensor size of a camera is 22.3 x 14.9 mm, its maximum resolution is 5 184 x 3 456 pixels which results in 4,3 μm sensor pixel size. The cameras circle of confusion is 0.019 mm. The focal length of the lens is 35 mm. Used lens is characterized by a negligible distortion (-0.2% barrel distortion) and very good performance towards distortion for aperture values not smaller than f/11. Aperture f/11 was the smallest value I used during this study, so it can be said that the quality of the pictures was not affected by diffraction.

I chose semi-automatic mode of shooting which enables the camera to select the optimal exposure time for the lighting conditions. In order to minimize the noise introduced by the increased light sensitivity I set the ISO value to 100 for all of the photographs. Pictures were taken indoors, in a constant lighting of approximately 4 000 lx illuminance within the whole sample surface.

5.2.2 Image processing, 3D model formation

The first step of image processing is the preparation of images for processing. The RAW format images were converted into JPEG, the brightness of pictures was adjusted and processed to remove the effect of diffraction in Canon Digital Photo Professional software version 3.14.47. The steps which I took during that process are listed below:

1. Open images to be processed in Digital Photo Professional 3.14.47
2. Open one of the pictures to be processed by double click, then right click on the picture →from menu which pops up choose Tool palette
3. In RAW brightness adjustment set -0.50
4. In Lens, Digital Les Optimizer click Tune
5. Check the checkbox Settings and change them to the MAX

Rest of the options was left in the default settings.

Images of one surface (from all camera configurations) in JPEG file format were loaded into VisualSFM0.5.26 software. The working principle of VisualSFM surface is the technique called structure from motion which is described roughly in chapter 3.3.1. Generally, the software locates the features from 2D pictures and uses them to create a 3D reconstruction of the object on pictures. Structure from motion utilizes the SiftGPU algorithm to match pictures taken from different angles with each other and find all of the matching features. Then, the bundle adjustment process combines the matching features into a sparse 3D reconstruction. After that the sparse reconstruction is upgraded into a dense reconstruction by PMVS/CMVS routine. In a nutshell this routine combines 2 functions – CMVS (Clustering Views for Multi-view Stereo) function, which creates the clusters of a model and PMVS (Patch-based Multi-view Stereo) function, which combines created clusters into a dense reconstruction. The dense point clouds are saved as .PLY (polygon) format file.

After creation of the dense point clouds, the redundant parts (surroundings, floor, lamps, etc.) of the point clouds were removed, so only the joint surface remains. For further processing purposes cropped point cloud needs to be triangulated. Orientation and scaling of the surface is not necessary since the MATLAB algorithm applies the coordinate system for the surface and the size is scaled by the length.

1. Open the ply file to be edited in Cloud Compare 2.6.0
2. To triangulate go to Edit → Mesh → Delaunay 2D (best fitting plane)
3. Save as .STL (Standard Tessellation Language) in ASCII.

5.2.3 3D directional roughness analysis

Both, directional and slope length methods of roughness assessment were used previously in KARMO on different samples. The roughness assessment using both methods were executed using MATLAB. The MATLAB codes for directional roughness assessment are provided by the inventors of the method, Tatone and Grasselli (2009). The MATLAB code for slope length assesment (Tse and Cruden, 1979) were created by Joni Sirkiä, the methodology for roughness assesment using the technique developed by Sirkiä is described in (Iakovlev et al, 2015; Sirkia et al, 2016)STL surfaces can serve as an input data for MATLAB. MATLAB was used to conduct the directional roughness analysis introduced by Tatone and Grasselli (2012). I used the MATLAB GUI and scripts for Rock Surface Roughness Estimator by Geogroup Software to produce colormaps type Virdis of the surfaces, polar plots of the roughness values and polar plots of the errors in the roughness estimation. The detailed description of this roughness estimation method can be found in Tatone, Grasselli (2012). The software (including MATLAB codes) can be found on: http://geogroup.utoronto.ca/. The software was used with default settings, just the colormap type was changed and the material property was change to dull to eliminate the reflection on the colormap.

5.2.4 2D roughness analysis

Similarly to the directional roughness assessment using Rock Surface Roughness Estimator by Geogroup Software, in slope length and surface length roughness assessment the input data is the surface models in .stl format. The algorithm sets up a reference coordinate system by means of orthogonal base vectors created by SVD (Singular Value Decomposition) routine. In the next step algorithm creates a sectioning plane which is defined by a dot product of the base vector in the shearing direction and the plane normal. After establishing a sectioning plane the 2D roughness profile in the shearing direction is created by calculating the intersections of the sectioning plane and surface triangles. In total, 3 2D roughness profiles are created from one surface by dividing it evenly Final roughness characterization is conducted by means of digital JRC calculation using the slope length method (Tse and Cruden, 1979). During this calculation, a sectioning plane is normalized by 0.5 mm sampling interval. The normalization is conducted by taking the mean value for height in a sampling interval, since that sampling pattern showed the best match during studies conducted by Sirkiä (2015). The principle of slope length and surface measurement method is described in chapters 3.3.1 and 3.3.2. The deliverables from this step of photogrammetric prediction are the values of JRC for each of the created profiles.

5.2.5 Estimation of shear strength and residual friction angle

The values of joint roughness coefficient obtained from the analysis described above were used to calculate the peak shear strength and peak friction angle values for the created surfaces. The calculations were done using Barton – Bandis criterion (Barton and Choubey, 1977). The value of uniaxial compressive strength used in calculation is 218 MPa which is a typical strength for the Grey Kuru Granite and was determined according to the standard EN 1926 in STONE POLE LABORATORIO by Suomen Kiviteollisuus Oy. The basic friction angle used for prediction was 33 º and was determined by the author of this thesis with a tilt tests. In total 20 repetitions of a tilt test were done on a smooth sawn surfaces of the same material. One reading was eliminated as an outlier. 33º was the lowest value obtained from the test and occurred 4 times as a result of the tilt test.

5.3 Aalto Shear Pull Experiment for Rock Tensile fracture ASPERT

5.3.1 Experiment set-up

Aalto Shear Pull Experiment for Rock Tensile fracture (ASPERT) was conducted at the Laboratory of the department of Civil and Environmental Engineering, the time of conducting the experiment was 20-28.6.2016. The test arrangement was entirely build up by the Laboratory staff.

Pulling force was applied on the upper part of the sample using the hydraulic cylinder (1) (Figures 33 and 34) The force was transferred through 2.5 m long chains attached with one end to the head of the cylinder (2) and with two ends to the steel frame installed on the sample (2a and 2b). Steel frame was installed on the upper part of the sample only, and was consisting of two steel beams (profile UNP 100) attached to the sides of the sample (3a and 3b) (Figures 33 and 34) and two steel rods installed on the front and back of the sample squeezing the beams together (4a and 4b) (Figures 33 and 34). Pulling chains were attached to the rod placed on the front of the sample (4a). The purpose of the steel frame was to ensure even distribution of the shear stress within the sample and enable handling of the sample – lifting and flipping it over. The still beams were attached to the rock with expansion anchors (5), spacing between the anchors was equal to 15 cm and the pattern is presented in figure 66 in the Appendix 3.
Underneath the long steel beam, shorter pieces of the steel beams (profile UNP 100) were installed, two on each side (6a, 6b, 6c and 6d) (Figure 36). Those beams were installed on the joint, in place were two sides of the sample were meeting, and were fixed to upper long steel beams with a still clamps (7) (Figure 36)to prevent the lateral displacement of the upper sample. The ball-bearing plates (8a, 8b, 8c and 8d) (Figure 37) were placed between the sample surface and the steel beams (6a, b, c, and d) (Figure 36) to minimize the friction. To prevent the both sides of the sample from moving forward together the 2.5 m long steel beam (9) (Figure 35) was fixed to the floor. The beam was attached to the floor with two perpendicular, securing beams (10a and 10b) (Figure 35) screwed to the floor and additionally attached to the across beam (9) (Figure 35) with a steel clamps. During the test sample was placed on a wooden platform (11) (Figure 36). Assembly pictures of the setup are presented in Appendix 3.

During the experiment displacement of the upper part of the sample was measured in all three directions: vertical, longitudinal and lateral. For that reason, 10 linear variable differential transformers (LVDT) were installed on the sample (Figure S1). Shear (longitudinal) displacement of the upper sample was measured with four LVDTs (S_1, S_2, S_3, and S_4) (Figure 37 and 38). Those LVDTs were installed at the back of the sample. Transformers number 1 and 3 were used to control the shearing rate due to their high accuracy, range of those devices was ± 1 mm and. Transformers S_2 and S_4 were used to measure the shear displacement due to their broader range which was ± 100 mm. Vertical displacement (dilation) was measured with four LVDTs installed on the top of the sample (S_5, S_6, S_7 and S_8) (Figure 37 and 38) their range was ± 10 mm. Lateral (sideways) displacement was measured with two LVDTs installed on the side of the sample. Sideways movement of the sample was constrained but two measurement devices (S_9 and S_10) of range ± 5 mm were installed anyway to control if movements occurs despite of the barrier used. All of the installed LVDTs were accurate to five decimals. Sideways LVDTs were installed on the steel frame since it was not possible to install them on the sample surface directly.

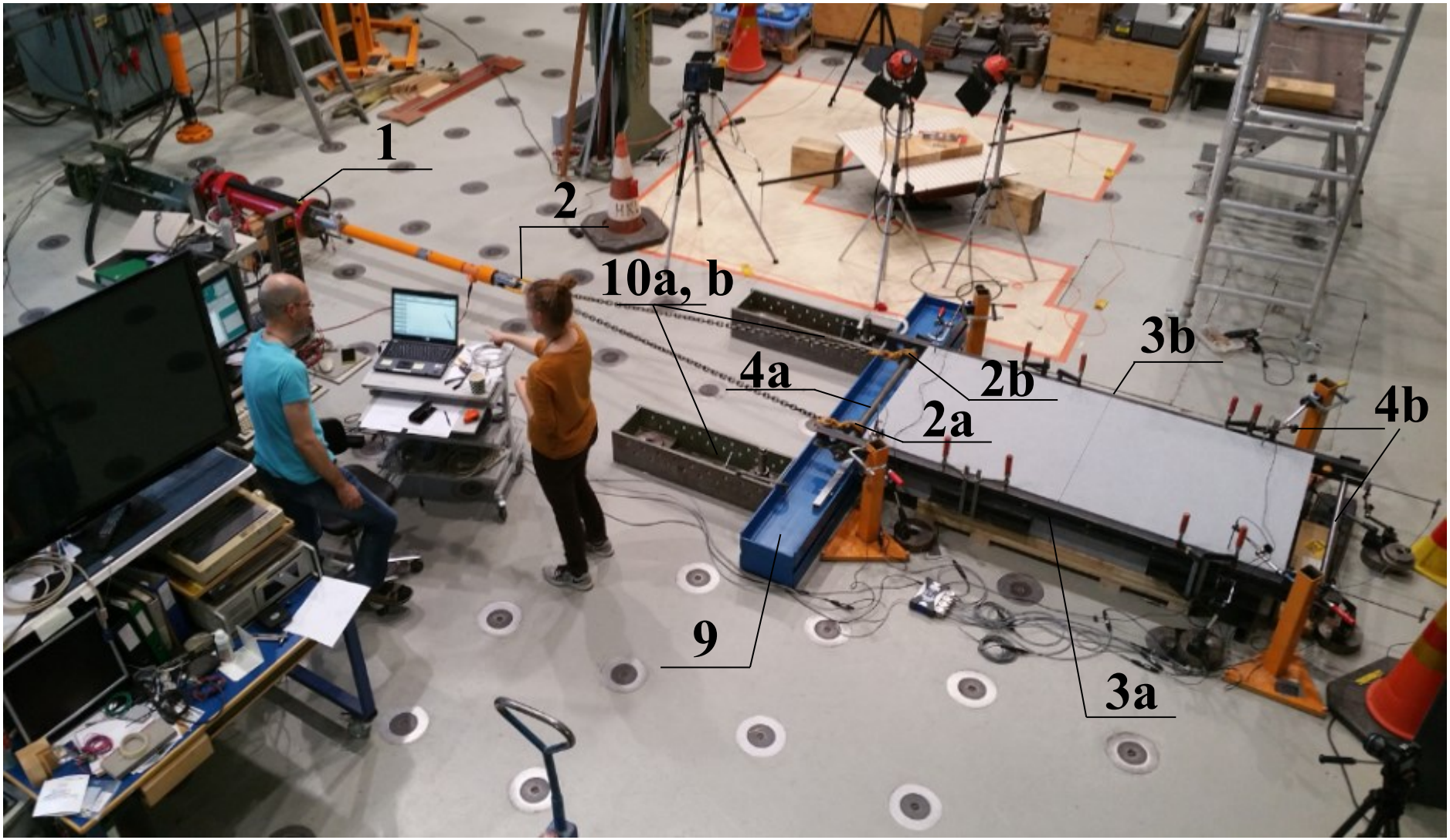

Figure 33 Overview of the whole set-up during the first stage of shearing

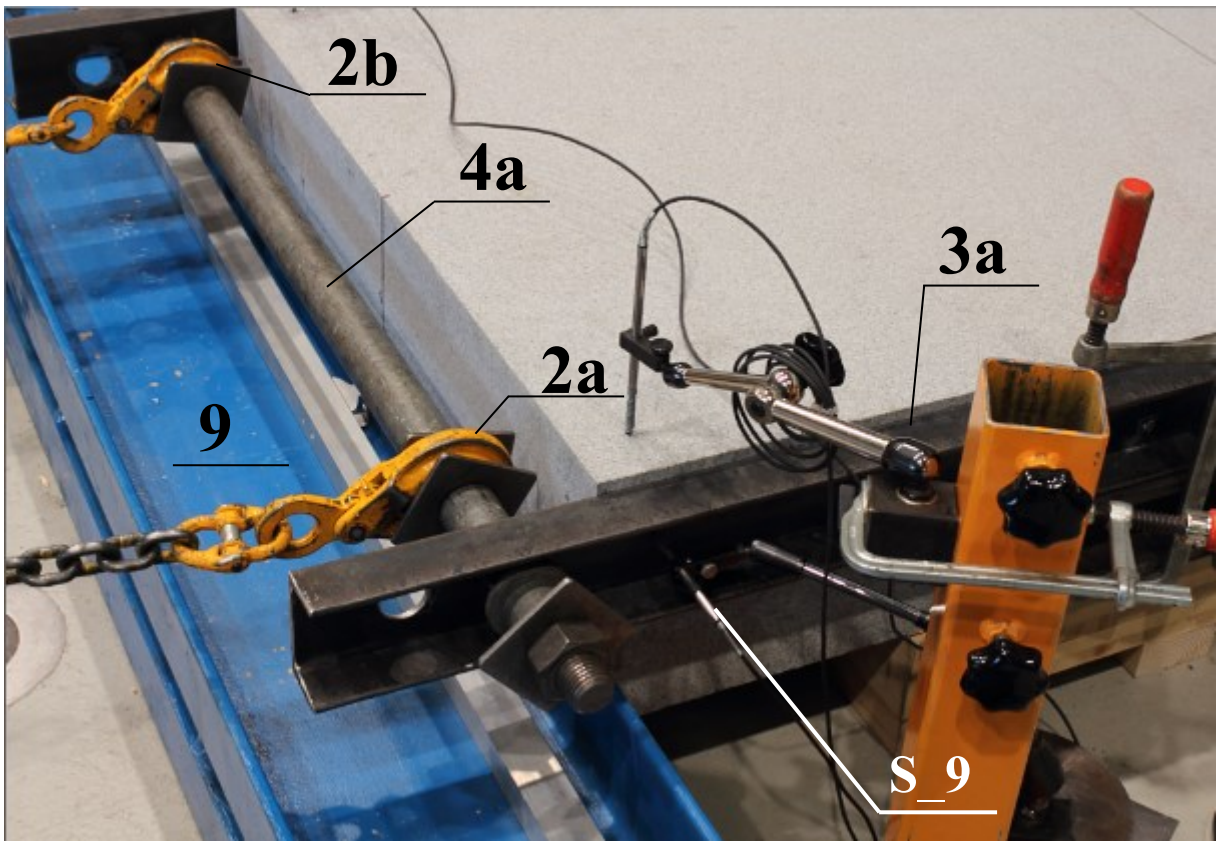

Figure 34 Detail of the steel frame and chain attaching clamps.

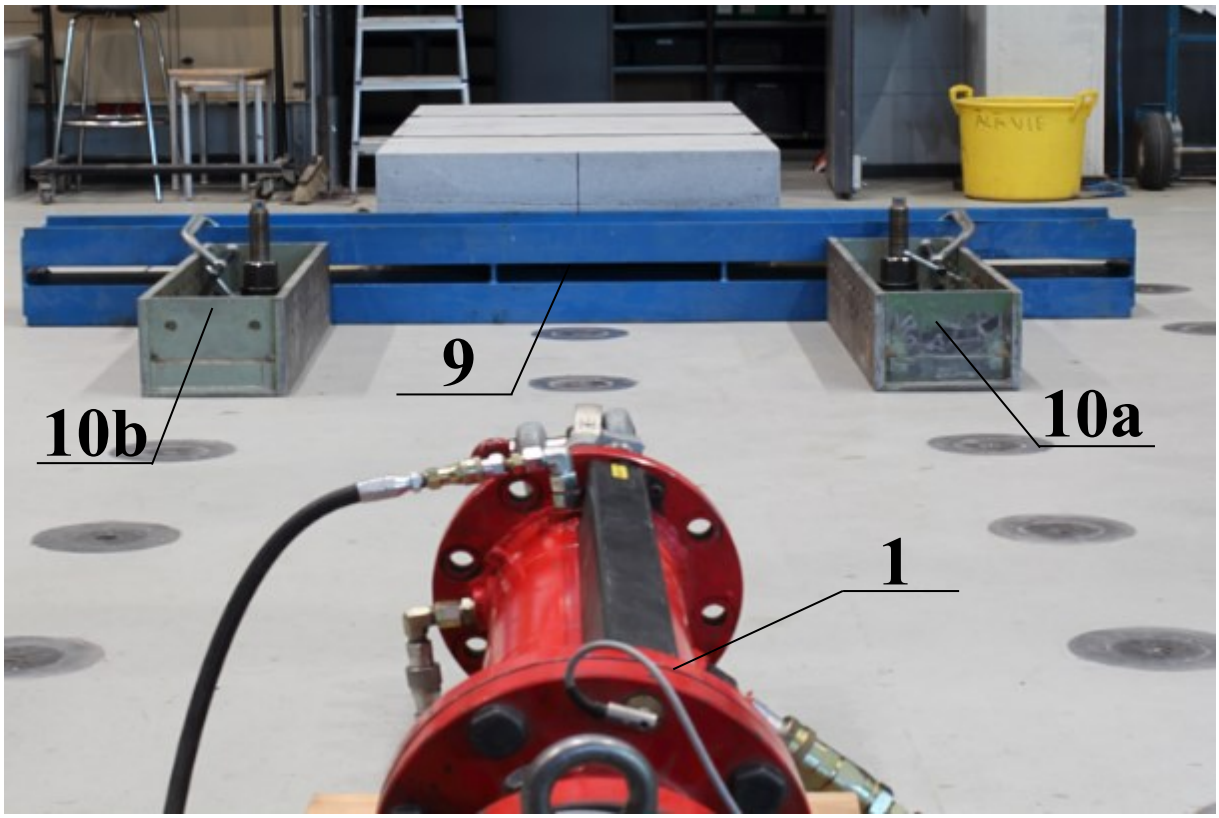

Figure 35 Hydraulic cylinder and barrier preventing the bottom sample from moving together with the upper sample

Figure 36. Steel frame and elements preventing lateral displacement of the upper sample.

Figure 37 Back view of the test arrangement before the second shearing stage

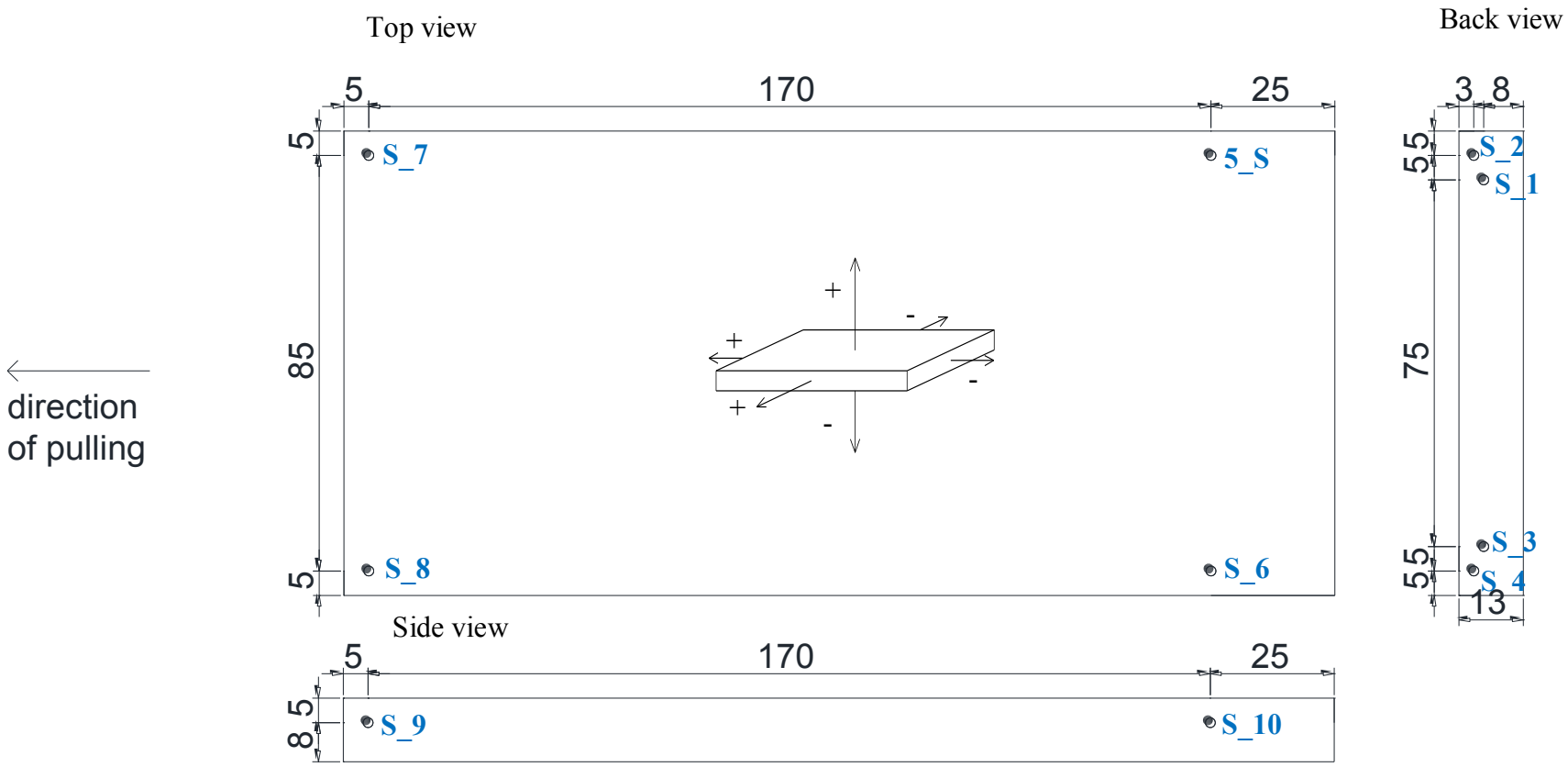
Top view
Back view
Side view
direction
of pulling
5
170
25
3
8
85
75
55
55
13
5
5
8
5
S_7
5_S
S_8
S_6
S_2
S_1
S_3
S_4
S_9
S_10
+
-
+
-
+
-

5.3.2 Procedure

Since there is no suggested method for determining the shear strength using pull test specifically (ISRM, 2007; ISRM, 2014) the test procedure was adopted from the ISRM Suggested Method for Laboratory Determination of the Shear Strength of Rock Joints: Revised Version (ISRM, 2014).
According to the norm, test apparatus was consist of:

a) A stiff testing system, including a stiff frame (3a, 3b, 4a, 4b) and a stiff sample holder which was sufficiently rigid to prevent distortion during the test (9, 10a, 10b).
b) A specimen holder, where both halves of specimen are fastened, which also allows relative shear and normal displacement (3a, 3b, 6a, 6b, 6c, 6d, 9, 10a, and 10b).
c) Loading devices to apply the normal and shear loads on the specimen at adequate rates in such way that the shear load goes through the centroid of the sheared area (1, 2, 2a, 2b, and 4a).
d) Devices to measure normal and shear displacement throughout the test (LVDTs No. 1-10)

As it has been mentioned in the chapter 5.1, Figure 28, the test procedure incorporated 4 shearing stages. Stages were varying according to the normal load sample was subjected to. First was done under the normal load being just the weight of the sample, which is 4 kPa. During the second shearing normal load was increased by 2.6 kPa. During third stage of shearing external normal load was further increased by another 2.6 kPa. Last, fourth stage of shearing was done without any external normal load, just the self-weight of the sample, which is 4 kPa. After each shearing stage the position of the sample was reset to its initial position, aluminum rods were attached to the sample for guidance, to ensure that the sample was put back in the correct position. Repositioning was done using the crane, steel frame rods (4a and 4b) were used to attach the sample to the crane chains.

The rock dust residue left on the sample surface after the sawing was carefully removed with a soft brush and vacuum cleaner. Sample surface was also cleaned in between the test stages, the debris was collected and the rock dust was removed with a soft brush and vacuum cleaner.

The normal load was applied by putting the additional mass on the top of the sample. Since the equal distribution of the load within the shearing area is necessary, that was the most practical way to apply the load on the sample of significant (1,9 m^2) area. Used material was gravel contained in the bags. Bags were weighted separately and secured additionally with plastic bags in case of spillage. Bags were put on the top of the sample in a way that they did not disturb the LVDTs. Small empty spaces were left in the corners of the sample where the displacement measurement devices were installed.

Mass of the upper sample together with the steel frame as well as all additional elements attached to the upper part of the sample (steel clamps, steel beams 6a, b, c, and d) was also established prior to the testing.
Table 3 shows all the mass and pressure put on the sample during respective stages of the test.

Table 3. Normal load during the pull experiment

Test stage	Total mass (including the sample)	Total normal load [kPa]
First	**776,5 kg** 742 kg (upper sample + steel frame – 3a, 3b, 4a, 4b) + 34,5 kg (6a, b, c and d plus steel clamps)	4.0
Second	**1 280 kg** 776,5 kg (sample + additional equipment) + 503,5 kg (bags with gravel)	6.6
Third	**1 778,1 kg** 776,5 kg (sample + additional equipment) + 1 001,6 kg (bags with gravel)	9.2
Fourth	**776,5 kg** 742 kg (upper sample + steel frame – 3a, 3b, 4a, 4b) + 34,5 kg (6a, b, c and d plus steel clamps)	4.0

According to the above mentioned norm (ISRM, 2014), the shearing rate during the tests was set to 0,1 mm/min before peak shear strength was reached and 0,5 mm/min after the peak shear strength was reached. Although, those are the rates of the hydraulic cylinder movement and not the shear displacement of the sample itself. Due to the ability of the chain to store energy the rate of sample shear displacement before peak was significantly lower (see chapter 7.1) during 4 test stages, while the rate of sample shear displacement after peak was slightly higher in all of the test stages due to the stick – slip phenomenon which was observed during all the test stages. That phenomenon and its effect on the test results are explained in 8.2. For all the test stages total shear displacement was equal to 50 mm, which is 2,5% of the length of the sample. The suggested method is to conduct the test until shear displacement reaches at least 5% of the length of the sample, yet, that would extend the testing time to more than 7 hours and it was expected that the residual strength would be reached before that time. Therefore we made a decision that the total shear displacement will be defined during the tests, based on the shape of the stress strain curve. 4 checking points were set up for the total shear displacement – 50 mm, 75 mm, 100 mm and 200 mm. The plan was to judge on the ongoing basis at the each checkpoint if the shear force values are stabilized (no trend can be detected) and stop the test if at the first checkpoint where the values reached a plateau. The stress strain curve was observed while the tests were carried out and the decision was made to stop the test at 50 mm displacement, since the value of the shear strength was stabilized at that point. The sampling frequency used for all the test stages was 10 Hz.

5.3.3 Risk analysis

Before the test, risk analysis was done to identify the possible risk sources for the experiment and to plan and implement mitigation strategies preventing those risks. Five risks were identified, the likelihood of those risks to occur and the consequences of them occurring were assessed and are presented in the table 4 below. For each risk the mitigation strategy was planned and implemented in the test arrangement and procedure.

Table 4. Risk analysis

Risk	Likelihood	Consequences	Mitigation strategy	Risk rate
Malfunction of more than one LVDTs measuring the dilation	Rare	Moderate –dilation values not recorded, test results still valid	Usage of 4 LVDTs (minimal amount required by norm (ISRM, 2014) is one	LOW
Malfunction of LVDTs measuring the shear displacement	Rare	Severe – shearing rate is not recorded and not controlled, test results are invalid	Usage of 4 LVDTs (minimal amount required by norm (ISRM, 2014) is one	MEDIUM
Too big lateral displacement	Possible	Major - Too big lateral displacement affects the shearing rate, test results are invalid	Installing a barrier to prevent the sideways displacement displacement	MEDIUM
Uncontrolled shear displacement (beyond the allowed range)	Unlikely	Major – Results not consistent with ISRM standard, results are invalid		MEDIUM
Dilation values bigger than the range of LVDTs (+- 10mm)	Unlikely	Moderate – dilation values not recorded, test has to be interrupted but results are still valid	Measuring the asperities height prior to the test (within the range of maximum planned displacement (20 cm)	LOW

The risk analysis done prior to the experiment did not identify any major risks and thanks to the risk mitigation strategies used the total risk was assessed as low.
Despite that, some unexpected events have occurred during the test due to the human error. One minor incident was a disturbance of one of the vertical displacement LVDTs. Because there were vertical displacement LVDTs installed on the sample, malfunction of one of them has minor consequences since the sample surface is planar and the position of the 4th LVDT can be calculated if the data from remaining 3 is available.
We also observed that the LVDTs can be affected by the cell phones.
Another incident happened during the preparation for the second stage of shearing.

Before the start of the test the hydraulic cylinder was turned on in order to tense the chains, unfortunately, due to the mistaken set up of the cylinder and malfunction of the emergency stop button the displacement exceeded planned range and the sample was pulled uncontrolled. During that accidental loading two damage zones were created on the sample surface. The data from this incident was recorded and is presented in the chapter 7.1.2. Figures 39 and 40 below show disturbances in measurements of dilation and shear displacement.

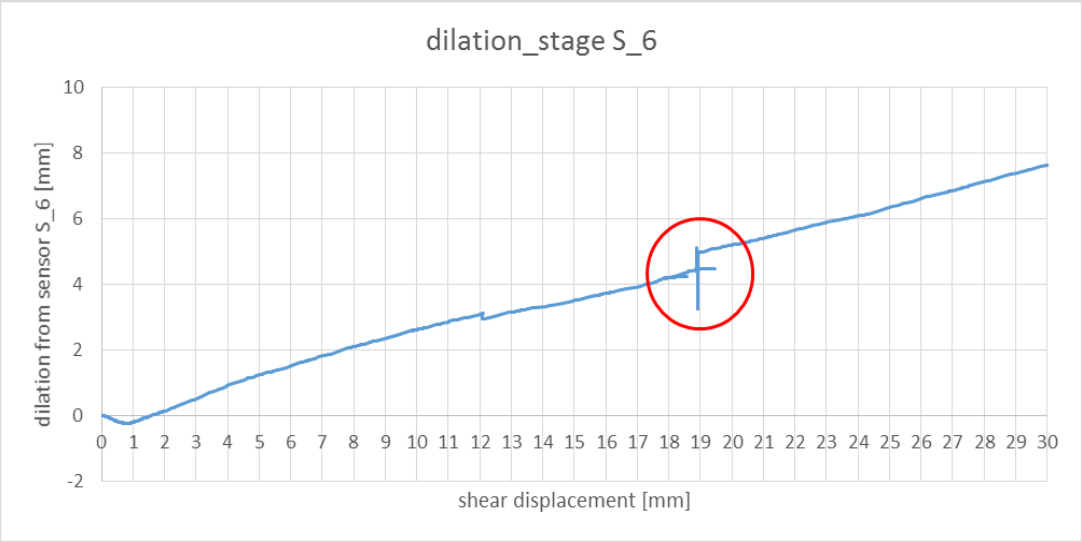

Figure 39 The disturbance of the sensor caused the shift in value of dilation.

Before calculating the average of readings from all sensors for the first stage of shearing this error was corrected by removing the points responsible for the shift in the readings.

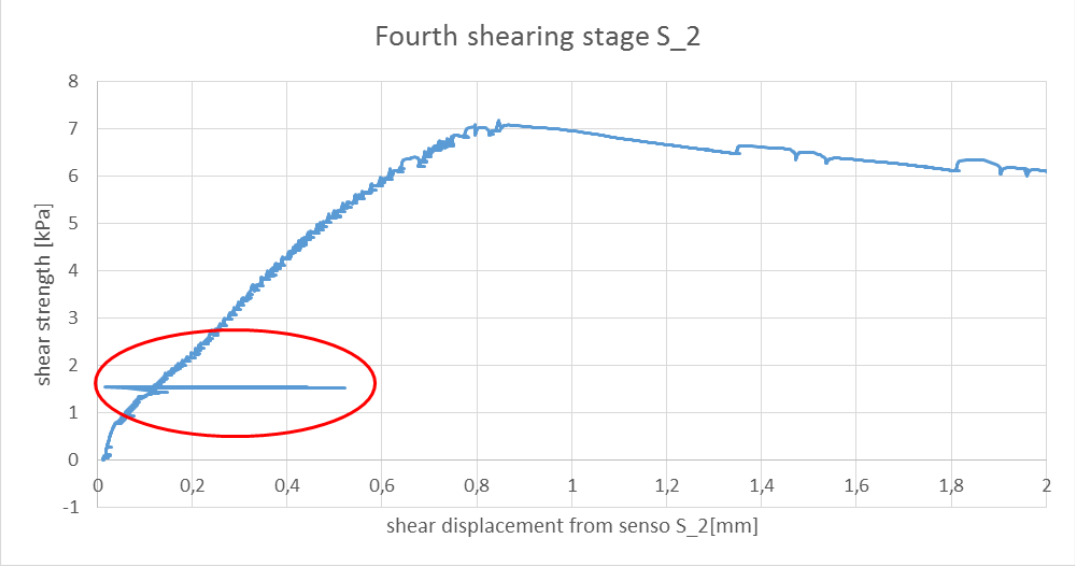

Figure 40 Artifact in the recording of shear displacement

The graph above presents a false reading of the shear displacement recorded by LVDT number 6, we noticed that this artifact was recorded at the time when person with cell phone was standing next to the sensor, and therefore our conclusion is that the cell phone has interfered with LVDT.

6 Photogrammetric prediction of joint´s roughness and friction angle

6.1 Presentation of the results

6.1.1 Digital models of sample surface

Since I did photogrammetry after and before the pull test, in total 4 models of the joint surface were created. That is: top and bottom surface before the test and top and bottom surface after the test. Table 5 below shows the absolute number of points in the point cloud for each of the surfaces, the number of points per cm^2 of the surface and the total number of triangles created.

Table 5. Digital models of the sample surface.

Surface model [-]	Number of points created in dense reconstruction [-]	Average spacing between the data points [mm]	Number of points created in sparse reconstruction [-]	Number of projections in sparse reconstruction [-]	Density of a dense point cloud [$1/cm^2$]	Number of triangles created
Before test, top	3 267 383	0.76	169 512 (3+: 145 139)	3 095 182 (3+: 3 047 077)	172	6 532 519
Before test, bottom	1 655 666	1.07	146 731 (3+: 116 166)	2 724 968 (3+: 2 675 952)	87	3 310 644
After test, top	2 658 544	0.85	158 977 (3+: 126 523)	2 818 340 (3+: 2 759 015)	140	5 315 650
After test, bottom	3 406 850	0.75	129 589 (3+: 102 035)	2 528 665 (3+: 2 477 670)	179	6 812 817

Figure 41 below presents the picture of triangulated, oriented and scaled surface model of top surface after the test opened in VisualSFM 0.5.26.

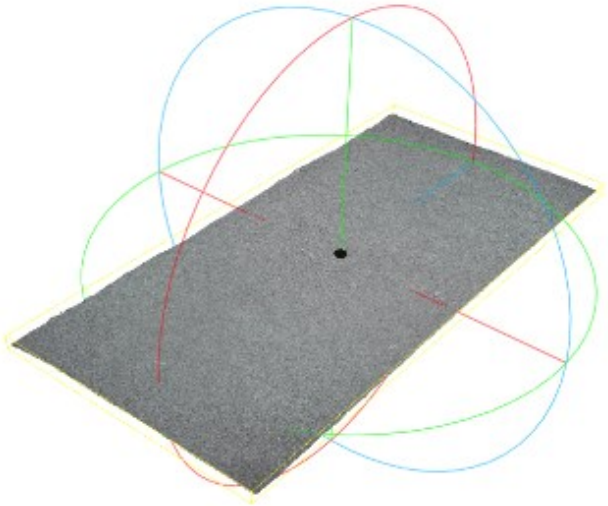

Figure 41 Oriented and triangulated surface model.

6.1.2 3D directional roughness analysis

For each surface model the directional roughness according to Tatone and Grasselli (2009) was analyzed. The results of analysis include also the value of El – Soudani roughness coefficient (Rs) (El – Soudani, 1987) for each analyzed surface. The R_s coefficient, according to El-Soudani (1987) can range between the values of 0 and 5, where the higher value indicates the rougher surface. The roughness assessment was conducted with MATLAB GUI Rock Surface Roughness Estimator by Geogroup (see chapter 4.2).

Table 6.3D directional roughness assessment.

surface model	Directional roughness **(θ_{max}/C+1)** in the direction of shearing - **X**	El-Soudani Roghness coefficient **(Rs)**	Number of triangles in the surface model
before bottom	21.48129	1.26663	3 310 644
after bottom	23.30533	1.29336	6 812 817
before top	27.63781	1.38969	6 532 519
after top	19.88789	1.22151	5 315 65

The table 6 above shows the results of directional **(θ/C+1)** analysis in the direction of shearing (along the X axis of a model) compared with El –Soudani Roughness coefficient (Rs) for respective surfaces. Model of the top surface before test is characterized with the highest directional roughness, while model of the top surface after the test is characterized with the lowest value of directional roughness. That results are consistent with the values of Rs coefficient.

The directional residual friction angle was calculated using the equation 16 presented in chapter.3.3.3, yet, this equation was developed for the cases of CNS therefore table presents the values of residual friction angle which we would have gotten if we submitted the sample to the shearing in constant normal stiffness conditions.

Only the direction of shearing (azimuth 0, direction of x axis of a model) was considered in calculations.

Table below contains the parameters used for calculations and parameters used in calculations. Value of basic friction angle for used rock is 33º and was determined with a tilt test. Sample block of the same rock and dimensions: 50 x 25 cm and smooth sawn side surfaces was tested 20 times on a tilt table. The tilting rate used during the test was around 15º/min. From 20 results one was excluded due to its exceptionally low value and the value of 33º was chosen as it was the lowest and repeated 4 times among the results.

Table 7. Residual friction angle predicted from 3D roughness analysis.

surface model	A_0	C	θ_{max}	φ'_r
before bottom	0,47839	3,19	90,01	52,61
after bottom	0,48499	2,86	89,96	52,43
before top	0,48351	2,26	90,10	51,82
after top	0,48385	3,53	90,09	52,90

The polar plots for conducted directional analysis for all surfaces are presented in the figure 64 in Appendix 1. Colormaps of created surfaces are presented in figure 65 in Appendix 2.

6.1.3 2D roughness analysis and peak friction angle estimation

The 2D roughness analysis was conducted by following the procedure described in (Iakovlev et al, 2015; Sirkiä et al, 2016). The roughness analysis was conducted on the cross sectional profiles of the digital models of joint surface. From each model, three cross sections were extracted along the direction of shearing dividing the surface in three equal parts. Methods used for the roughness assessment are surface length and slope measurement described shortly in chapters 3.3.1 an 3.3.2. Sampling window used for analysis was 0.5 mm. The normalization chosen for analysis was a normalization to the mean height, since this type performed the best in studies conducted by Sirkiä (2015). Table below presents the values of JRC of each section of the surface models calculated with surface length and slope measurement methods.

Table 8. JRC values from slope measurement and surface length methods.

Surface model	before bottom			after bottom			before top			after top		
section	1	2	3	1	2	3	1	2	3	1	2	3
Surface length	27.3	35.2	36.6	26.2	40.6	26.8	33.2	44.2	47.4	23.4	25.2	27.9
Slope measurement	19.9	21.5	21.8	18.7	21.9	19.2	20.8	23.9	23.3	17.8	18.4	19.1
Slope measurement average	21.1			19.9			22.6			18,4		

The value of peak friction angle was derived from Barton – Bandis criterion, using the following equations:

$$\tau = \sigma_n \tan\left(\varphi_b + JRC log_{10}\left(\frac{JCS}{\sigma_n}\right)\right); (18)$$

$$\frac{\tau}{\sigma_n} = \tan\left(\varphi_b + JRC log_{10}\left(\frac{JCS}{\sigma_n}\right)\right); (19)$$

It is known that:

$$\arctan\left(\frac{\tau}{\sigma_n}\right) = (\varphi_b + i); (20)$$

So:

$$(\varphi_b + i) = \arctan(\tan\left(\varphi_b + JRC log_{10}\left(\frac{JCS}{\sigma_n}\right)\right) = \varphi_b + JRC log_{10}\left(\frac{JCS}{\sigma_n}\right); (21)$$

The vales used in calculations are:
φ_b- 33°
JRC- according to the Table 8
JCS – 216 MPa (SONE POLO LABORATORIO, test on Grey Kuru Granite according to the standard EN 12371)
σ_n – 0.004 MPa

Peak friction angle calculated according to the formula 21 look as follow:

Table 9. Peak friction angles estimated with Barton_Bandis criterion.

Surface model	before bottom			after bottom			before top			after top		
section	1	2	3	1	2	3	1	2	3	1	2	3
Surface length	162,3	199,7	206,4	157,1	225,3	159,9	190,2	242,3	257,5	143,8	152,4	165,1
Slope measurement	127,3	134,8	136,3	121,6	136,7	123,9	131,5	146,2	143,4	117,3	120,1	123,5

6.2 Interpretation of the results

6.2.1 Digital models of joint surfaces

The density of the point clouds of joint surfaces differ quite significantly despite using the same methodology for each of the surface models, both during photogrammetry and image processing during creation of the models. The least dense surface model is a model of bottom surface before the test, here the point cloud density was 87 [points/cm^2]. In the densest model – bottom surface after test, the point cloud density is over two times bigger and is equal to 179 [points/cm^2]. There was no difference in the image acquisition technique and image processing. Visually, the quality of photographs of each surface is the same. I took and processed the same amount of pictures of each surface, the lighting conditions did not change during the process of taking pictures and the configurations of the camera position were the same for all of the surfaces photographed. Then pictures were processed using the same methodology described in chapter 4.2.Most probably, the difference lies in the dense reconstruction process of VisualSFM 0.5.26, after checking the log files for differences it turned out that for the point cloud of bottom surface before test only 3 clusters were created, while for other surfaces the amount of created clusters was 6. The results did not change after updating the software to the most current version and changing the settings to use 0 level for PMVS function (use full resolution pictures for processing). During the sparse reconstruction, the amount of points created for each surface model is approximately the same. The number of points created during the sparse reconstruction is shown in Table 5. No correlation exist between the number of points in sparse and dense reconstruction.

6.2.2 3D directional roughness assesment

Obviously the density of the point cloud affects the results of the directional roughness estimation. That can be observed from the Figure 65 in Appendix 1 where the polar plots for the roughness estimation are presented. Figure X a) shows the Roughness of the bottom surface before the test, while b) shows the roughness of the same surface after test. For both surfaces the polar plots are circular, meaning that the roughness is an anisotropic value. Yet the absolute value of the roughness estimates is much lover for the surface before test than for the same surface after test. That is obviously wrong, since the shearing cannot make the sample rougher, the difference here comes from the model of the bottom surface before test being much less accurate that the bottom surface after the test. Number of triangles for the surface before test is less than half of the number of triangles for the same surface after test. Since much less triangles were used in the model from before test to cover the same surface are, the average area of triangles themselves must have been much bigger, leading to the estimated surface before test being much smoother than the same surface after test. Therefore it can be concluded that the roughness of the bottom surface before test presented on the Figure 65 is an underestimation. Opposite situation can be observed for the top surface before and after test. Here, the surface after the test is consist of the lower number of triangles than the same surface after test, so probably the roughness for this surface is underestimated.

In sum, since the photogrammetry produced the surfaces of significantly different accuracy, the results of roughness estimation for those surfaces should not be compared with each other and no conclusion about the roughness of the surfaces can be drawn from the table 6.

6.2.3 2D roughness assessment and peak friction angle estimation

In photogrammetric prediction value of joint roughness coefficient was estimated using slope measurement and surface length methods. Values of JRC obtained with those methods were then used to calculate the friction angle of the discontinuity with Barton – Bandis criterion (equation 18).

Table 8 presenting the values of JRC for each of the profiles in respective surfaces shows the difference in JRC values estimated with surface length and slope measurements methods. Both methods give overestimated results, but the JRCs calculated with surface length method are much higher than those calculated with slope measurement method. Average value of JRC calculated with slope measurement method for all profiles is 21.5, while the same value from surface length method is 32.8. It might seem unexpected that the values of JRC were overestimated, since as it has been mentioned before, the digital model of joint surfaces are of rather low density. That can be explained by the noise which originates from the size of sampling window being smaller than the spacing between the data points in the point clouds. The sampling window used for the slope measurement and surface length JRC calculations was 0.5 mm while the spacing between the data points was equal to 0.76 mm for top surface before test, 1.07 mm for bottom surface before test, 0.85 mm for top surface after test and 0.75 mm for bottom surface after test. Due to the size of sampling window, some intermediate points might have been interpreted as the asperity tips which at the end led to overestimation of the roughness. Since photogrammetrically predicted JRC values are unreliable some alternative empirical methods were incorporated to obtain the value of joint roughness coefficient for tested sample. The results are presented in the next chapter.

Finally, the friction angle estimations used Barton - Bandis criteria was conducted. The results obtained from calculations give the values of friction angle over 90º degrees, which is unrealistic. Analysis of the results led to conclusion that the incorrect results originate from relatively low value of normal load σ_n. Authors of the criterion (Barton and Choubey, 1977) do not note the lower limit of the criterion applicability for the low value of normal stress. Yet, they point out that the proposed envelope has a curvy-linear form in case of the most rough joints (JRC >20). The linear relation between shear stress and normal stress in this case occurs for very low normal load values. Hoek (2007) observed, that the lower limit of normal load can be determined using the fact pointed out by Barton and Bandis (1977), that the criterion losses its practical meaning when $\varphi_b+JRC*\log(JCS/\sigma_n) > 70º$. Due to that limitation, the peak shear strength of a joint was calculated assuming the linear $\tau - \sigma_n$ relation. Results of those calculations are presented in next chapter.

Photogrammetric prediction of sample roughness and friction angle using Barton-Bandis gave incorrect results. However, those estimations are interesting and valuable since they reveal the limitations of Barton-Bandis criterion for cases of very low normal load. However, overestimated values of JRC did also contribute to the failure of friction angle predictions since the applicability of Barton – Bandis criterion is especially limited for surfaces of high roughness. The limitations of used criterion are discussed and analysed in the next chapter.

6.2.4 Alternative JRC estimation

Since the surface length and slope measurement analysis of digital models created with photogrammetry gave unrealistically high values of JRC, some alternative methods were implemented to find out the actual value of JRC for analyzed sample.

- Graphical JRC estimation using the graph presented by Barton and Choubey (1977).

The results obtained from ASPERT were analyzed using the graph describing a relation between the friction angle and the logarithm of the ratio of joint compressive strength to normal load applied during the test. The relation is presented in the figure 42 below. As can be seen in the figure, JRC values vary from 6 - 8 for the results of first stage shearing and 8 – 10 from the second and third stage. Comparing to the values obtained from surface length and slope measurement analysis of digital models of a joint these values are significantly lower.

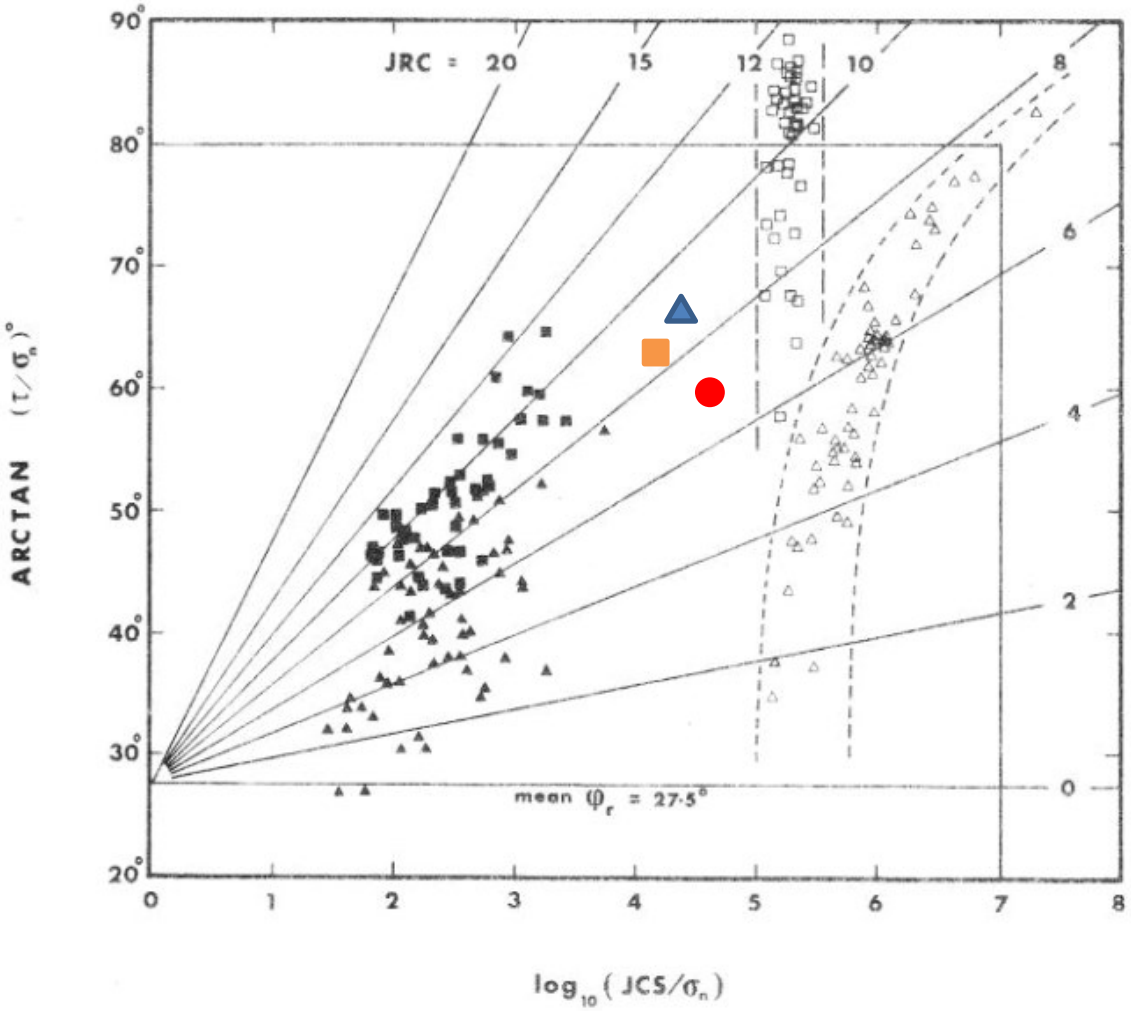

Figure 42 Relation between the friction angle, log (JCS/σn), and JRC values in tests conducted by Barton and Choubey (1977) with added results of ASPERT.

Black triangles represent the results of tilt test, and black squares of push test. The results of ASPERT are presented as red circle for the first and fourth test stages blue triangle for the second stage of test and yellow square for the third stage.

- Hand measurement of JRC.

Prior to the test, the roughness of both surfaces was measured with a Barton´s profilometer. The JRC profiles were measured in the direction of shearing and with the same pattern as the sections for surface length and slope measurement were made – in tree lines dividing the surface evenly. The profilometer used for the analysis was 25 cm long. Consequently, from each surface 24 profiles were taken – 8 for each sectioning line. To each profile, the JRC value was assigned by visual comparison with the standard profiles (Barton and Choubey, 1977). The results of the analysis are presented in the Figure 43 a and b below. As can be seen in the figures, for both surfaces the most frequent reading was 6 – 8. In case of the bottom sample the range of 8-10 is also a big part of the results – 10 out of 24 readings gave a result from this range. In case of the top half of the sample it is just three readings. In sum readings from range 6 – 8 make 54% of all readings for bottom surface and 63% of all readings for top surface.

a). Results of the hand JRC measurements for the bottom half of the sample.

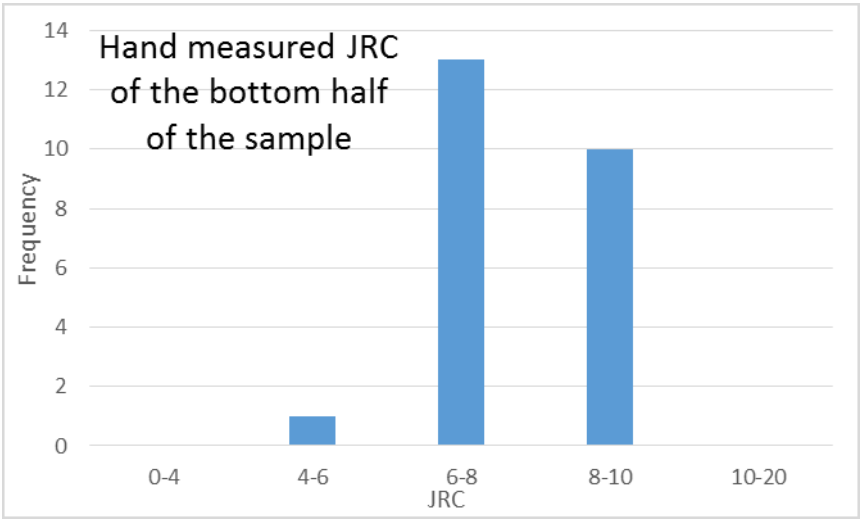

b). Results of the hand JRC measurements for the top half of the sample.

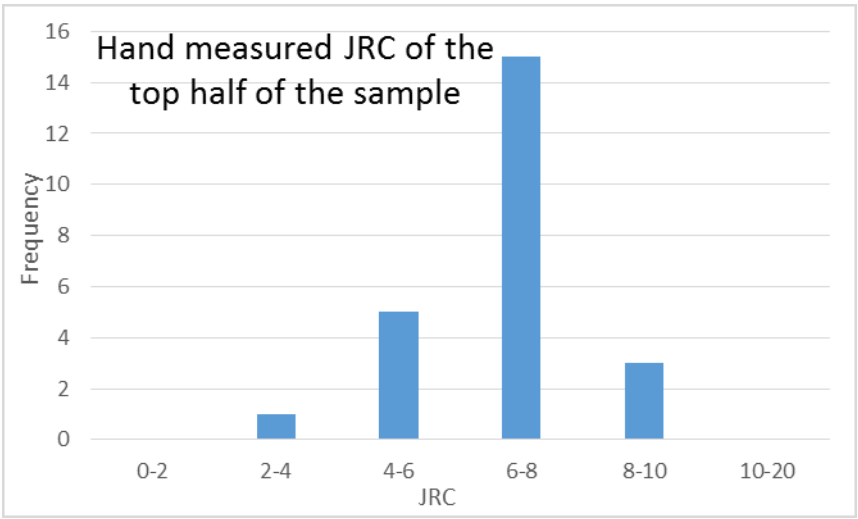

Figure 43 Results of the hand JRC measurements for the bottom and top half of the sample

6.2.5 Limitations of Barton – Bandis criterion

Both results of JRC and peak friction angle seem overestimated. The estimation of JRC values results probably from noise in digital models due to the sampling window being smaller than the point spacing. Incorrect values of peak friction angles probably result from the limitation of Barton – Bandis criterion (equation 18). According to Hoek (2007), the applicability of Barton – Bandis criterion is limited by the value of normal load. Moreover, Barton and Choubey (1977) pointed out that the value of $\arctan(\tau/\sigma_n)$=70º is the maximum allowable shear strength limiting the practical meaning of equation 18. For values higher than this, the relation between shear and normal stress is linear. Therefore, according to the authors, estimations giving values higher than 70º should be ignored, and the value of 70º should be considered as a result. They also highlight that for the roughest joints (of friction angle bigger than 70º) their envelope has a curvy-linear form. That form is presented in figure 44 below. Figure shows the relation between shear and normal stress for different size joints of high roughness. The JRC value for joints is 20. The graph presents the shear – normal stress envelope for 100 mm, 50 mm, 10 mm and 5 mm long joints, the numbers above the lines indicate which function represents which joint length. As can be seen, for the joint length 100 mm, the relation between shear and normal stress is linear for values of normal load smaller than 1 MPa. For higher values of normal lad this relation is nonlinear and can be described with equation 18. In case of smaller samples (50 mm, 10 mm, 5 mm) the normal load value for which the $\tau - \sigma_n$ relation is linear is respectively smaller, since normal stress is higher. Since the application limit for equation 18 is the value of $\arctan(\tau/\sigma_n)$ = 70º, the inclination of the linear part of the curves in figure 43 is 70º.

In this chapter, the value of normal load limiting the applicability of Barton – Bandis criterion is found. The peak shear strength of the joint for normal load values used in ASPERT is predicted using the linear relation. The limitation of Barton – Bandis criterion is analyzed with respect to changes in JRC.

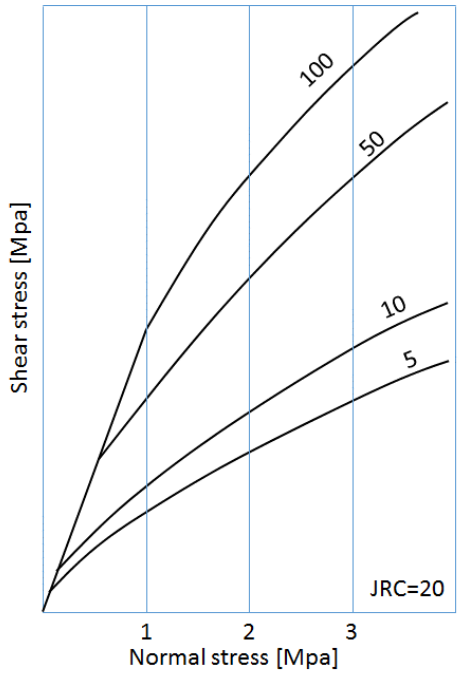

Figure 44 Bilinear form of the Barton – Bandis criterion (modified after Barton and Choubey, 1977)

- LIMITS OF APPLICABILITY OF BARTON – BANDIS CRITERION FOR PHOTOGRAMMETRICALLY ESTIMATED JRC

The normal load limiting the applicability of Barton – Bandis criterion for this studies can be determined by analyzing the value of arctan(τ/σ_n) (see equation 21) for different values of normal load. Such analysis has been conducted using equation 21 and following parameters:

a) Constant JRC = 21.5 value, which is an average of results from slope measurement calculation for surfaces before test and 19.2 for surfaces after test (see table 8)
b) Constant JCS = 218 MPa,
c) Constant φ_b = 33°, obtained from 20 repetitions of tilt test on sawn surfaces of the same material
d) Varying σ_n, range from 0.1 to 5.4 MPa in increments of 0.1. MPa

Results of the analysis are presented in Figure 45 below.
On this figure it can be observed that the friction angle of 70° is reached for value of normal load equal to 4.2 MPa for JRC = 21.5 and 2.6 MPa for JRC = 19.2. Normal loads lower than those produce values higher than 70°. Therefore, the value of normal load limiting the applicability of Barton – Bandis criterion for ASPERT and parameters listed above is 4.2 MPa for JRC estimated for surfaces before test and 2.6 for surfaces after test. It is important to notice that this limit is defined with using overestimated JRC value (see table 8).

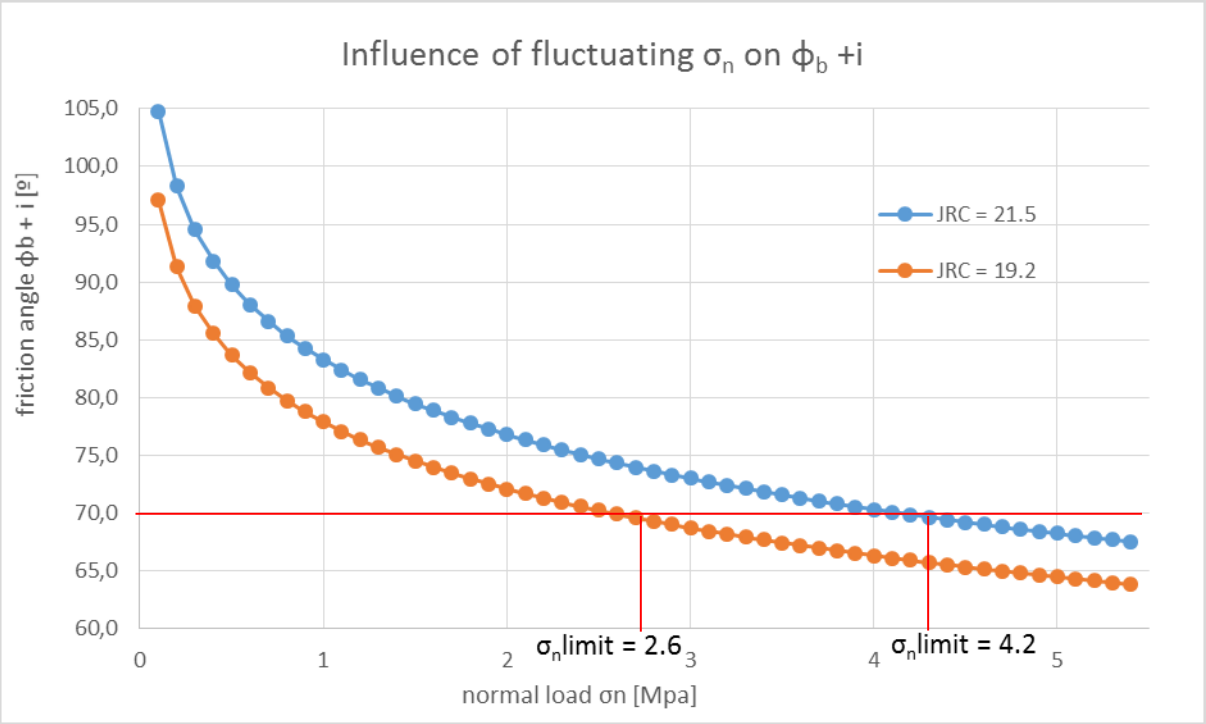

Figure 45 Friction angle as a function of normal load for photogrammetrically predicted JRC.

JRC value = 21.5 (slope measurement estimation for surfaces from before test) and 19.2 (slope measurement estimation for surfaces from before test), normal load limiting applicability of Barton – Bandis criterion is equal to 4.2 MPa.

Since the values of arctan (τ/σ_n) calculated for JRC values presented in table 8 are larger than 70º, the relation between normal and shear strength is assumed to be linear, according to what Barton and Choubey (1977) suggest. The linear relation can be defined by the limiting value of normal load and respective to it value of shear strength. According to analysis shown in figure 46 the linear relation between the normal load and shear stress is limited by the normal load equal to 2.6 MPa and 4.2. MPa. Since both of those values are much higher than the normal loads used during ASPERT, the shear strength of a joint can be can be calculated from the linear relation. According to equation 18 shear stress values respective to the limiting values of normal load are equal to 7.12 MPa and 11.46 MPa respectively. Linearity of the τ-σ_n envelope occurs for values lower than that and can be described with equation:

$$\tau = 2.792 * \sigma_n \; ; (22)$$

Using equation shown above, the peak shear strength of a joint was calculated for the normal loads representing the respective stages of ASPERT. Results of those calculations are shown in table 10 below.

Table 10. Results of photogrammetric prediction

	Stages of ASPERT			
	1st	2nd	3rd	4th
normal stress [kPa]	4.0	6.6	9.2	4.0
peak shear stress [kPa]	10.9	18.0	25.1	10.9

- LIMITS OF APPLICABILITY OF BARTON – BANDIS CRITERION FOR HAND MEASURED AND GRAPHICALLY ESTIMATED JRC

Since the minimum value of normal load limiting the applicability of Barton – Bandis criterion is depended on the value of JRC, the values of joint roughness coefficient estimated with graphical method and hand measurements were analyzed towards this limitation). Figure 46 below shows the relation between friction angle calculated with Barton – Bandis criterion and the normal load for JRC values 6, 8 and 10.

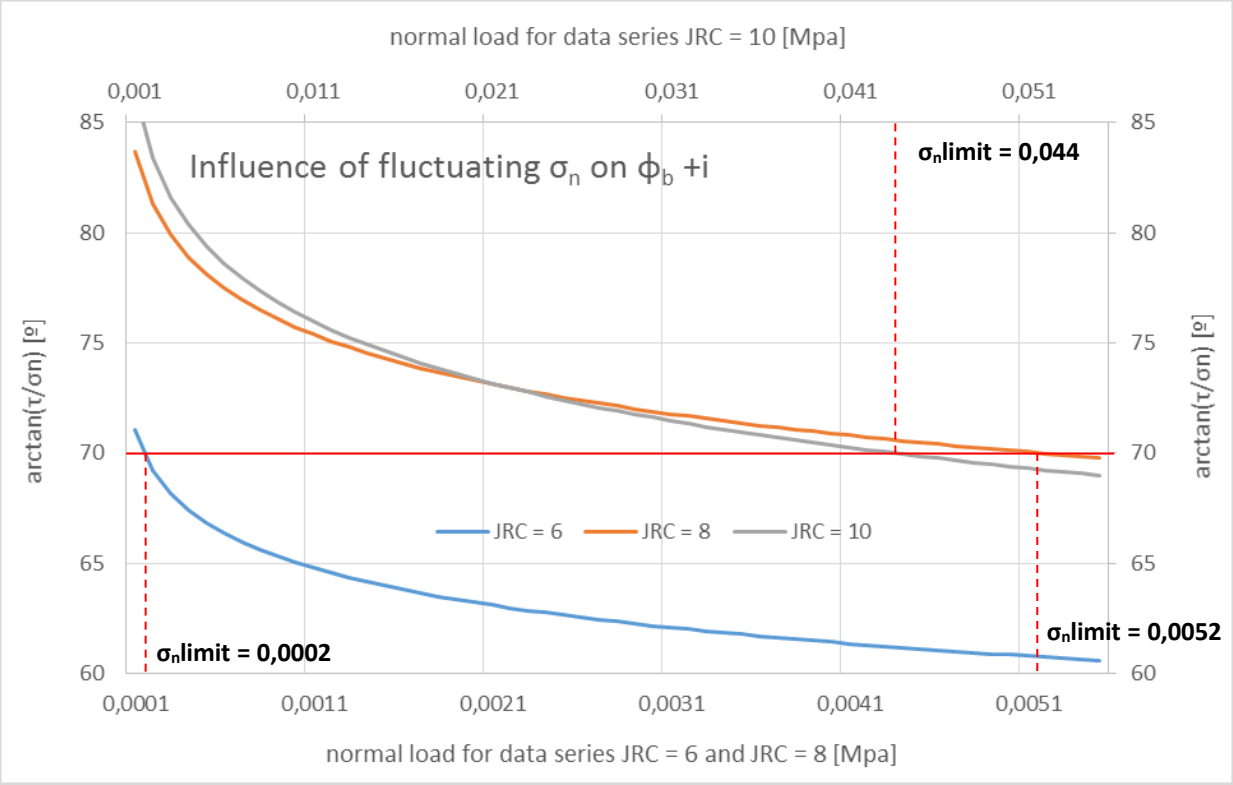

Figure 46 Friction angle as a function of normal load for hand measured and graphically estimated JRC.

The values of normal load used during ASPERT were 0,004 MPa in first and fourth stage shearing, 0,0066 MPa during second and 0,0092 MPa during the third stage. According to figure 47 peak shear strength can be estimated with Barton – Bandis criterion for all the test stages assuming JRC = 6 and for second and third stage assuming JRC = 8. In case of JRC = 10 minimal limiting normal load is higher than normal load applied during any of the ASPERT stages. Table 11 below shows the shear strength of a joint calculated with Barton – Bandis criterion (equation 18) for hand measured values of JRC – 6 and 8. Following parameters were used for those calculations:

- JRC 6 and 8 according to hand measurements (see figure 55)
- Constant JCS = 218 MPa,
- φ_b = 33º, obtained from 20 repetitions of tilt test on sawn surfaces of the same material
- σ_n, = varying according to the ASPERT stage

Table 11. Shear strength of a joint estimated with Barton – Bandis criterion (equation 18) using following parameters:

Test stage	1st stage σ_n=4 kPa	2nd stage σ_n=6.6 kPa	3rd stage σ_n=9.2 kPa	4th stage σ_n=4 kPa
	τ [kPa]	τ [kPa]	τ [kPa]	τ [kPa]
JRC = 6	7.34	11.48	15.46	7.34
JRC = 8	10.9 - linear	17.33	22.77	10.9 - linear

- RELATIONS BETWEEN THE SHEAR STRENGTH, NORMAL LOAD AND JOINT ROUGHNESS COEFFICIENT IN BARTON – BANDIS CRITERION

To study how the shear strength is influenced by the values of normal load and joint roughness coefficient in Barton –Bandis criterion, the sensitivity analysis was conducted. Two separate analysis were done in that case. First shows how the shear strength changes with the changing value of normal load. This analysis was conducted for three different values of JRC – 21.5, 19.2 and 8. Those are the values obtained with photogrammetric prediction and graphical and hand profiling methods.
Analysis on how the value of $\arctan(\tau/\sigma_n)$ is influenced by changes in normal load was already presented in this chapter. Results are shown in figure 45 for photogrammetrically predicted JRC and figure 46 for JRC estimated with graphical method and hand profiling. Analysis of relation between τ and σ_n was calculated using following parameters:

a) φ_b- 33º, obtained from 20 repetitions of tilt test on sawn surfaces of the same material
b) JRC- constant 21.5,19.2 and 8
c) JCS – 218 MPa (SONE POLO LABORATORIO, test on Grey Kuru Granite according to the standard EN 12371)
d) σ_n – Varying σ_n, range from 0.1 to 5.4 MPa in increments of 0.1. MPa

Results of that analysis are presented in figure 47 below. On this figure value of shear strength is presented as a function of normal load. Figure 47 consists of 3 functions – a separate function for each JRC value. Negative values of shear strength occurs only in case of high JRC values – 21.5 and 19.2. For JRC = 8 the values of shear strength stay positive throughout the whole range of values of normal load. As can be seen from the function for JRC = 21.5, for normal loads lower than 0.5 MPa shear strength τ has negative values, since the friction angle respective to them is bigger than 90º. Sudden jump in the values of shear strength can be observed when normal load reaches approximately 0.5 MPa. That is because for that value of normal load friction angle is approaching 90 º.

For both JRC values shear strength stabilize after the friction angle drops below 90º. That figure confirms the estimated limits of normal load for analyzed JRC values (see figures 45 and 46)

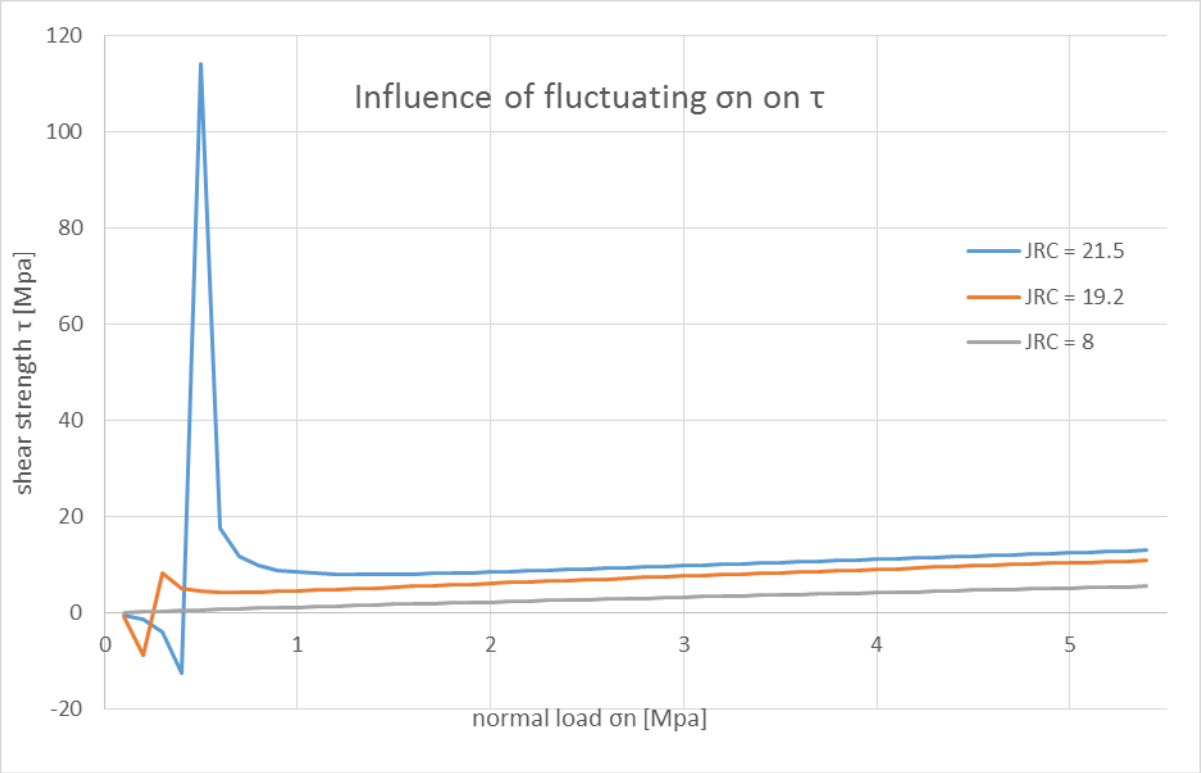

Figure 47 The relations between normal load, shear strength and friction angle in Barton – Bandis criterion (for constant JRC value 21.5 and 19.2)

The next analysis focuses on how the value of τ is influenced by changes in JRC values. Parameters used in this analysis look as follow:

a) Varying JRC value, ranging 1 to 42
b) Constant JCS = 218 MPa,
c) φ_b = 33º, obtained from 20 repetitions of tilt test on sawn surfaces of the same material
d) Constant σ_n, = 4 kPa

Figure 48 below shows the relation between the value of τ and the value of JRC. For low JRC values (from 1 to 12) the values of τ are positive and range from 0.03 MPa for JRC = 1 to 0.05 MPa for JRC = 11. That range of JRC and τ values corresponds to the range of friction angle values $\arctan(\tau/\sigma_n)$ of 38º for JRC 1 to 85º for JRC = 11. After that, the value of friction angle approaches 90º and the sudden increase in values of shear strengthy occur. When the values of friction angle rise above 90º the values of shear strength drop below zero and stay negative for the whole remaining range of JRC values – 12 to 42. The friction angle of 70º occurs for the JRC value of 7. That result leads to conclusion that the Barton – Bandis criterion in cases of σ_n = 4 kPa can only be applied for the joints which JRC is equal to 7 or less.

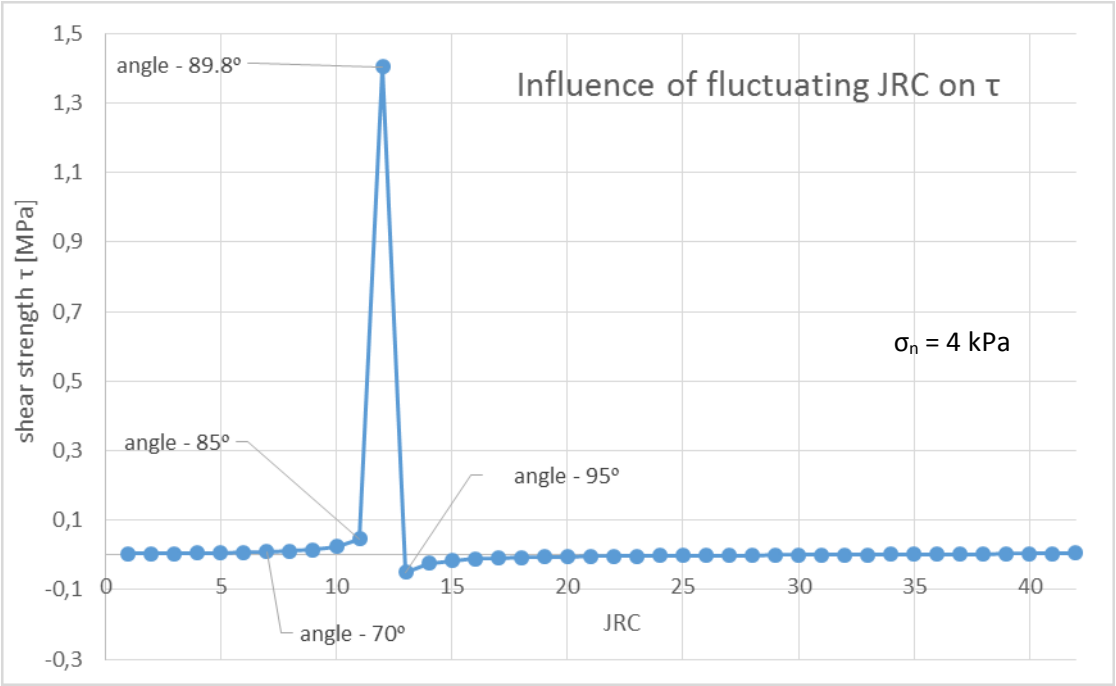

Figure 48 Relation between JRC and shear strength in Barton – Bandis criterion (for constant normal load of 4 kPa

In figure 48 above it can be seen that the value of arctan(τ/σ_n) is reached already for the JRC value of 7. As it has been mentioned before, according to Barton and Choubey (1977), for this level of normal load Barton – Bandis criterion cannot be applied for the joints which JRC is higher than 8. That also confirms that the limitation of Barton – Bandis criterion is defined by both normal load and joint roughness coefficient. In case of joints of high JRC values the limiting normal load would be higher than in case of less rough joints.

That conclusion is illustrated by the figure 49 below. This figure presents the shear stress in Barton – Bandis criterion as a function of normal load. Figure compares this relation for 5 different values of JRC: 21.5, 19.2, 10, 8, and 6. Those are the values obtained with photogrammetric prediction, graphical method and hand profiling. In case of JRC = 21.5 and 19.2 curvilinear form of the $\tau - \sigma_n$ envelope is very apparent. The applicability of Barton – Bandis criterion for those values of JRC is constrained with the normal load of respectively 4.2 and 2.6 MPa. For lower JRC values – 10, 8, and 6 the normal loads limiting applicability of Barton – Bandis criterion are significantly lower and equal to 0.044 MPa, 0.0052 MPa and 0.0002 MPa respectively (see figure 46).

Figure 49 shows the positive relation between the value of JRC and the normal load limiting applicability of Barton – Bandis criterion. That relation is presented more clearly in figure 50 which presents the normal load limiting the applicability of the criterion as a function of JRC value in ASPERT conditions. Based on that, it can be concluded that the photogrammetric prediction of shear strength and peak friction angle with this criterion would have been more accurate if the values of JRC were not overestimated. That would allow to predict the values of shear strength and friction angle using the real criterion and not the linear approximation (equation 22).

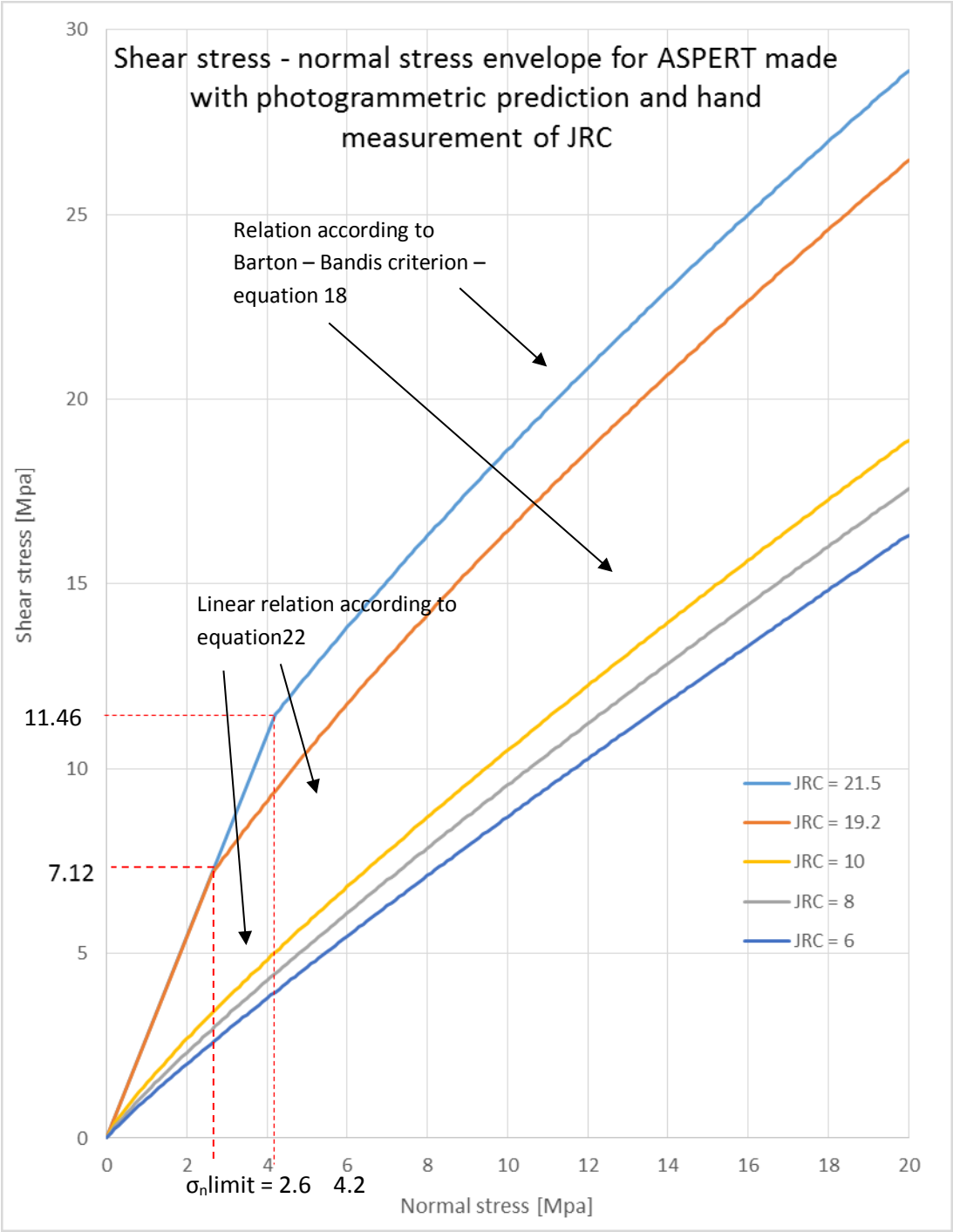

Figure 49 Relation between the shear and normal stress for ASPERT according to Barton – Bandis criterion, made with photogrammetric prediction (compare with figure 44). φb = 33°, JCS = 218 MPa.

As can be seen in the figures 49 and 50 a positive relation exist between the value of JRC and the value of normal load limiting the applicability of Barton – Bandis criterion. The relation between JRC and $\sigma_n$limit is presented in figure 46 below.

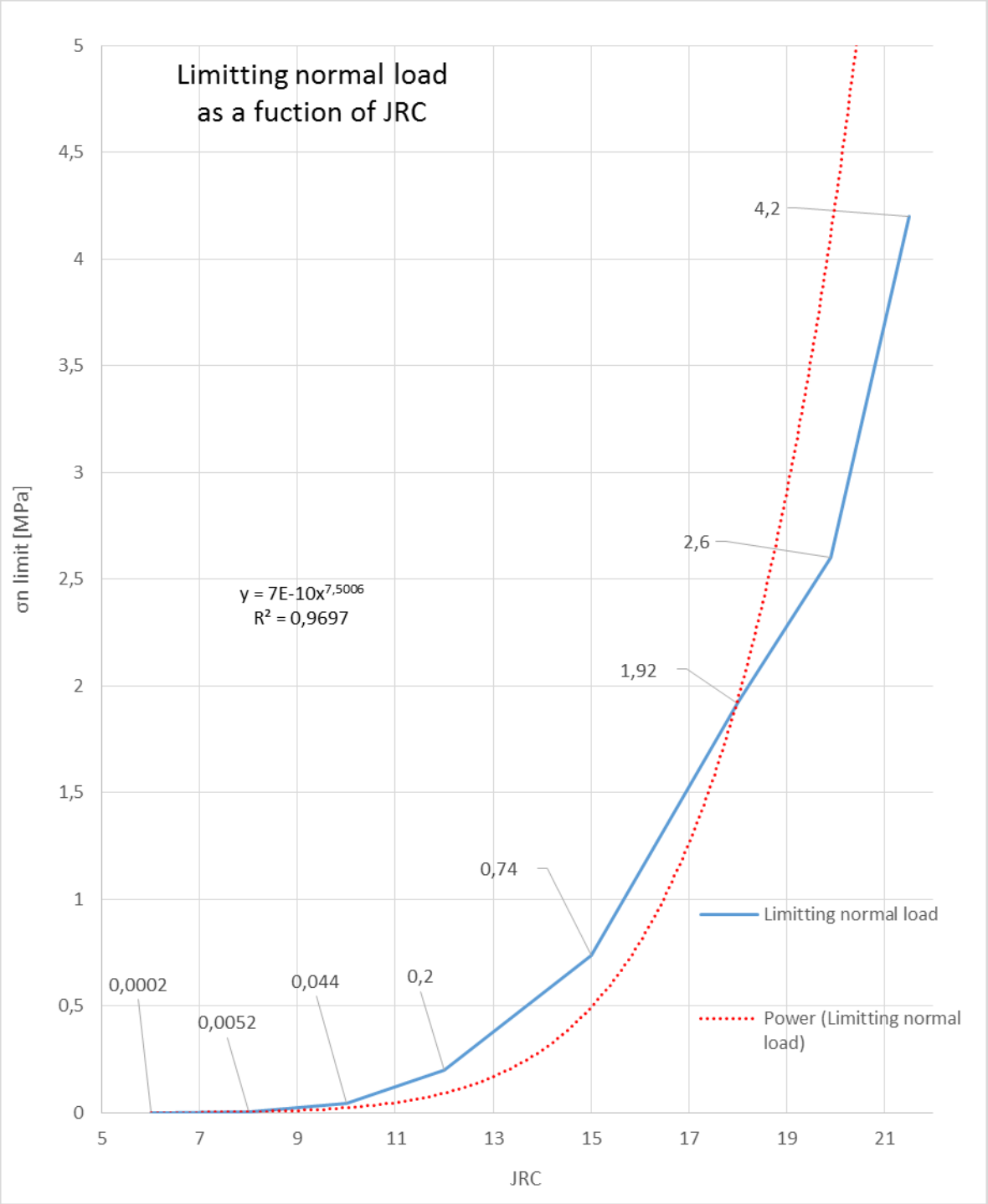

Figure 50 Relation between the value of JRC and value of minimal normal load limiting the applicability of Barton – Bandis criterion. φb = 33°, JCS = 218 MPa.

The relation between JRC and minimal normal load in Barton – Bandis criterion (equation 18) can be represented with a power trend line. The power function and R^2 correlation coefficient are displayed in the figure.

7 Aalto Shear Pull Experiment for Rock Tensile fracture ASPERT

7.1 Presentation of the results

7.1.1 First stage

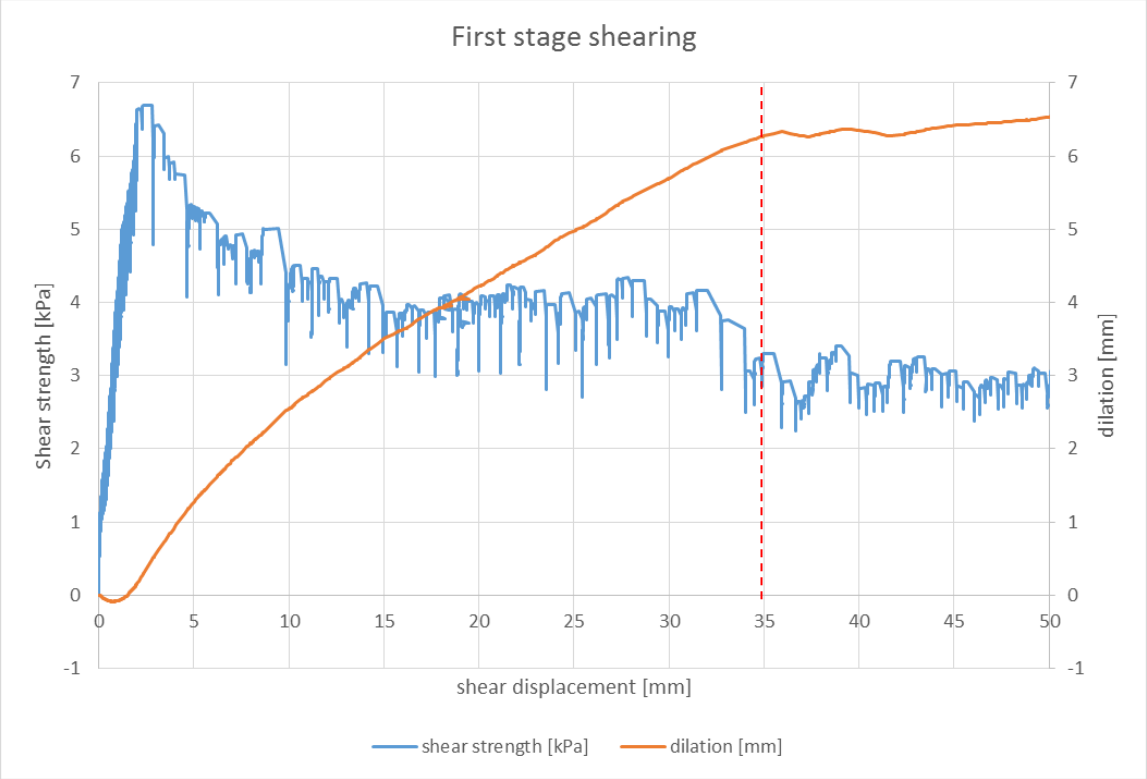

Figure 51 First shearing stage.

Figure 51 shows the graphical representation of the data from the first stage of experiment. Represented pieces of data are joint´s shear strength [kPa] and sample´s dilation [mm] as a functions of shear displacement [mm]. The red dashed line represents the threshold of calculating the residual shear strength. The residual shear strength is an average value of the readings from red line onwards. Presented dilation value is an arithmetic average of readings from LVDT´s 5, 6, 7, and 8. Value of shear displacement is also an average of readings from LVDT´s 2 and 4. Both graphs present the raw data from experiment and consist of 118 082 data points. Table 12 below contains the most important parameters of the test. It is important to notice that in the methodology we used, the displacement control was executed towards the hydraulic cylinder, not the sample itself, values in the last two rows of Table 12 regard the movement of the sample. The difference between the set up value of shearing rate (0,1 mm/min before peak and 0,5 mm/min after peak) and the actual sample´s shearing rate originate from constrained stiffness of the test setup (usage of chains) and consequently slip stick phenomenon occurring during the test.

Table 12. First shearing stage

Test parameter	**Value**
Normal load	constant, 4 kPa
Peak shear strength	6,7 kPa
Residual shear strength	2,7 kPa
Shear displacement at the moment of peak	2,791 mm
Total testing time	196,72 min
Sample´s hearing rate before peak	0,03 mm/min
Sample´s shearing rate after peak	0,51 mm/min

Table 13 below, shows the behavior of the spatial behavior of the sample during the test - maximum, minimum, average and final values of dilation and sideways (lateral displacement) of the sample. LVDT No 5, 6, 7, and 8 represent dilation while 9 and 10 sideways displacement (Figure 39).

Table 13. First shearing stage

value	Value of LVDT_No [mm]					
	_5	_6	_7	_8	_9	_10
maximum	8,577	9,319	5,580	6,421	2,283	0,119
minimum	-0,051	-0,245	-0,026	-0,287	-0,252	-1,179
maximum of average	6,567				x	
minimum of average	-0,088					
at the end of the test	7,673	9,024	5,577	6420	0,851	-0,952

7.1.2 Fast loading

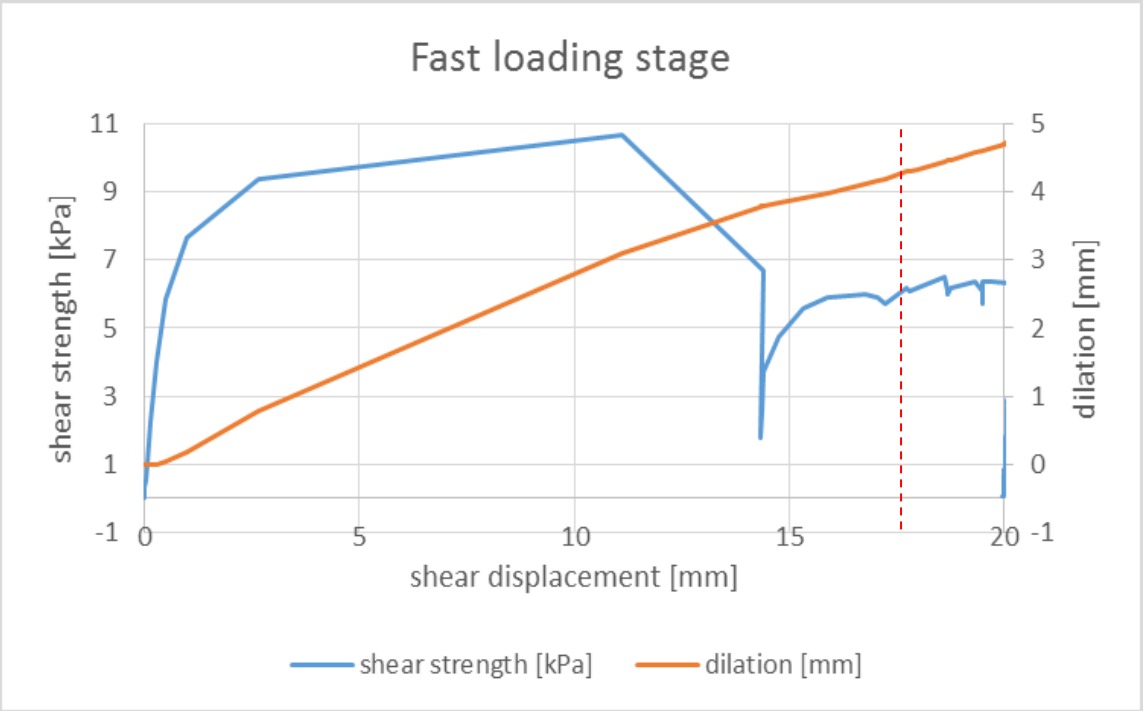

Figure 52 Fast loading stage

Analogically to previous chapter figure 52 presents the dilation of a sample and shear strength of a joint as a function of its shear displacement during the fast loading stage. The residual shear strength is an average of the shear strength values from the red dashed lines onwards. Dilation value is an average of readings from LVDT´s No 5, 6, 7, and 8, shear displacement – 2 and 4. Data presented in figure 52 is not modified, both graphs consist of 2 664 data points. Tables 14 and 15 below present the parameters and most important values from the test (Table 14) as well as sideways and vertical displacement during (maximum, minimum, average) and at the end of the test (Table 15).

Table 14. Fast loading stage

Test parameter	**Value**
Normal load	constant 6,6 kPa
Peak shear strength	10,7 kPa
Residual shear strength	3,3 kPa
Shear displacement at the moment of peak	1,011 mm
Total testing time	4,35 min
Sample´s hearing rate before peak	3,65 mm/min
Sample´s shearing rate after peak	4,65 mm/min

Table 15. Fast loading stage

value	Value of LVDT_No [mm]					
	_5	_6	_7	_8	_9	_10
maximum	5,110	5,171	4,344	4,288	1,304	0,000
minimum	-0,001	0,000	-0,078	-0,094	-0,233	-1,066
maximum of average	4,724					
minimum of average	-0,002					
at the end of the test	5,061	5,131	4,344	4,288	1,012	-0,956

7.1.3 Second shearing stage

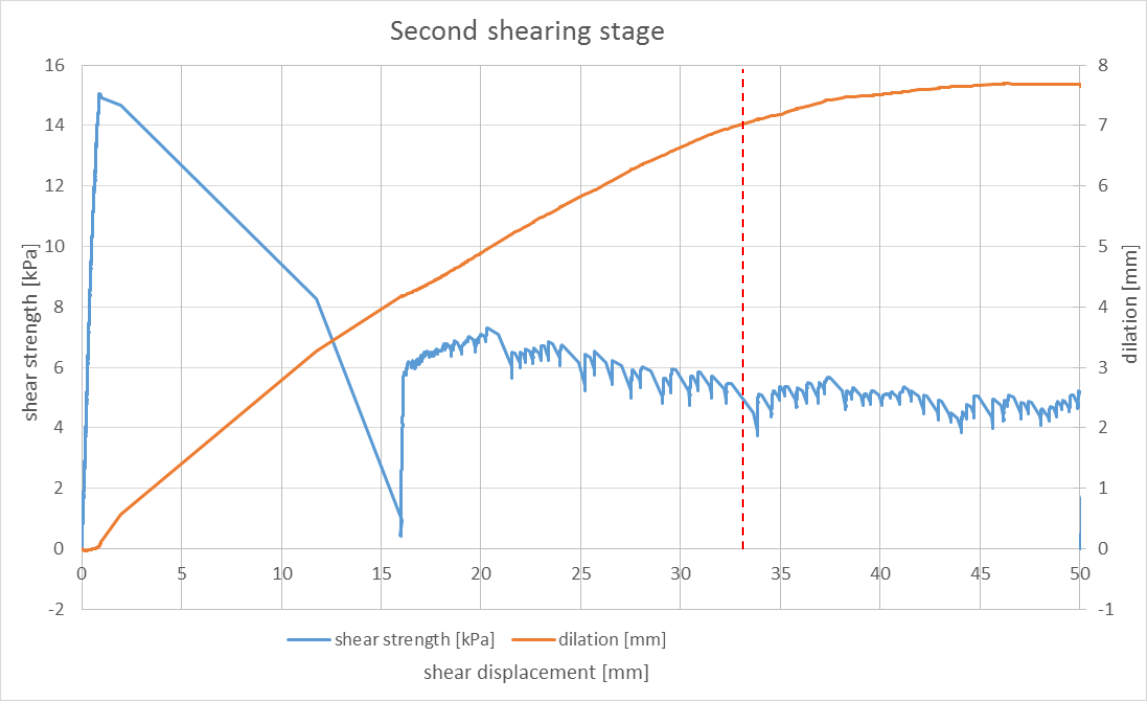

Figure 53 Second shearing stage

Analogically to previous chapter figure 53 presents the dilation of a sample and shear strength of a joint as a function of its shear displacement during the second stage of shearing. Residual shear strength was calculated as an average of the values of shear strength from the red dashed line onwards. Dilation value is an average of readings from LVDT´s No 5, 6, 7, and 8, shear displacement – 2 and 4. Data presented in figure 53 is not modified, both graphs consist of 111 262 data points. Tables 16 and 17 below present the parameters and most important values from the test (Table 16) as well as sideways and vertical displacement during (maximum, minimum, average) and at the end of the test (Table 17).

Table 16. Second shearing stage

Test parameter	**Value**
Normal load	constant 6,6 kPa
Peak shear strength	15,1 kPa
Residual shear strength	4,3 kPa
Shear displacement at the moment of peak	0,906 mm
Total testing time	185,35 min
Sample´s hearing rate before peak	0,01 mm/min
Sample´s shearing rate after peak	0,65 mm/min

Table 17. Second shearing stage

value	Value of LVDT_No [mm]					
	_5	_6	_7	_8	_9	_10
maximum	8,077	9,189	6,145	7,364	2,048	0,306
minimum	-0,002	-0,038	-0,079	-0,050	-0,133	-0,850
maximum of average	7,690				x	
minimum of average	-0,030					
at the end of the test	7,780	9,023	6,142	7,364	0,553	0,157

7.1.4 Third shearing stage

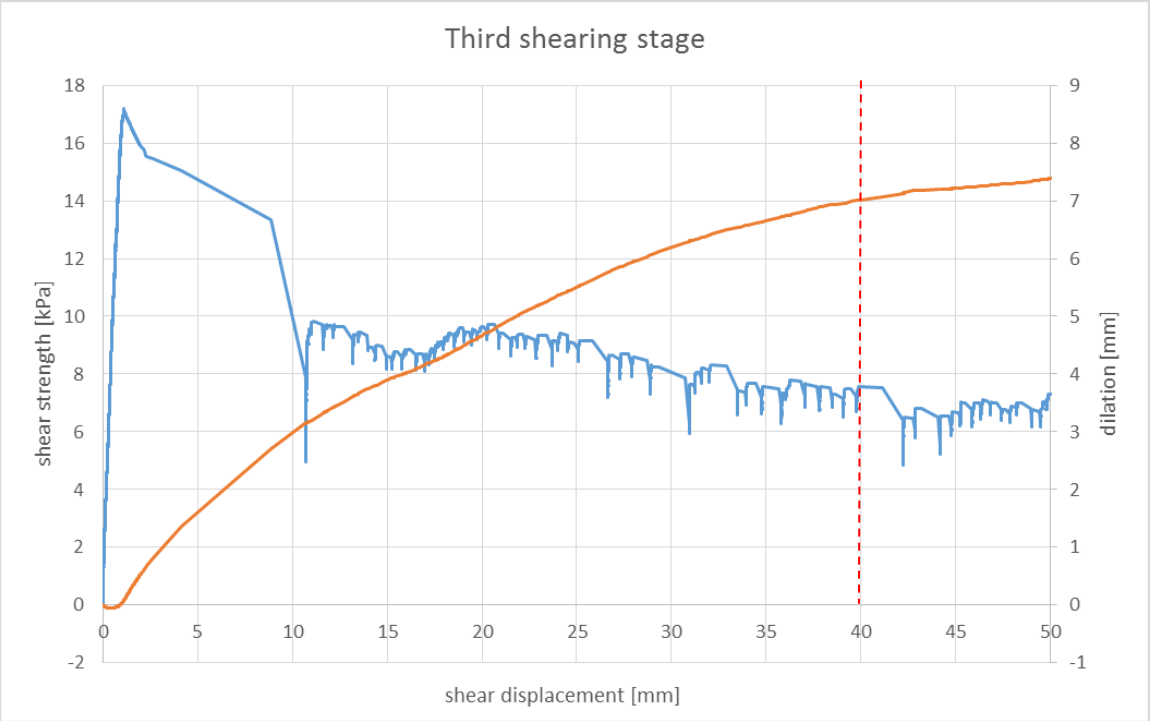

Figure 54 Third stage shearing

Analogically to figure 53 figure 54 presents the dilation of a sample and shear strength of a joint as a function of its shear displacement during the third stage of shearing. Residual shear strength was calculated as an average of the values of shear strength from the red dashed line onwards. Dilation value is an average of readings from LVDT´s No 5, 6, 7, and 8, shear displacement – 2 and 4. Data presented in figure 54 is not modified, both graphs consist of 96 495 data points. Tables 18 and 19 below present the parameters and most important values from the test (Table 18) as well as sideways and vertical displacement during (maximum, minimum, average) and at the end of the test (Table 19).

Table 18. Third shearing stage

Test parameter	**Value**
Normal load	constant, 9,2 kPa
Peak shear strength	17, 2 kPa
Residual shear strength	6,4 kPa
Shear displacement at the moment of peak	1,087 mm
Total testing time	160,74 min
Sample´s hearing rate before peak	0,02 mm/min
Sample´s shearing rate after peak	0,55 mm/min

Table 19. Third shearing stage

value	Value of LVDT_No [mm]					
	_5	_6	_7	_8	_9	_10
maximum	7,933	8,849	6,054	7,083	1,068	0,710
minimum	-0,003	-0,002	-0,132	-0,136	-0,142	-0,780
maximum of average	7,407					
minimum of average	-0,058					
at the end of the test	7,629	8,789	6,053	7,083	0,207	0,665

7.1.5 Fourth shearing stage

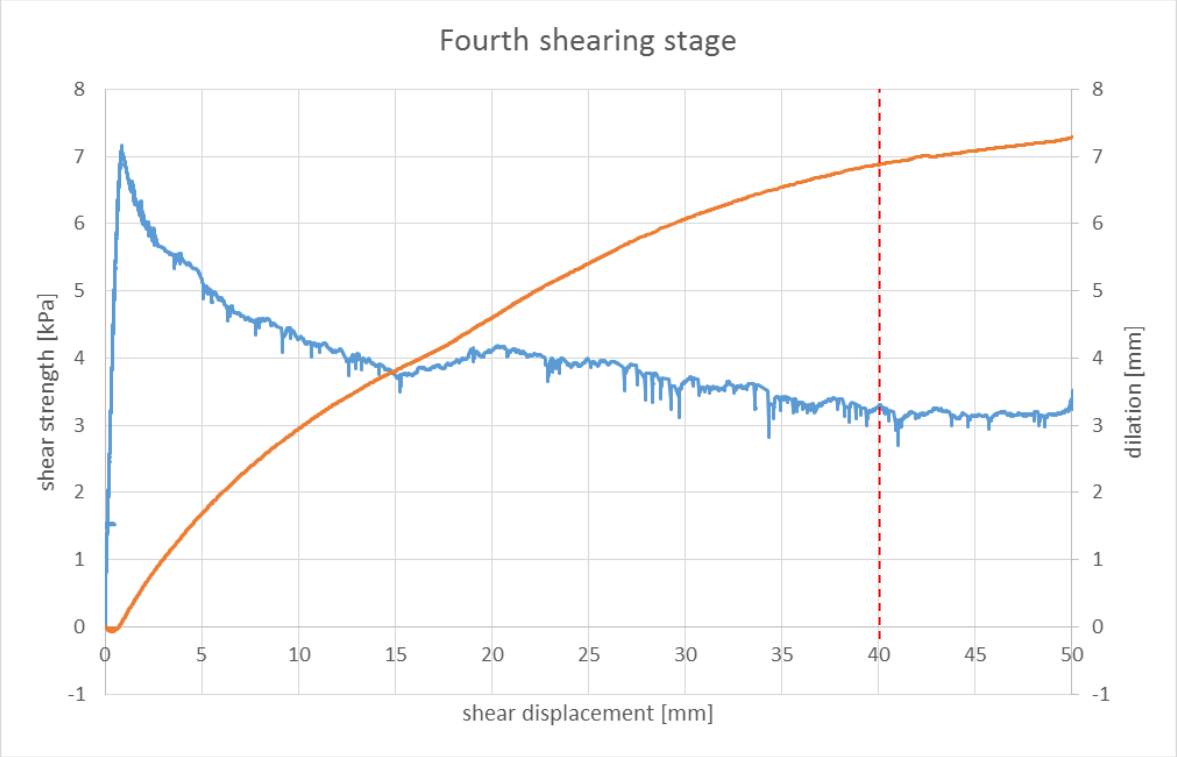

Figure 55 Fourth shearing stage

Analogically to previous chapters figure 55 presents the dilation of a sample and shear strength of a joint as a function of its shear displacement during the fourth stage of shearing. Residual shear strength was calculated as an average of the values of shear strength from the red dashed line onwards. Dilation value is an average of readings from LVDT´s No 5, 6, 7, and 8, shear displacement – 2 and 4. Data presented in figure 55 is not modified, both graphs consist of 109 632 data points. Tables 20 and 21 below present the parameters and most important values from the test (Table 20) as well as sideways and vertical displacement during (maximum, minimum, average) and at the end of the test (Table 21).

Table 20. Fourth shearing stage

Test parameter	**Value**
Normal load	constant, 4 kPa
Peak shear strength	7,2 kPa
Residual shear strength	3,1 kPa
Shear displacement at the moment of peak	0,846 mm
Total testing time	182,64 min
Sample´s hearing rate before peak	0,01 mm/min
Sample´s shearing rate after peak	0,51 mm/min

Table 21. Fourth shearing stage

value	Value of LVDT_No [mm]					
	_5	_6	_7	_8	_9	_10
maximum	7,900	8,779	6,059	6,984	0,708	0,503
minimum	-0,012	-0,037	-0,139	-0,181	-0,318	-0,643
maximum of average	7,368				x	
minimum of average	-0,009					
at the end of the test	7,658	8,719	6,055	6,983	-0,023	0,492

7.2 Interpretation of the results

7.2.1 Shear strength, friction angle and dilation of the sample.

Multi - stage testing methodology allows to make observations about the relation between the joint´s peak/residual shear strength and the normal load under which the test has been conducted. The ratio of normal load to the shear strength is known as a friction coefficient and its tangent represents the friction angle of a given joint (see table 1). The components of the friction angle which can be derived from the value of friction coefficient are φ_r+i, where φ_r is residual friction angle of a joint and i is the inclination of asperities (see chapter 3.2, equations 1 – 6, figure 3).

Table 22 presents a review of the results from all test stages. The value of shear displacement at the moment of peak presented in the fifth column is and average of the readings from the LVDT´s 2 and 4. Dilation at the end of the test is as well an average of the readings from LVDT´s No 5, 6, 7, and 8. It should be noted that for third and fourth stage of shearing, the average dilation at the end of the test was still increasing. For both stages the inclination of the dilation function at the end of the test was around 2.5º. The shear stiffness k_s presented in table 22 is a measure of resistance of a body to deformation. It is calculated by dividing the shear stress at the moment of peak by the shear displacement at the moment of peak.

Table 22. Comparison of the results from respective stages of ASPERT

Test stage [-]	Normal load [kPa]	Peak shear strength [kPa]	Shear displacement at the moment of peak [mm]	Shear stiffness k_s [Pa/mm]	Residual shear strength [mm]	Dilation at the end of the test [mm]
First	4	6,69	2,79	2 397	2,66	6,56
Second	6,6	15,06	0,91	16 618	4,29	7,65
Third	9,2	17,19	1,09	15 808	6,44	7,39
Fourth	4	7,17	0,85	8 474	3,12	7,35
Fast loading	6,6	10,68	1,01	10 563	3,33	4,71

The relation between normal load and peak/residual strength is presented in figure 58which shows combined results of all the test stages. The right part of the figure presents the shear strength of a joint during four stages of the test as a function of shear displacement. Value of shear displacement, is an average of the readings from LVDTs number 2 and 4 (figure 39). The left side of the graph present the peak and residual values of shear strength of a joint as a function of normal load during respective stages of the test.

It can be observed that in case of residual shear strength the relation of shear strength and normal load is nearly linear. The red dashed line going through the plot is the linear trend for this data. The inclination of the trend line is equal to 35º, therefore the conclusion can be made that the value of residual friction angle is around 35º. In case of peak shear strength the relation to normal stress is clearly not linear.

The inclination of dashed lines connecting the intersection of X and Y axes with the respective points on the function represent the values of peak friction angle at each shearing stage. For the first stage that value was 59º, for the second stage - 66º and for the third 62º.

As it has been mentioned in the beginning of this chapter analysis of relationship between the normal load and shear stress provides with information about the roughness of the tested joint surface. Additionally, for CNL conditions, the component representing the inclination of asperities i can be derived from the tangent of the ratio of dilation to shear displacement (Poturovic et al, 2015). Comparative analysis of both angles: φ_r+i, and i can be used to characterize the residual friction angle and identify the moment in the test where the residual state was reached. Figure 57 below shows the values of φ_r+i, and i for each of the shearing stages. When the angle of dilation (i) stabilizes at around 0º that indicates that the residual strength was reached, and for this value of I the tangent of friction coefficient represents the residual friction angle since φ_r+i = φ_r when i = 0. Analogically, the peak friction angle occurs for the highest angle of dilation since the value of φ_r+i is the biggest when i = max.

$$\tan i = \frac{dv}{du}; (22)$$

$$\tan(\varphi + i) = \frac{\tau}{\sigma_n}; (23)$$

where:
i –dilation angle/inclination of asperities
dv – incremental increase in vertical displacement values (dilation)
du – incremental increase in horizontal displacement values (shear displacement)
τ- shear stress during the respective test stage
σ_n- normal load during the respective test stage (in case of ASPERT its constant for each stage and equals to 4kPa in first stage, 6,6 kPa in second, 9,2 kPa in third and 4 kPa in fourth

The table 23 below shows the values of peak and residual friction angles for each stage extracted from the data presented in figure 56. From the figure 56 it can be noticed that the dilation angle at the end of the test fluctuates around the value of zero but does not stabilize at this value. For that reason, residual friction angles were selected for the lowest values of dilation angle in the last millimeters of shear displacement, which was not necessarily the last reading. Because of that, values of residual friction angle presented in the table 23 might be slightly overestimated, especially in case of the fourth stage of shearing, where the dilation angle was equal to 3º. That means that the value of residual friction angle for this stage was probably overestimated with about 3º. This fact indicates that the total shear displacement was not enough and the sample should have been sheared for few millimeters more in order to reach its residual state.

Yet, the values of peak friction angle presented in table 23 correspond well with the same values presented in figure 57. The slight discrepancies between the results comes from the fact that the value present in the figure 57 is an inclination of the linear trend between the said four data points.

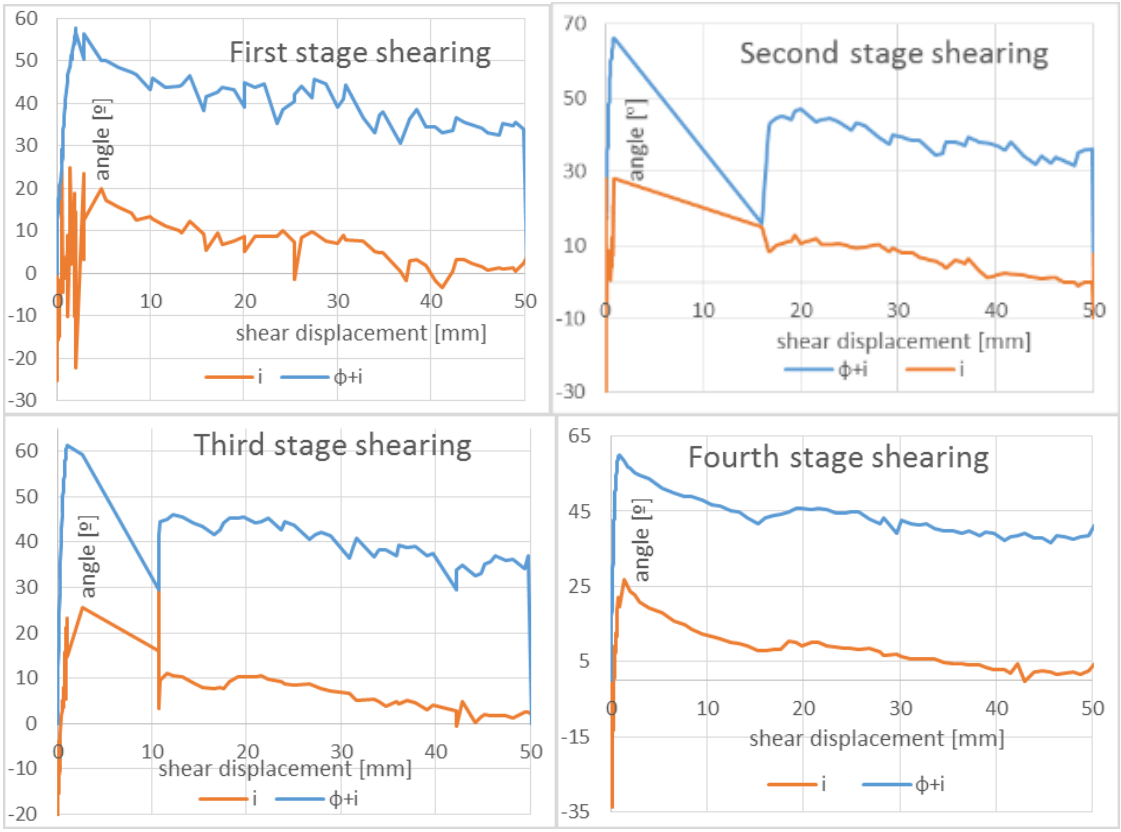

Figure 56 The values of dilation and friction angle recorded during the respective stages of shearing as a function of shear displacement.

The dilation and friction angle were calculated according to the equations 22 and 23. To eliminate the influence of the noise, every 1000th reading from the experiment data was taken into account during creation of this figure.

Table 23. Values of peak and residual friction angle calculated based on the value of dilation and the ratio of $\tau / \sigma_n = \varphi_b + i$

parameter	first stage shearing	second stage shearing	third stage shearing	fourth stage shearing
peak friction angle	59^o	66^o	62^o	60^o
residual friction angle	33^o	33^o	33^o	37^o
dilation angle read for ϕ_r	0.8^o	-0.2^o	0.3^o	3^o

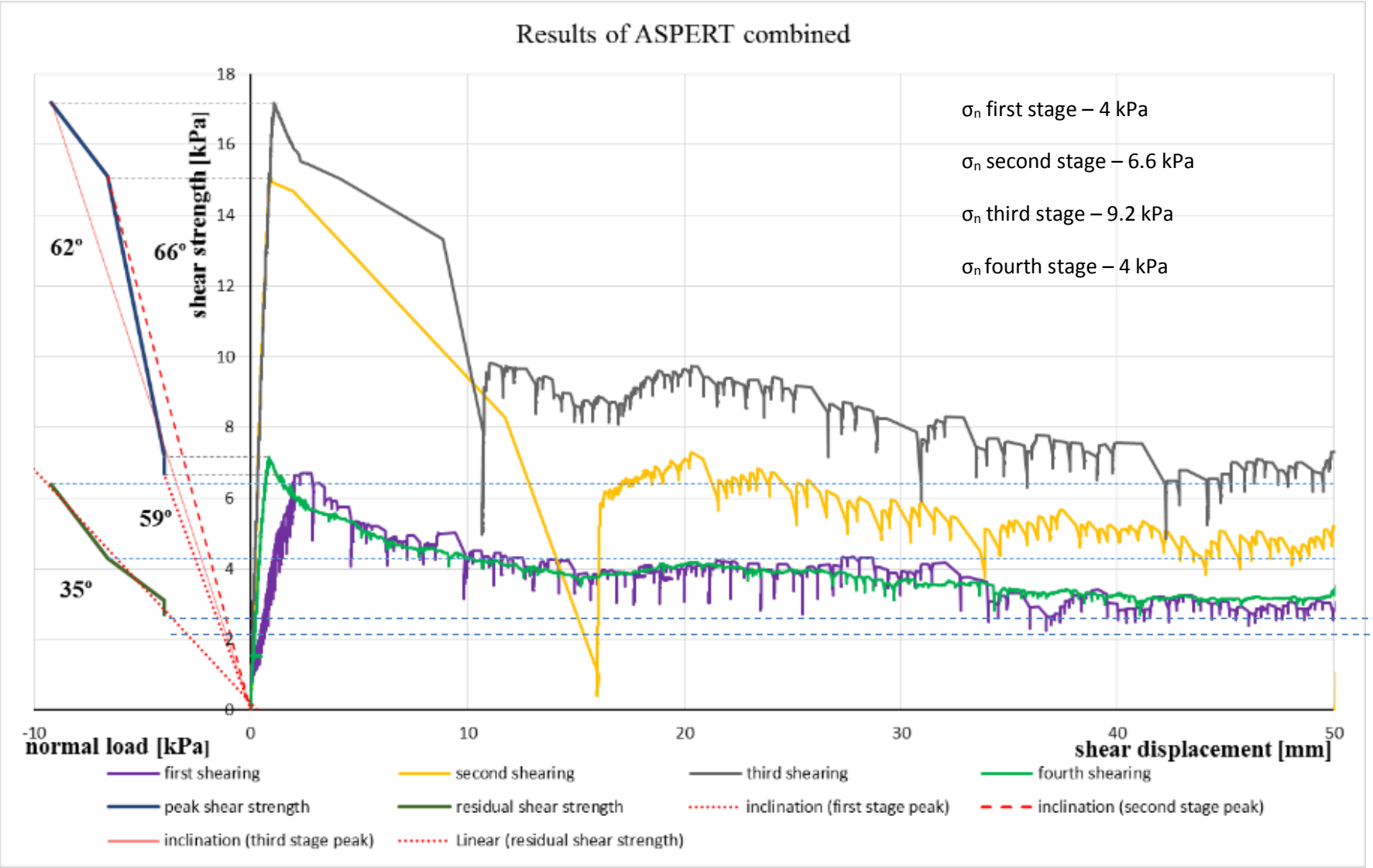

Figure 57 Results of ASPERT. Left side of the graph presents the relation between shear strength and normal load, right between the shear strength and shear displacement in respective stages of the test

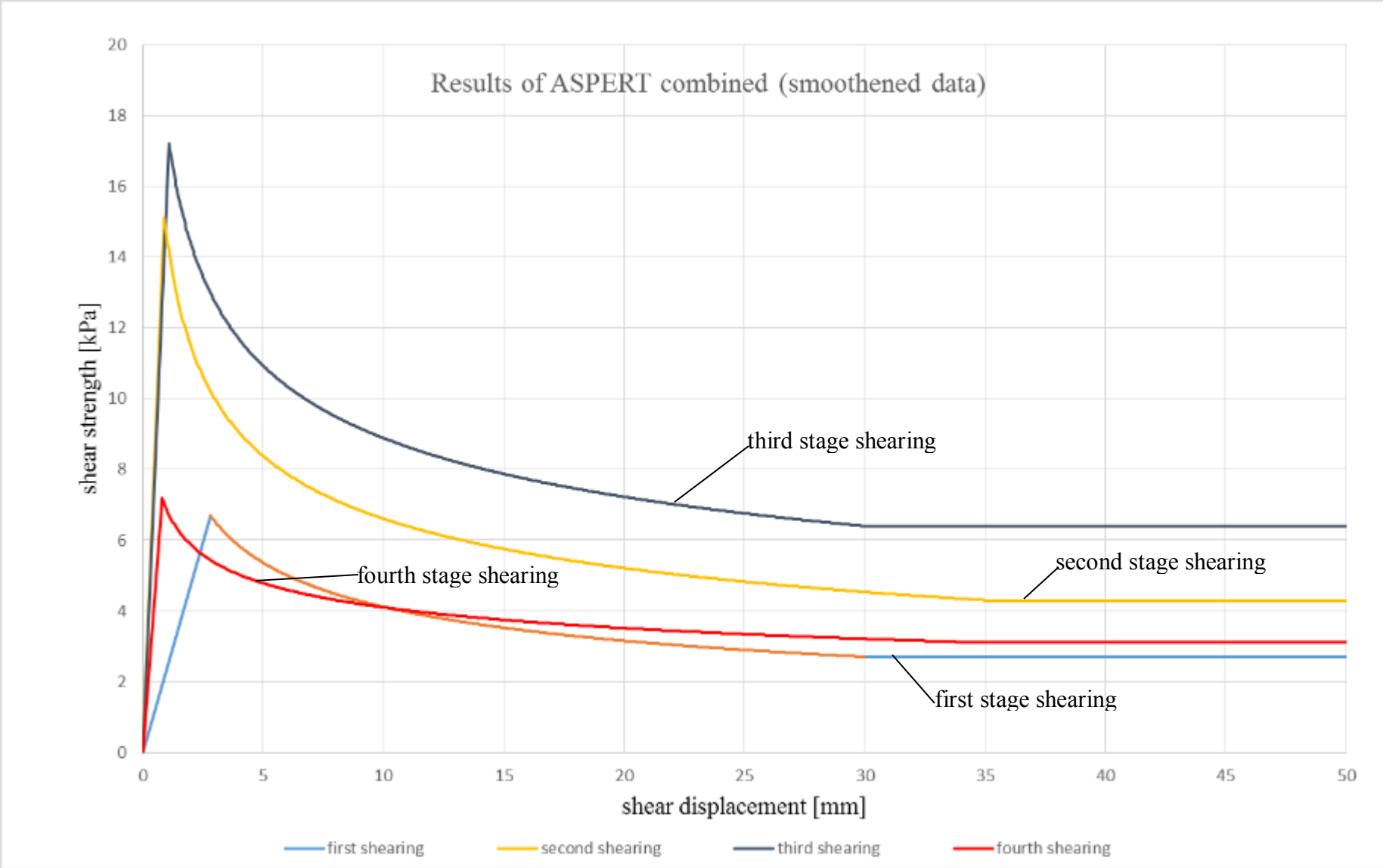

Figure 58 Results of ASPERT, shear strength of a joint as a function of shear displacement. Graph presents modified, smoothened data, without the influence of stick – slip phenomenon.

Interesting observation which can be made based on table 22 and figure 57 is that both peak and residual shear strength of a joint for fourth shearing stage is lower than the same values for the first shearing stage, which is a very surprising result. Since during the second and third stage of shearing the sample surface was altered, one would expect lower results in the fourth stage. The explanation for this might be the mistake in methodology which is further discussed in 8.2.

From the figure 57 and table 22 it can be observed that the peak shear strength have occurred for about 1 mm of shear displacement for all shearing stages, except for the first stage. Surprisingly, in the first stage of shearing the peak value of the shear strength was recorded at approximately 3 mm of shear displacement. Generally, the shape of the curve for the first stage shearing differs slightly from the other 3. The part of the curve which represents the elastic behavior of the joint is much less inclined for the first stage shearing than for other stages, where it is almost vertical. It is unknown where the difference originates from, possibly it is due to the lack of consolidation stage prior to the test. However, the behavior of the joint during the first shearing stage was more elastic which may suggest that sample surface might have been more slippery due to some residue from the sawing process left on the sample surface– which might be oil or dust. Anyway, that explanation is questionable since I cleaned sample carefully prior to the test, removing all of the dust residue from sawing. No signs of oily residue were detected on the sample surface (e.g. change of color), anyway I did not use alcohol or acetone to clean the surface of the joint, so if some oily residue was coating the sample surface it was not removed and therefore could have affected the results of first stage in ASPERT. Sawing was done with usage of water but during the test sample was dry.

Another discrepancy in the results from first stage shearing is the average dilation at the end of the test (see table 22). For second, third and fourth shearing stages that value was around 7.5 mm while for first approximately 1 mm less. And last but not least, the sideways movement of the sample was the biggest during the first stage of shearing, excluding fast loading (see table 13)
For LVDT No. 9 it was roughly 0.85 mm (positive), while for 10 - -0.95 (negative). In other stages both values were positive (or slightly negative in fourth stage) and significantly lower. Because the barrier blocking the sideways movement was not stiff enough, sample was free to move slightly and find the path of least resistance to shear. The question is, why did it not do it in other stages. The answer to that question might be found in the values of dilation before peak. For first stage of shearing those values remained negative for much bigger shear displacement than in other stages. Decreasing values of dilation indicate that the joint was closing or setting up to the correct position. That suggests, that during the first stage of ASPERT the opposite sides of the sample were not positioned correctly on top of each other, therefore at the beginning of the test sample was adjusting to the correct position, and that extended the negative dilation and delayed the occurrence of peak. That hypothesis is explained and studied further in chapter 8.2.

From the raw data (figure 57) it can be clearly seen that the shear movement of the sample during all the test stages was not continuous and smooth. On all graphs, it can be noticed that after peak, any shear displacement was occurring after the increase in the shear strength. The reason for that is mentioned already in the chapter stick-slip phenomenon. Which means that the sample was moving in waves, as the joint surfaces were changing between the stages of sticking together and top surface sliding over bottom.

That phenomenon is caused by the changes in the friction force between touching surfaces depending if they stay static or move. Because static friction coefficient is higher than, relatively big force is needed to start the movement of the sample.

At the moment when the sample starts moving, the friction force to be overcame decreases significantly and that leads to sudden jump in the movement of the sample.

At this point, the chain works like an elastic spring which can accumulate the energy. When energy accumulated before the movement starts is released during the movement and decreases to the point when kinetic friction cannot be overcame the sample stops moving and because of increasing pulling force, the chain is accumulating energy again.

That is especially noticeable in case of second and third stage shearing. The displacement before peak is very small, at the moment of peak the level of static friction is reached and sample accelerates suddenly. Friction force is decreased to its kinetic level and energy is released suddenly. During the second stage, after reaching the peak sample moved roughly 1,5 cm in 0,4 of a second before it stopped and the chain started accumulating the energy again. This is the reason, why the shearing rate was the highest in the second stage of shearing (table 16), the result was affected by the sudden jump after peak. The same phenomenon in a smaller scale can be observed through all of the graphs.

Stick slip behavior of the joint is analyzed in figure 59.

Although stick-stick slip phenomenon present during the test have contaminated the data and influenced the shearing rate, it gives us information about the static and dynamic friction of tested sample. The static and dynamic residual friction angle can be calculated when only the highest points of the residual part of certain curve are averaged. Analogically the dynamic residual shear strength is an average of lowest points of residual part of certain curve. The left part of figure 59 below presents the dynamic and static residual shear strength of the joint as a function of the normal load during respective stages of the test. The static and dynamic residual shear strength were calculated by averaging the points from the same range as in case of general residual strength, but instead of taking all points into consideration, only the points from before drop (highest) were taken into account in case of static friction and from after drop (lowest) were taken into account in case of dynamic friction. Analogically to figure 58 inclination of the linear trend between those data points gives the value of residual static and dynamic friction angle. As can be seen in figure 59, static friction angle is equal to 39º and the dynamic friction angle is equal to 35º. The right part of figure 59 presents the stress - strain behavior of a joint in 4 test stages. Red points marked on a curve from the third stage shearing serve as an example on how the static and dynamic strength were calculated.

Figure 58 above shows the data with removed influence of the stick-slip phenomenon. Data presented on this figure is an interpretation and should not be confused with the real data. Only values of peak and residual shear strength were preserved. The shape of the curves was changed to improve readability of the graph.

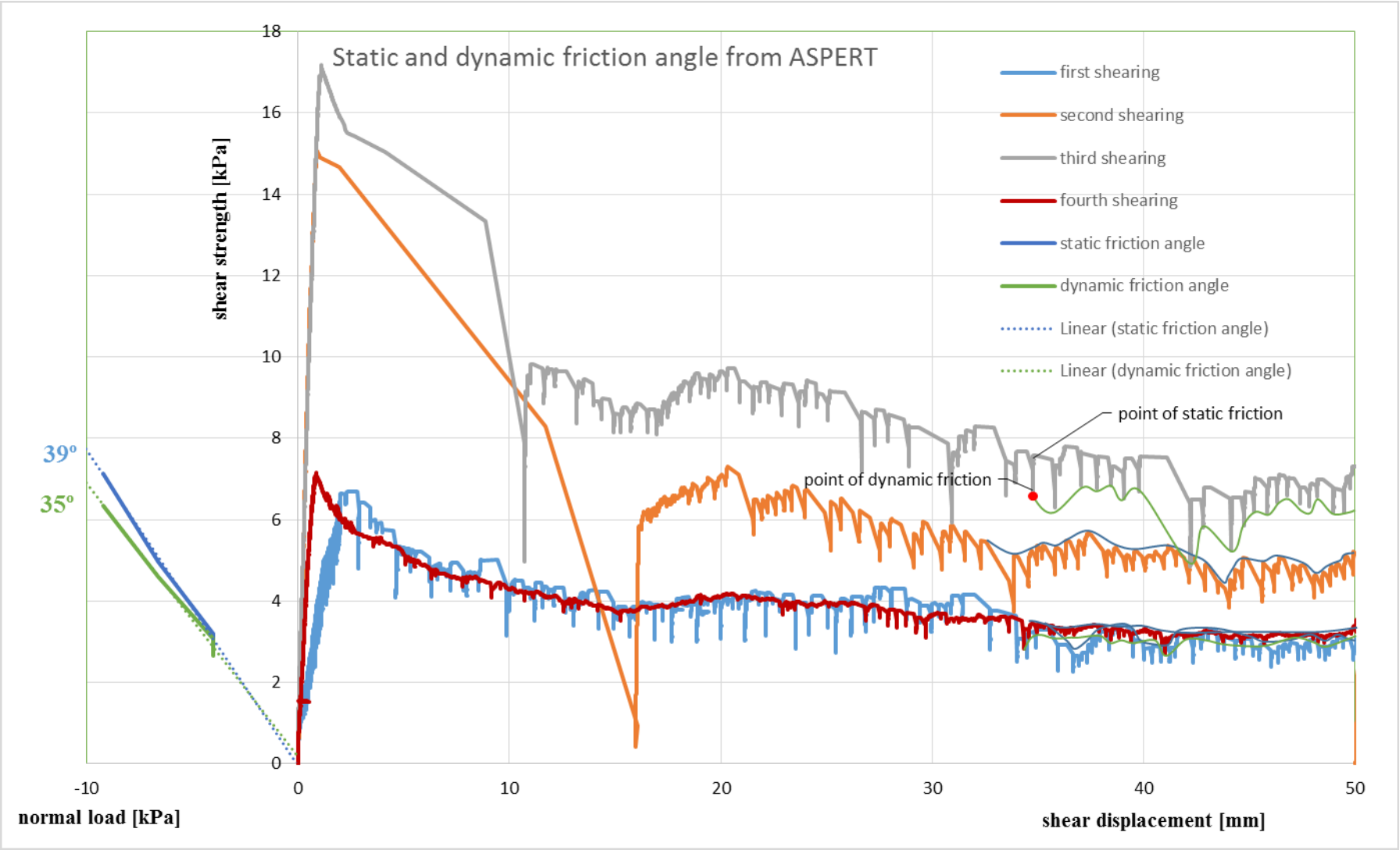

Figure 59 Results of ASPERT representing the static and dynamic friction. Left side of the graph shows the static and dynamic friction angles, right, stress strain behavior of the joint

7.2.2 Damage analysis

After each stage of the test the bottom part of the sample was checked for the damage zones left after the shearing. The damaged areas were marked, on the sample surface after each of the consecutive shearing stages. Since the fourth stage of shearing was made without increased normal load no new damage zones were created during that stage.

Figure 60 below shows the damage map on the bottom surface of the sample after all stages of the pull test. Blue marks represent the damage zones made during first stage of shearing (normal load 4 kPa), damage zones made during the second shearing stage (normal load 6.6 kPa) are presented with green marks and the red marks represent the damage zones created during the third stage of shearing (normal load 9.2 kPa). First observation which can be made from this figure is that the damage zones made during the first stage of shearing are concentrated in the front of the sample surface, on the half closer to where the pull force was applied. Since the fracture was created by tensile force the roughness of the sample surface before test was independent on the direction, therefore isotropy of the asperities height cannot be considered as a reason for that fact. What might be considered as a reason is the possibility that the sample surfaces were not put together precisely in a correct position, and the front of the sample was placed off center. The location of damage zones made during the second and third stage do not reveal any directional dependence and seem to be distributed evenly throughout the sample surface. In total 18 damage zones were created during the first shearing stage, 9 during the second stage and 11 during the third stage.

From the experiment data, it can be concluded that the damage done to the surface was not significant. The results of the first and fourth stages of the pull tests without any external normal load do not differ significantly (Figure 57). In the shear stress vs shear displacement curve for the fourth stage of shearing the peak of the shear strength is sharp and noticeable which suggest that the surface was not altered significantly by the earlier stages of shearing. Yet, after the fourth stage of shearing, no new damage zones were localized on the sample surface.

Low alteration of the sample surface after the test is not surprising in that case. Normal loads used during the testing were rather low. CNL testing conditions made it easier for the sample to dilate than to shear and actually break some asperities off at their base. The only breakage that occurred was on the tips of the asperities

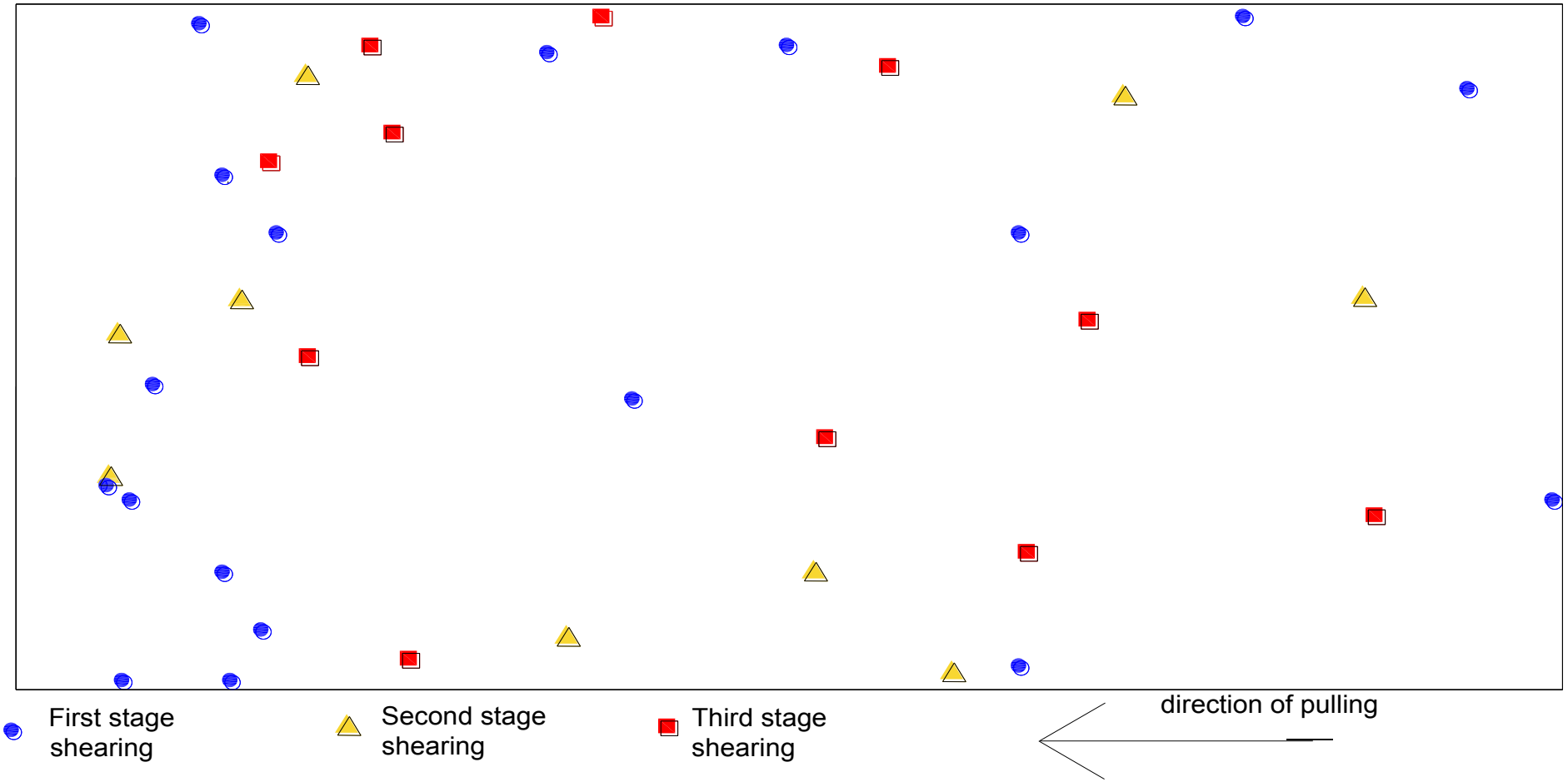

Figure 60 Map of the damage on the bottom half of the sample done during respective stages of ASPERT.

Blue circles represent the damage from the first test stage, yellow triangles from the second and red squares from the third. No new damage zones were located on the sample surface after the fourth stage of shearing

8 Errors analysis

Interpretation of results of both photogrammetric prediction of the joints roughness and friction angle and experimental determination of the joints shear strength using the pull test have revealed some mistakes in the methodology. In this chapter, the errors and mistakes are analyzed.

8.1 Photogrammetric prediction of joint´s roughness and friction angle

The results of photogrammetric prediction are unsatisfactory due to the low density of produced point clouds. The ISRM standard for shear tests of rock joints (ISRM, 2014) as well as the authors of the method for directional roughness analysis (Tatone and Grasselli, 2009) suggest that in order to characterize the features of surface roughness precisely enough for the shear damage done by shear test to be detected the nominal distance between the points in the point cloud should be < 0.5 mm. According to that requirement, for the sample size I used in this study one model should consist of more than7 600 000 points, while my models are consist of 1 6 55 666 points minimum to 3 406 850 points maximum. Perhaps for such sample size different photogrammetry technique should be used, some which does not require the complete overlapping of pictures but allows to photograph the object in parts. That would allow to reduce the distance from camera to object significantly and therefore improve the resolution of the photographs. Additionally, better equipment could be used to achieve the target density of the point clouds. Another problematic aspect of the results of photogrammetric prediction is their inconsistency. The density of the point cloud of the bottom sample surface before test is significantly lower than the density of the point cloud of the same surface after test. The number of points in the model after test is twice as big as the model of the same surface before test. The model of the top joint surface after the test is also less dense than in case of analogic model from before test. The number of points for point cloud after test is 2 658 544, while for top surface before test it is 3 267 383. That discrepancy in the quality of created models makes the comparison of the results impossible, since one cannot say if the difference comes from the changes to surface done during the test, or from the difference in the quality of the models. In fact, the results of directional roughness analysis say more about the quality of the digital model of a surface than about the actual roughness of that surface.

After the test was conducted and digital models from after test have been created the bottom sample was photographed again using different methodology. This time hand held photogrammetry was used, so camera was not mounted on a tripod. While taking pictures, I followed the methodology developed in KARMO I, which is described in (Korpi, 2016). Pictures were taken from the floor, each time small part of the sample was photographed. The sequence of the pictures started at the corner of the sample and continued towards the longer side of the sample to the opposite side of the rock, like described it is described by Korpi (2016). In total 203 pictures were taken using 16 different camera heights. The distance between the sample and camera was varying from 120 cm to 40 cm. The pictures were then processed according to methodology described in chapter 5.2.2. Point cloud of the surface was created by following the methodology used for other models in this thesis described in chapter. Despite the fact that much smaller number of pictures were used to create a model, the point density of resulting point cloud was much higher. On average, the point density of created point cloud was **8 points/mm^2**, which gives the average point spacing of **0.3 mm**.

8.2 Aalto Shear Pull Experiment for Rock Tensile fracture (ASPERT)

The results of experimental studies using the pull test can also arise some questions about the possible mistakes in methodology. Especially questionable here are the results of the first stage shearing and the difference between the results of first and fourth stage of shearing. However it is possible that the damage to the sample surface done during the first, second and third stage of shearing was small enough for the fourth stage to not differ from first, the bigger values of peak and residual shear strength cannot be explained anyhow, but just with mistakes in methodology or differences in sample condition. The hypothesis, that the sample surface was contaminated with a residue from the sawing process was already mentioned in the previous subchapter. Yet, this is very unlikely to be the cause of the results inconsistency, since the sample was thoroughly cleaned from any dust prior to the tests. No signs of oil residue, such as changes in color, were present on the sample surface. More likely hypothesis is, that the position of the sample during the first stage shearing was not correct. That means, that the opposite sides of the sample were not aligned correctly and did not overlap each other as they should. What makes this theory more probable than the previously mentioned is the value of dilation during the first stage of shearing. As can be seen in the figure 61, the dilation value in the first stage of shearing remained negative much longer than in three remaining stages.

The dilation continued to be negative for around 1.5 mm of the shear displacement of the sample. In the other stages, the dilation values increased to above zero, before 1 mm of shear displacement was reached. The negative value of dilation is a sign that the joint was matching or finding the correct position. That can result from the poor matedness of a joint as well as from the opposite sides of the sample not being positioned properly at each other. Since in three other stages the dilation increased above zero much earlier it can be concluded that in the first stage incorrect positioning of the sample was the reason for remaining negative dilation values. The opposite sides of the sample first had to find the right position before the peak shear strength was reached. That can also explain bigger sideways movement during the first stage of shearing and the directionality of the damage zones created during that stage. Sample was moving sideways until it found the correct position, which could have resulted in creation of damage zones and peak shear strength occurring for much bigger shear displacement that in the other stages. That also possibly caused the elastic part of the curve for first stage shearing to be not as steep as in other cases, since the peak occurred later. Figure 61 shows the positive values of dilation for the first 5 mm of shear displacement for each of the shearing stages. As can be seen, the dilation graph of the first stage shearing intersects the value of zero the latest- at the value of shear displacement equal to 1.5 mm. For second, third and fourth stage of shearing this value is respectively 0.5 mm, 0.7 mm and 0.8 mm, which is significantly lower.

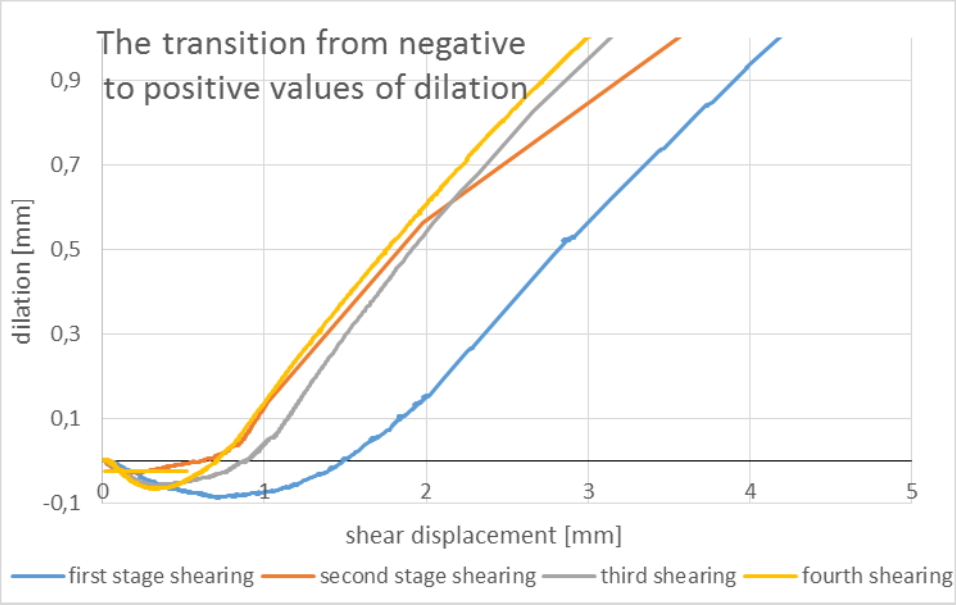

Figure 61 The transition from negative to positive values of dilation.

The jump in the displacement values for the first shearing, the horizontal part of the graph which shows the 0.5 mm displacement without any changes in applied shear stress is a measurement artifact and we believe it is caused by the cell phone being close to the shear displacement LVDTs.

That problem could have been prevented if the test arrangement included more reliable guiding facilities to position the samples on each other. During ASPERT test we used the aluminum beam attached to the top sample and the beams which were serving as a barrier for sideways displacement to direct the top sample correctly on the bottom sample. This arrangement seemed to be sufficient to us before test, but it turned out to be not, since even the smallest discordance could affect the results significantly. Additionally the process of positioning the sample was not easy since the sample was suspended on a crane and the steering system of a crane is not sensitive enough for this type of work.

The high elasticity of the test resulted with discontinuous movement of the sample due to the stick slip phenomenon. That caused a sudden jump in the sample movement during the second and third stage of shearing. The value of shear stress after peak fell below the value of residual shear strength of the sample and the applied shear stress was increased to the level where sample was moving again. In the second stage of shearing, the sudden release of energy resulted with over 15 mm of shear displacement in just 0.4 s. During the third stage jump in the sample motion was equal to about 10 mm and occurred in 0.9 s. The effects of stick slip phenomenon is the least visible in the fourth stage of shearing (see figure 57). The drops in the shear stress are relatively smaller and less frequent in comparison to the other stages. That may be an effect of surface damage, the tips of steepest and highest and steepest asperities were broken during the second and third shearing stage decreasing slightly the resistance of a joint.

Surprising influence of the stick slip phenomenon can be observed, again, on the results from first stage of shearing. Figure 62 presents the stress - strain relation during the all stages of shearing for the first 2 mm of shear displacement.

It can be clearly seen that the stick slip phenomenon was present also before the peak shear strength was achieved, which is unusual and did not take place in the second, third and fourth stage of shearing. Moreover, as can be seen in the figure 62, the parts of the graph where showing the drops in applied shear stress are inclined towards the point 0,0 which suggest that the sample was moving slightly backwards every time after the energy was released from the system. Of course that is only possible in case of a drop in applied shear stress caused by malfunction of the hydraulic cylinder and not by the overcoming of static friction value. In fact, if we look closer at the behavior of the cylinder during the first shearing stage (see figure 63), it appears that the cylinder was also displacing backwards together with the sample. Obviously, because cylinder was connected to the sample with a chain it could not push the sample back, so the backwards displacement of the sample could not have resulted from the displacement of a cylinder. The reason for that is most probably the malfunction of either the cylinder or the sensor measuring its displacement. That kind of backward displacement of neither the sample nor the cylinder does not occur in the data from after peak behavior during the first stage of shearing. It does not occur also at any moment of second, third or fourth stage shearing.

The effect of stick - slip phenomenon could have been minimized by increasing the stiffness of the testing arrangement by for example using shorter pulling chains or eliminate usage of chains by choosing push test methodology.

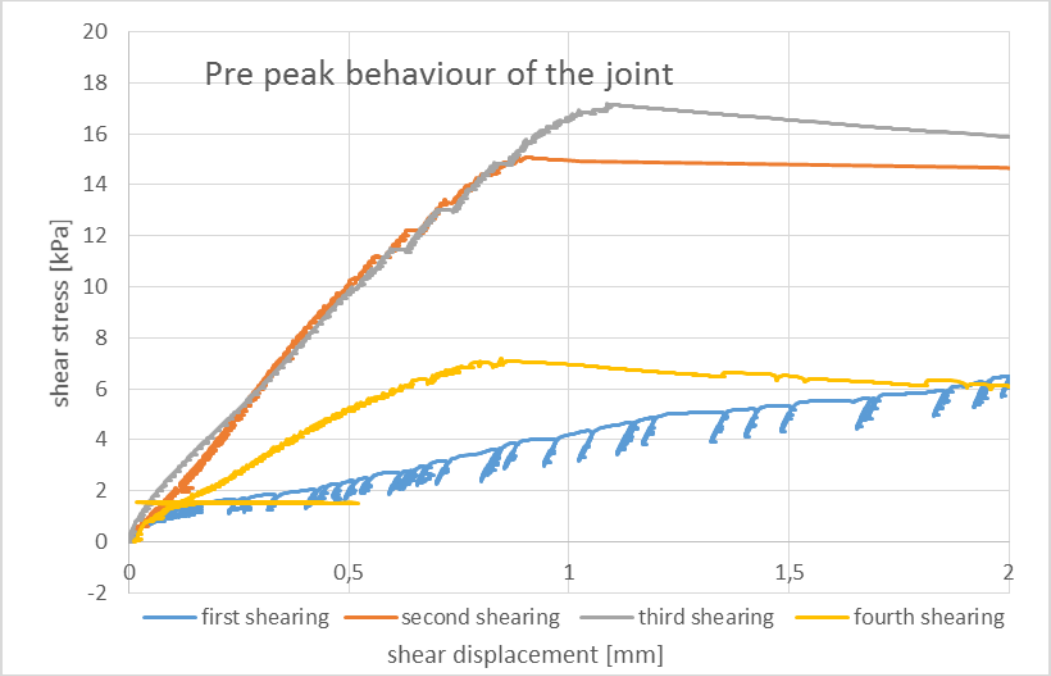

Figure 62 Stress strain curves from four stages of ASPERT during first 2 mm of shear displacement. Stick slip phenomenon can be observed during first stage shearing in pre peak behavior.

The jump in the displacement values for the first shearing, the horizontal part of the graph which shows the 0.5 mm displacement without any changes in applied shear stress is a measurement artifact and we believe it is caused by the cell phone being close to the shear displacement LVDTs.

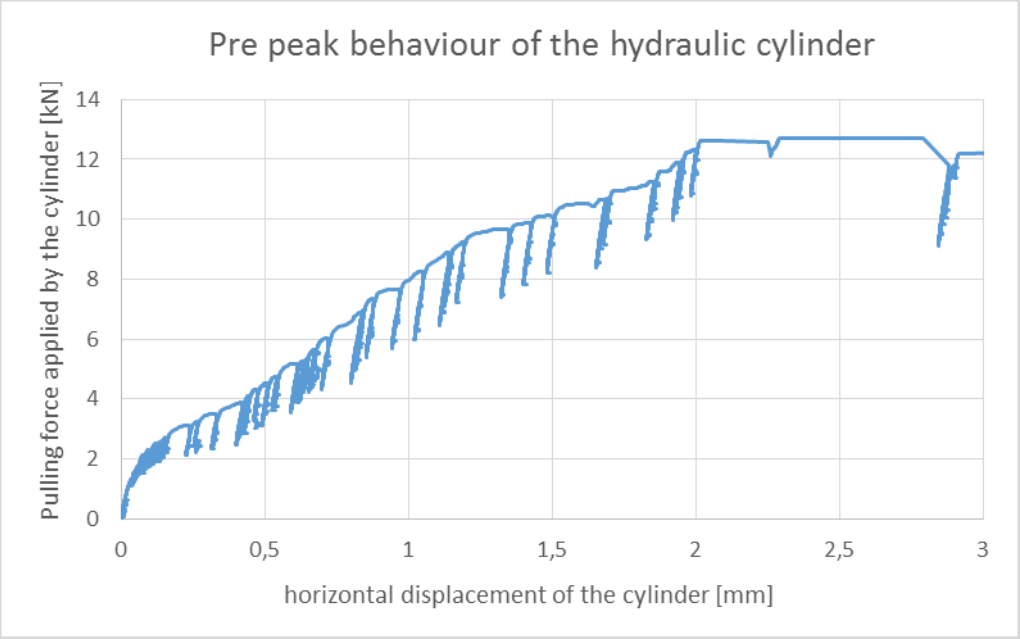

Figure 63 Pulling force applied by the hydraulic cylinder as a function of its horizontal displacement.

9 Summary and comparison of the results

In this thesis the values of peak shear strength and friction angle of analyzed sample obtained with different methods are compared. The shear strength of a joint under different levels of normal load was derived experimentally with the shear pull test (ASPERT). Results of the test were then compared with the results obtained from different methods of roughness analysis.

Roughness of the sample was analyzed with 5 different methods:

1. 3D directional roughness analysis according to Tatone and Grasselli (2009)
2. 2D joint roughness coefficient estimation with surface length method according to Maerz and coworkers (1990)
3. 2D joint roughness coefficient estimation with slope measurement method according to Tse and Cruden (1979)
4. Joint roughness coefficient estimation with hand profiling of the sample surface (Barton and Choubey, 1977)
5. Joint roughness coefficient estimation with graphical method (Barton and Choubey, 1977)

Methods 1 – 3 required the digital models of the analyzed surface. Models were created using close range photogrammetry and methodology described in chapter 5.2. In total four digital models of the sample surface were created:

1. Bottom surface before test
2. Top surface before test
3. Bottom surface after test
4. Top surface after test

The accuracy of created models was not enough according to the standard (ISRM, 2014) and the authors of directional roughness assessment method (Tatone and Grasselli, 2009) which requires the point spacing to be not more than **0.5 mm**. For that reason, values of JRC obtained with using photogrammetrically created models were overestimated. After the analysis was complete the bottom part of the sample was reshot using methodology developed in KRAMO I (Korpi, 2016) in order to verify if that methodology would give more accurate results. Point cloud created with this method was characterized with much higher point density and less point spacing of **0.3 mm**. That accuracy would most likely allow to get reliable results of JRC estimation using methods 2 and 3. Methods 4 -5 were implemented in order to obtain more reliable value of JRC. This methods did not require photogrammetrically created digital models of sample surface. The values of joint roughness coefficient were obtained using Barton´s profilometer (method 4) and the results of ASPERT (method 5). The values of JRC obtained with methods 2 – 5 are compared in table

Table 24. Comparison of JRC values obtained with different methodology.

	Surface length	Slope measurement	Estimated with figure 42	Hand measured
JRC values for bottom surface	before: 33.0 after: 31.2	before: 21.1 after: 19.9	before: 6-10 after: 8-10	6-8
JRC values for top surface	before: 41.6 after: 25,5	before: 22.6 after: 18.4		6-8

JRC values estimated with methods 2, 4 and 5 were further used to calculate the shear strength and friction angle of a joint using Barton – Bandis criterion (Baron and Choubey, 1977).

Since the values of JRC estimated with photogrammetrically created models (method 2 and 3) were overestimated, the values of friction angle calculated initially with those values were incorrect (see table 9). Yet the authors of the criterion (Barton and Choubey, 1977) point out that it loses its practical limit when the value of friction angle exceeds 70º. They advise to assume the linear relation between the shear stress and normal stress for that cases. The applicability of Barton – Bandis criterion is thus limited by the value of normal load for which friction angle exceeds 70º ($\sigma_n$limit). As it has been studied in this thesis, the value of normal load limiting applicability of Barton – Bandis criterion is proportional to the JRC value. That means, the higher JRC is, the higher limiting normal load is (see figures 50 and 51). The value of $\sigma_n$limit for ASPERT conditions was found and for JRC values as high as estimated with method 2 and 3 it was higher than the normal load used during ASPERT. Therefore, the shear strength of a joint was calculated assuming the linear relation between shear stress and normal load (see chapter 6.2.5, figures 45, and equation 22)
In case of JRC estimated with method 4 and 5 the $\sigma_n$limit was smaller than the normal load used during the all stages of ASPERT (for JRC = 6) or smaller than normal load used during the third and second stage of ASPERT (for JRC = 8). Therefore, calculation with Barton – Bandis criterion was possible using equation 18. The linear approximation was used only to predict the shear strength in first and fourth shearing stage for JRC = 8.
Results of the shear strength and friction angle calculations are compared in table 25 below.

Table 25. Comparison of shear strength and friction angle values obtained from different methods of JRC estimation and from ASPERT

ASPERT stages / Parameters	Shearing stage			
	1st	2nd	3rd	4th
Shear strength from ASPERT [kPa]	**6.7**	**15.1**	**17.2**	**7.2**
Peak friction angle from ASPERT [°]	**59**	**66**	**62**	**61**
Shear strength from photogrammetric prediction with slope measurement method (using Barton – Bandis criterion) [kPa]	10.9	18.0	25.1	10.9
Peak friction angle from photogrammetric prediction with slope measurement method (using Barton – Bandis criterion) [°]	70	70	70	70
Shear strength from hand measured JRC = 6 (using Barton – Bandi criterion [kPa]	7.3	11.5	15.5	7.3
Peak friction angle from hand measured JRC = 6 (using Barton – Bandi criterion [°]	61	60	59	61
Shear strength from hand measured JRC = 8 (using Barton – Bandi criterion [kPa]	10.9	17.3	22.8	10.9
Peak friction angle from hand measured JRC = 8 (using Barton – Bandis criterion [°]	70	69	68	70

10 Conclusion

The objectives of the thesis were mostly met. Results obtained during this research allow to answer the research questions stated at the beginning of the thesis.

Is photogrammetry a valid method to predict the friction angle of a rock joint?
In case of the sample size used in this study, the methodology of photogrammetric prediction of the surface roughness developed in KARMO II project seems to be not appropriate. That is due to the long distance between the sample and the camera during the imaging process. The determination of peak friction angle using photogrammetric interpretation did not give expected results, yet it highlighted the inapplicability of the Barton - Bandis shear strength criterion for low normal stress conditions and exposed the need for criterion which would allow the predictions even for low values of normal load. The linear approximation proposed by Barton and Choubey (1977) was used instead giving more realistic results, however still divergent from the values obtained during ASPERT.

Is the experiment methodology appropriate for determining the shear strength of rock joint, and if not why?
Methodology of shear test implemented in ASPERT is appropriate for determining the shear strength of a rock joint. Achieved results are realistic and provide not only the values of peak and residual friction angles but also the shear resistance and dilation of the sample during the test. That additional information, especially the dilation values, enabled to identify some mistakes in methodology. Those mistakes are mainly related to high elasticity of the testing machine and incorrect positioning of the sample halves on top of each other.

How the measurement procedure (both experimental and photogrammetric) can be improved to give more reliable results?
The comparison of the results revealed some discrepancies between values of shear strength and friction angle obtained with different methods. Comparing to the results of ASPERT, the results obtained with photogrammetric prediction are overestimated by 45% on average. In case of JRC estimated with hand profiling, the shear strength comparing to ASPERT was overestimated for first and fourth shearing stage by 5% on average and underestimated for the second and third shearing stage by 20% on average for JRC value equal to 6. In case of hand measured JRC = 8 all values were overestimated by 40% in relation to ASPERT results. Sources of discrepancies between the results obtained with both methods were mostly identified. In some cases additional research is needed to find out the reasons for discrepancies, however most of them were revealed in this thesis. Multiple hypotheses for discrepancies are presented and studied in this thesis. Discrepancies listed above show that there is a room for improvement in the methodology of laboratory pull test as well as of photogrammetric roughness prediction. Photogrammetric roughness estimation could be improved by applying methodology of image acquisition where the distance between camera and photographed object is minimized. Such methodology was developed in KARMO I and was testes again during this thesis. The quality digital models created with this methodology is satisfying and fulfills requirement of the standard (ISRM, 2014). Methodology of laboratory pull test could be improved by increasing the stiffness of the testing arrangement and applying a more reliable system of positioning the sample halves on top of each other.

11 Recommendations and suggested studies

The photogrammetric prediction of joint roughness and therefore its friction angle could be improved by increasing the density of produced point clouds. That should be made by using a method which allows to decrease the distance between the camera and photographed object and does not require complete overlapping of the pictures. Perhaps, a suitable method was already used in KARMO I (Uotinen et al, 2015). During this thesis, that methodology was used after the analysis was done and produced digital model was of high density (0.3 mm point spacing). Additionally, higher resolution camera should be used to improve the quality of the pictures.

The method should be established to allow estimation of the point cloud density before the acquisition of the pictures given the lighting conditions, camera settings, picture acquisition procedure details and characteristics of a surface. That would ensure consistent quality of produced point clouds and would enable comparison of the results.

A more detailed study of the photogrammetric method should be done to determine where the inaccuracies of photogrammetrically created models originate from (camera – object distance, lighting conditions, camera intersection angle, etc.)

Digital models of the surfaces could be further analyzed with methodology presented in Johansson (2014) as an alternative method prediction for friction angle prediction.

The methodology of the pull test could be improve by implementing a more reliable system of orientation of the sample halves. Some discrepancies probably originated from the sample parts not being placed on top of each other properly. Moreover, sorter chains could be used in the test arrangement in order to reduce elasticity of the system and therefore minimize the influence of stick slip phenomenon.

Numerical modelling studies could be conducted using the digital models of the surface to test the behavior of a joint when submitted to higher normal load. That would allow the prediction of friction angle with Barton – Bandis criterion without the need to apply big normal load on the sample.

There is a need for shear strength criterion which would be applicable in low normal stresses.

12 References

Bandis, S. 1980, Experimental studies of scale effect on shear strength, and deformation of rock joints [PhD thesis], *The university of Leeds*

Bandis, S., Lumsden, A., Barton, N.R. 1981, Experimental studies of scale effect on the shear behaviour of rock joints, *Int. J. Rock Mech. Min. Sci. & Geomech. Abstr.*

Bandis, S., Lumsden, A.C., Barton, N.R. 1981, Experimental studies on scale effects on the shear behaviour of rock joints, *Int. J. Rock Mech. Min. Sci. & Geomech. Abstr. Vol. 18, No. 1, pp. 1-21*

Barton, N. R. 1971, A relationship between joint roughness and joint shear strength, *Norges Geotekniske Institutt*, Oslo, Norway

Barton, N.R, Choubey, V. 1977, The shear strength of rock joints in theory and practice, *Rock Mechanics, Vol. 10/1-2*

Barton, N.R. 1973, Review of a new shear strength criterion for rock joints, *Engineering Geology, Vol. 7, pp. 287-332*

Barton, N.R. 1976, The Shear Strength of Rock and Rock Joints, , *Int. J. Rock Mech. Min. Sci. & Geomech. Abstr.Vol. 13, pp. 255-279*

Barton, N.R. 2013, Shear strength criteria for rock, rock joints, rockfill and rock masses: Problems and some solutions, *Journal of Rock Mechanics and Geotechnical Engineering, Vol. 5/249-261*, Oslo, Norway

Brown, E.T. 1971, Strength – size effects in rock material, *Proc. Int. Symp. on Rock Mech., Nancy, Paper II – 11*

Brown, S.R. 1987, A note on the description of surface roughness using fractal dimension, *Goephysical Research Let. Vol. 14, pp. 1095-1098*

Castelli, M., Re, F., Scavia, C., Zaninetti, A. 2001, Experimental evaluation of scale effects on the mechanical behaviour of rock joints, *In: Sarkka, P., Eloranta, P. editors, Proceedings of Eurock 2001 Rock Mechanics – A Challenge for Society, Espoo, Finland*, Rotterdam, Netherlands

Giani, G.P. 1992, Rock slope stability analysis, *Technical University of Turin*, Rotterdam, Netherlands

Godman, R.E., Taylor, R.L., Brekke, T. 1968, A model for the mechanics of jointed rock, *J. Soil Mech. Div., Proc. ASCE, Vol. 94, pp. 637-659*

Grasselli, G. 2001, Shear strength of rock joints based on quantified surface description [PhD thesis], *University of Parma*, Parma, Italy

Hencher, S.R., Toy, J.P., Lumsden, A.C. 1993, Scale – dependent shear strength of rock joints, *In: Pinto Da Cunha A, editor. Proceedings of the 2nd International Workshop on Scale Effects in Rock Masses, pp. 233 – 240, Lisbon, Portugal*, Rotterdam, Netherlands

Hoek, E. 2007(ed.), Practical Rock Engineering, available online: https://www.rocscience.com/learning/hoek-s-corner/books

Hoek, E., Londe, P. 1974, Surface Workings in Rock, *Proc. 3rd Cong. Int. Soc. for Rock Mech., Vol. 1, pp. 613 – 654*, Denver, Colorado

Hsiung, S.M., Ghosh, A., Ahola, M.P., Chowdhury, A.H. 1993, Assesment of conventional methodologies for joint roughness coefficient determination, *Int. J. Rock Mech. Min. Sci. & Geomech. Abstr.Vol. 30, No.7, pp. 825-829*

Iakolev, D., Sirkiä, J., Kallio, P., Uotinen, L. 2015, Determination of joint mechanical parameters for stability analysis in low stress open pit mines, *Rock stress 2016 Symposium, Tampere, Finland*

Il´Nitskaya, E.I. 1969, Effect of Rock – Specimen Size on Mechanical Properties in Shear Test, *Mechanical Proprrties of Rocks, pp. 56-63*

ISRM 2007, The Complete ISRM suggested methods for rock characterization, testing and monitoring: 1974 – 2006, *Compilation arranged by the ISRM Turkish National Group, Editors: Ulusay, R., Hudson, J.A.* Ankara, Turkey

Johansson, F. 2009, Shear Strength of Unfilled and Rough Rock Joints in Sliding Stability Analyses of Concrete Dams [PhD], *KTH Architecture and the Built Environment, Divison of Soil and Rock Mechanics, Royal Institute of Technology*, Stockholm, Sweden

Johansson, F. 2015, Influence of scale and matedness on the peak shear strength of fresh, unweathered rock joints, , *Int. J. Rock Mech. Min. Sci. & Geomech. Abstr. Vol. 82, pp. 36-47*

Johansson, F., Stille, H. 2014, A conceptual model for the peak shear strength of fresh and unweathered rock joints, *Int. J. Rock Mech. Min. Sci. Vol. 69, pp. 31 - 38*

Kim, D.H., Gratchev, I., Poropat, G.V. 2013, Theb determination of joint roughness coefficient using three – dimensional models for slope stability analysis, *Australian Centre for Geomechanics*

Kolecka, N. 2011, Photo – based 3D Scanning – Competitive Data Aquisition Methods for Digital Terrain Modelling of Steep Mountain Slopes, *Jagiellonian University, Department of GIS, Cartography and Remote Sensing,* Krakow, Poland

Kulatilake, P.H.S.W., Shou, G., Huang, T.H., Morgan, R.M. 1995, New peak shear strength criteria for anisotropic rock joints, *Int. J. Rock Mech. Min. Sci. & Geomech. Abstr. Vol. 32, No. 7, pp. 673-697*, Great Britain

Kutter, H.K., Otto, F. 1990, Influence of parallel and cross-joints on shear behaviour of rock discontinuities, *Rock joints, Loen, Norway. pp. 243-250*

Lee, Y.H., Carr, J.R., Barr, D.J., Haas, C.J. 1990, The fractal dimension as a measure of the ropughness of rock discontinuity profiles, *Int. J. Rock Mech. Min. Sci. & Geomech. Abstr. Vol. 27, pp. 435-464*

Londe, P. 1973, The role of rock mechanics in the reconnaissance of rock foundations, *Q. Journal of Engng. Geology, Vol. 6*

Malinverno, A. 1990, A simple method to estimate the fractal dimension of a self – affine series, *Goephysical Research Let. Vol. 17, pp. 1953-1956*

McWilliams, P.C., Kerkering, J.C., Miller, S.M. 1993, Estimation of Shear Strength Using Fractals as a Measure of Rock Fracture Roughness, *United States Department of the Interior, Report of Investigations/1993*

Meemun, P., Fuenkajorn, K. 2015, Shear strength testing under constant normal load and contstant normal stiffness as affected by displacement rates, *Geomechanics Research Unit, Suranaree University of Technology, Vietrock2015 an ISRM specialized conference*

Melin, H. 2012, Controlling parameters for normal and shear behaviour of rock fractures – a study of direct shear test data from SKB [M.Sc. thesis], *KTH Architecture and the Built Environment, Division of Soil and Rock Mechanics*, Stockholm, Sweden

Muralha, J., Grasselli, G., Tatone, B., Blumel, M., Chryssanthakis, P., Yujing, J. 2014, ISRM Suggested Methods for Laboratory Determination of the Shear Strength of Rock Joints: Revised Version, In: The ISRM Suggested Methods for Rock Characterization, Testing and Monitoring: 2007 – 2014, *Springer, editor. Ulusay, R.*

Muralha, J., Pinto Da Cunha, A. 1990, About LNEC experience on scale effects in the mechanical behaviour of rocks, *In: Pinto Da Cunha A, editor. Scale Effects in Rock Masses – Proceedings of the First International Workshop on Scale Effects in Rock Masses, pp. 131 – 148*, *Loen, Norway*

Nilsson, M., Edelbro, C., Sharrock, G. 2012, Small scale joint surface roughness evaluation using digital photogrammetry, *Eurock*

Patton, F.D. 1966, Multiple modes of shear failure in rock and related materials [PhD thesis], *University of Illinois*

Poturovic, S., Schubert, W., Blumel, M. 2015, Comparsion of constant normal load (CNL) and constant normal stiffnes (CNS) direct shear test, *Eurock 2015 Future Development of Rock Mechanics, pp. 445-450*, Salzburg, Austria

Power, W.L., Tullis, T.E. 1991, Euclidean and fractal models for the description of rock surface roughness, *J. Geophys. Res. Vol. 96(B1), pp. 415-424*

Pratt, H.R., Black, A.D., Brown, W.S., Brace, W.F. 1972, The effect of specimen size on the mechanical properties of unjointed diorite, *Int. J. Rock Mech. Min. Sci. & Geomech. Abstr.Vol. 9, pp. 513-529*

Pratt, H.R., Black, W.S., Brace, 1974, Friction and deformation of jointed quartz diorite, *Int. Soc. Rock Mech. Vol. II, pp. 306-310*, Denver

Rengers, N. 1971, Unebenheit und der Reibungswiderstand von Gesteinstrennflächen, *Diss. Tech. Hochschule Fridericana, Karlsruhe, Ins. Bodenmech. Felsmech. Veröff. 47, pp 1 – 129*

Schenk, T. 2005, Introduction to photogrammetry, *The Ohio State University, Department of Civil and Environmental Engineering and Geodetic Science*

Sirkiä, J. 2015, Requirements for initial data in photogrammetric recording of rock joint surfaces [M.Sc. thesis], *Aalto University, School of Engineering*, Espoo, Finland

Sirkiä, J., Kallio, P., Iakovlev, D., Uotinen, L. K. T. 2016, Photogrammetric calculation of JRC for rock slope support design, *Ground Support 2016*

Tatone, B.S., Grasselli, G. 2009, Amethod to evaluate the three - dimensional roughness of fracture surfaces in brittle geomaterials, *Review of scientific instruments, Vol. 80*

Terzaghi, K. 1925, *Erdbaumechanik auf Bodenphysikalischer Grundlage, Vienna: Franz Deuticke*

Unal, M., Yakar, M., Yildiz F. 2004, Discontinuity surface roughness measurement techniques and the evaluation of digital photogrammetric method, *Selcuk University*

Unala, M., Yakarb, M., Yildizb, F. 2004, Discontinouity surface roughness measurement techniques and the evaluation of digital photogrammetric method, *XXth ISPRS Congress*, Istanbul, Turkey

Wakabayashi, N., Fukushige, I., 1992, Experimental study on the relation between fractal dimension and shear strength, *Conference of Fractured and Jointed Rock Masses*

Wickens, E.H., Barton, N. R. 1971, The application of photogrammetry to the stability of excavater rock slopes, *Photogrammetric record, Vol 7(37), pp. 46-54*

Yoshinaka, R., Yoshida, J., Arai, H., Arisaka, S. 1991, Scale effects on shear strength and deformability of rock joints, *In: Proceedings of the 2nd international work-shop on scale effects in rock masses. Ed. Pinto de Cunha, pp. 143-149*, Rotterdam, Netherlands

Zhao, J. 1997a, Joint Surface Matching and Shear Strength Part A: Joint Matching Coefficient (JMC), *Int. J. Rock Mech. Min. Sci. & Geomech. Abstr. Vol. 34, pp. 1997*

Zhao, J. 1997b, Joint Surface Matching and Shear Strength Part B: JRC-JMC Shear Strength Criterion

13 Appendix

Appendix 1 Colormap of created surfaces

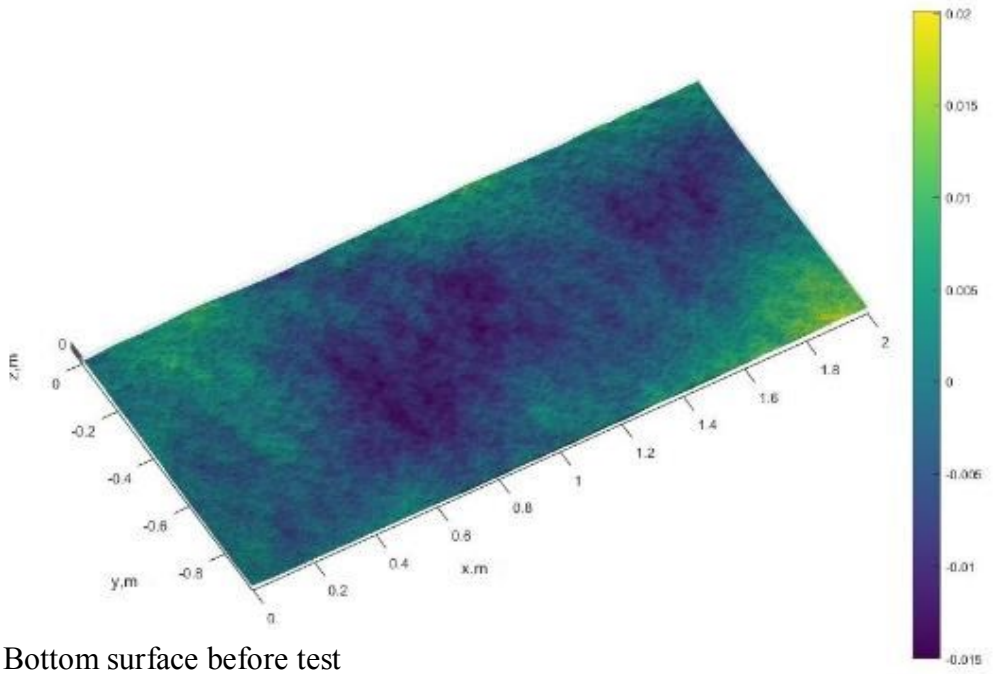

a) Bottom surface before test

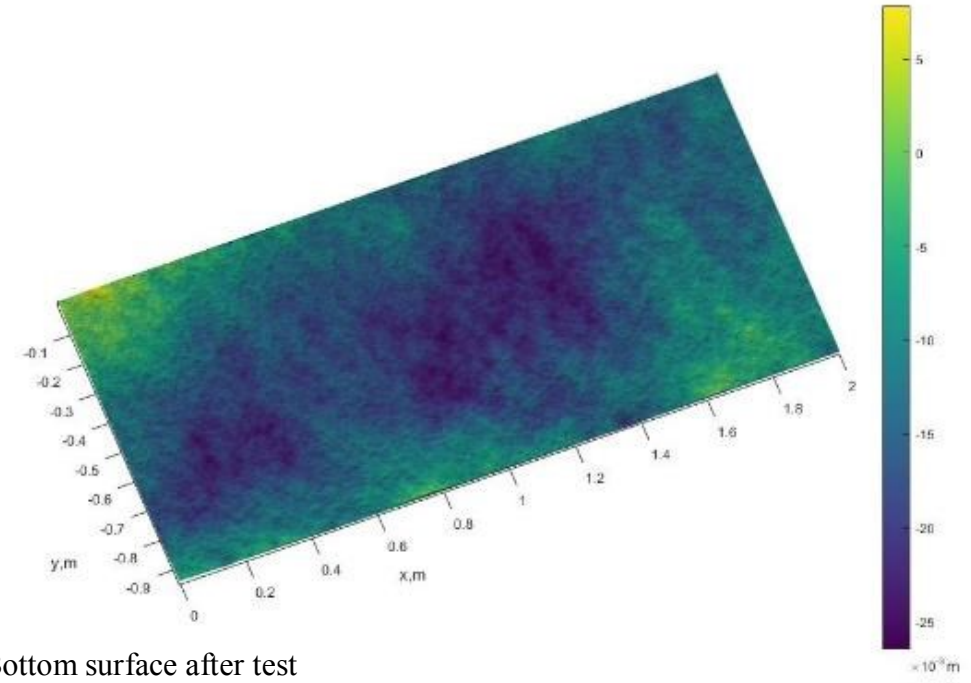

b) Bottom surface after test

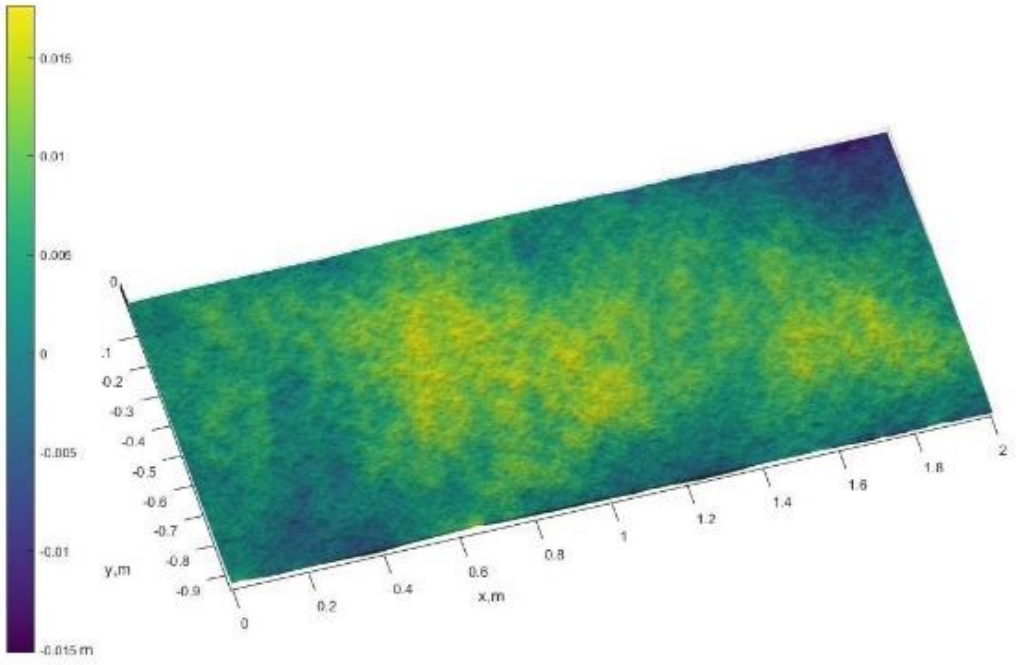

c) Top surface before test

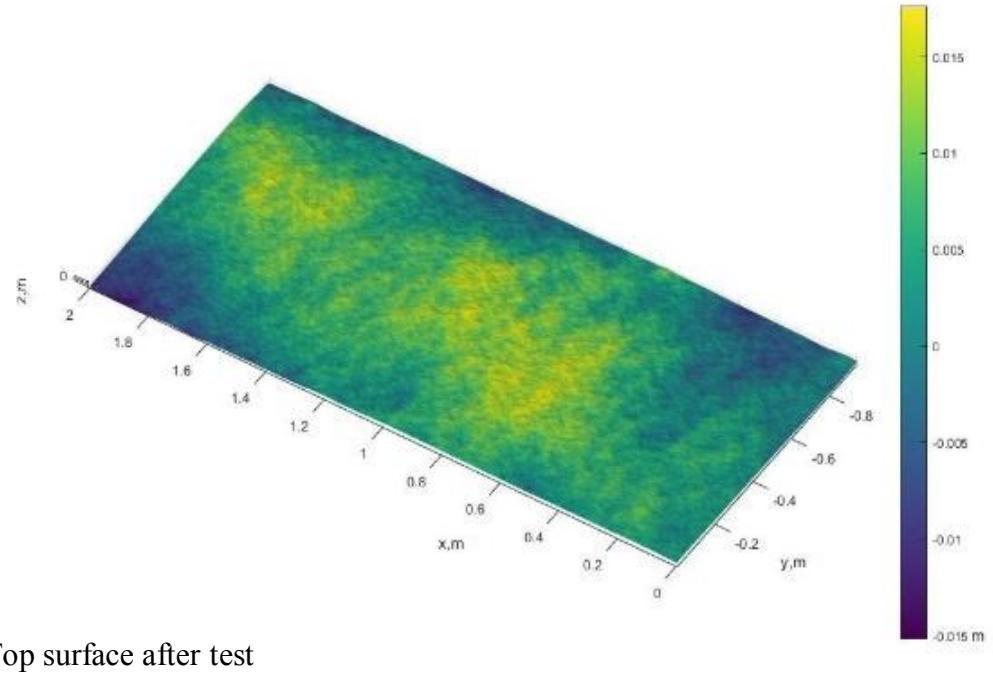

d) Top surface after test

Figure 64 Appendix 1. Colormaps of photogrammetrically created models of the joint surface

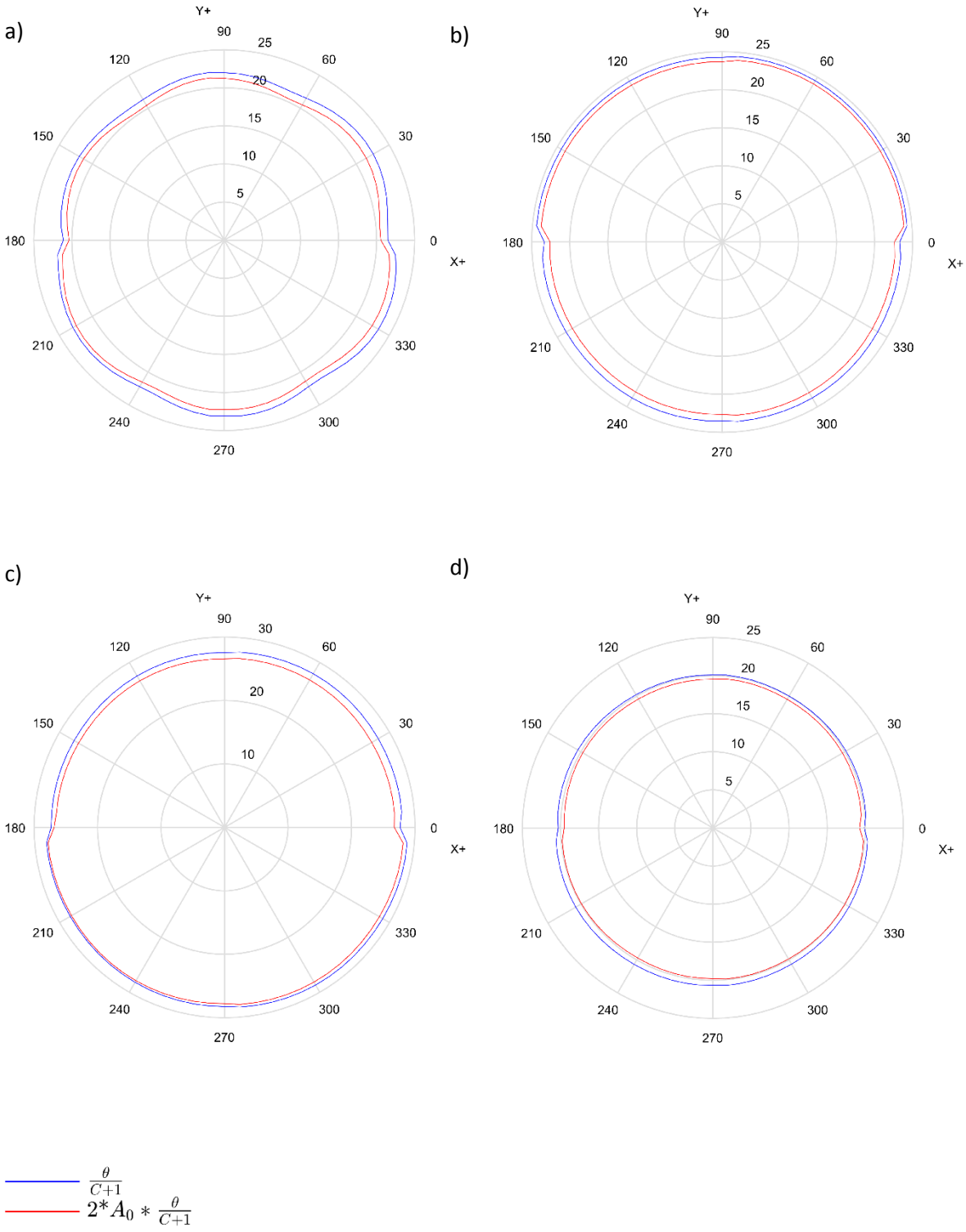

Figure 65 Appendix 2. Results of 3D directional roughness analysis as a form of polar plots. a – bottom surface before test, b – bottom surface after test, c – top surface before test, d – top surface after test

Appendix 3 Assembly pictures of the ASPERT

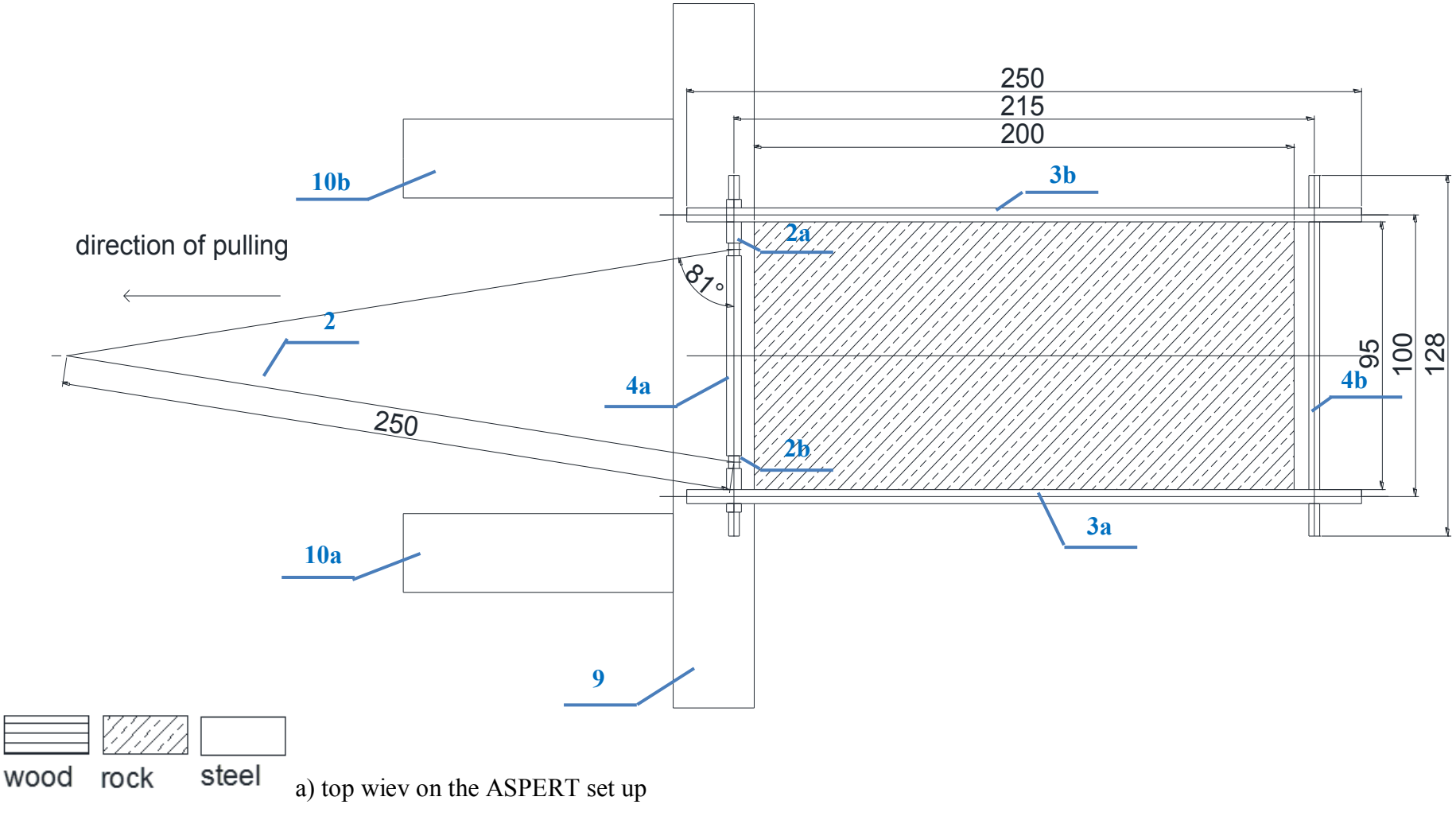

a) top wiev on the ASPERT set up

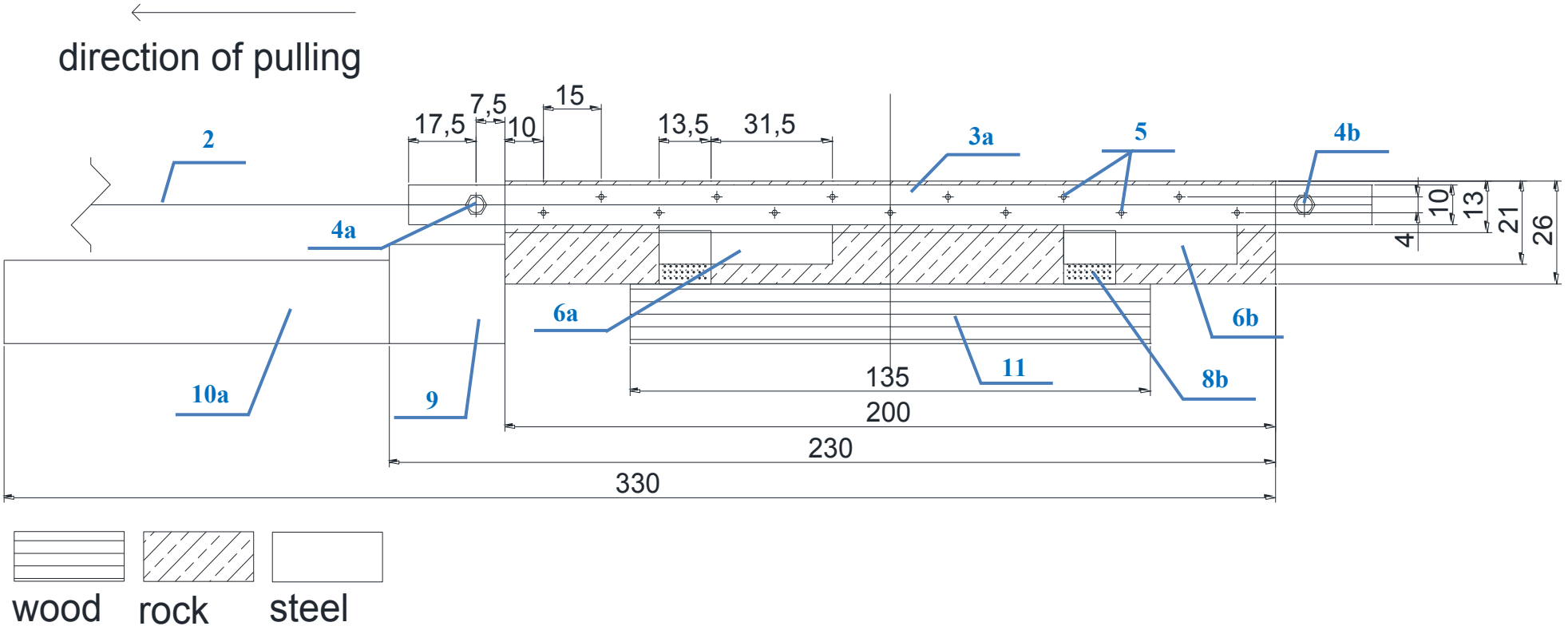

b). Side view of the ASPERT set-up

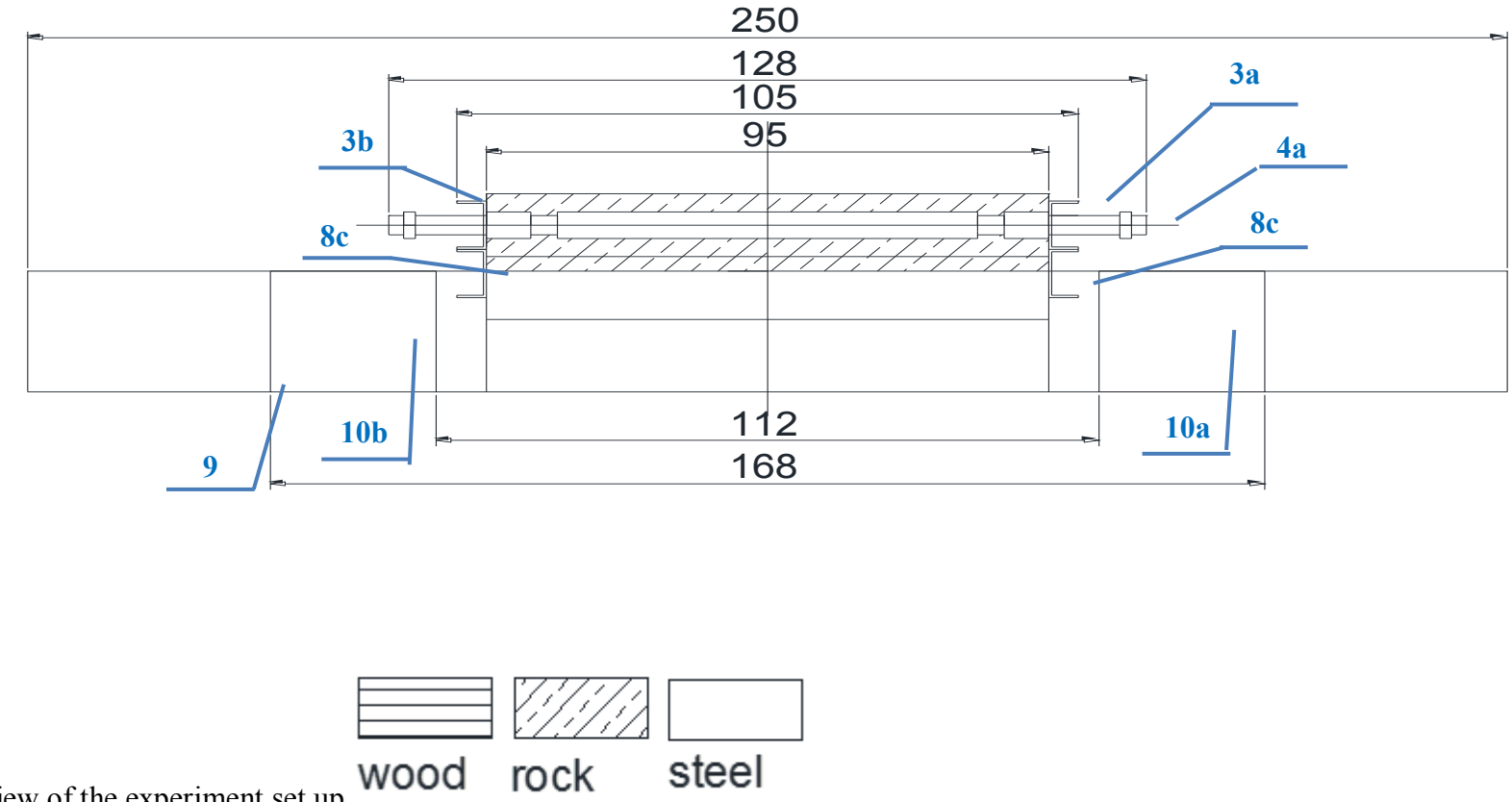

c). Front view of the experiment set up

Figure 66 Appendix 3. Assembly pictures of ASPERT set up